Computational and Experimental Study of Nasal cavity Airflow Dynamics

A thesis submitted for the degree of

Doctor of philosophy

of the University of London

by

Shahrzad Nayebossadri

School of Engineering and Materials Sciences

Queen Mary University of London

May 2012

I declare that this thesis and the research to which it refers, are the product of my own work, and that any ideas or quotations from the work of other people, published or otherwise, are fully acknowledged in accordance with the standard referencing practices of the discipline. I acknowledge the helpful guidance and support of my supervisor, Dr. Eldad Avital.

Signed:

(Shahrzad Nayebossadri)

ABSTRACT

This work aims to assess human nasal blockage by investigating its influence on nasal airflow dynamics, both computationally and experimentally. An in-house CFD code (Lithium) computes the steady (mean) nasal airflow for a cavity constructed from CT images of a healthy adult, for the internal cavity and for the first time for the external flow. To account for turbulence occurrence, the low Reynolds number k-ω Reynolds-Averaged-Navier-Stokes (RANS) model is used. The flow field is calculated at different breathing rates by varying the influx rate. Blockages are introduced at various locations inside the cavity to investigate common nasal blockages. The computational results are assessed against published literature and the Particle Image Velocimetry experimental (PIV) results, carried out on a 2.54:1 scale model of the computational nasal cavity. Schlieren optical technique is also used for external nasal airflow visualizations of a human subject, to comment on using an optical system for clinical application.

These computations reveal a significant dependency of both, the internal and external nasal airflow fields on the nasal cavity's geometry. Although for this model, the flow is found to be turbulent in the inspiratory phase of 200 *ml/s* and higher, it is suggested that the nature of flow can vary depending on the nasal cavity's structure which is influenced by genetics. Nevertheless, some common flow features were revealed such as higher flow rate in the olfactory region and main flow passage through lower airways during inspiration. More uniform flow passage was found in expiration. The results also suggest a possible correlation between the internal geometry of the cavity and the external nasal airflow angle and thickness. This

correlation can allow an application of optical systems such as Schlieren which is shown to give accurate qualitative images of the external nasal airflow for assessment of the nasal blockage.

ACKNOWLEDGEMENTS

Table of Contents

1. Chapter 1

Introduction

2. Chapter 2

Literature Review

3. Chapter 3

Computational Procedure

4.   Chapter 4

Experimental Procedure

5.   Chapter 5

Computational Flow Field for the Normal Nasal Cavity

6.   Chapter 6

Influence of Nasal Blockage on Flow Dynamics and Physiology

7.   Chapter 7

Experimental Results & Comparison with Computational Data

8.   Chapter 8

Discussion

9.   Chapter 9

Conclusion & Future Work

List of Figures

14

List of Tables

LIST OF SYMBOLS

Notation

a – Un-obstructed height of the light source image

A – Inflow cross section

c_p – Specific heat capacity at a constant pressure process

e – Specific internal energy

f – Breathing frequency

F – Force

K – Gladstone coefficient

k – Turbulent kinetic energy

L – Axial characteristics

M – Mach number of flow

n – Refractive Index

$(n-1)$ – Refractivity

NR – Nasal resistance

P – Pressure

q – Volume flow rate

Re – Reynolds number

s – Sensitivity of Schlieren system

St – Strouhal number

t – Time

T – Temperature

(U, V, W) – Instantaneous velocity components in x, y and z directions

$(\bar{u}, \bar{v}, \bar{w})$ – Mean velocity components in x, y and z directions

(u', v', w') – Fluctuation velocity components in x, y and z directions

Greek Symbols

δ_{ij} – Kronecker delta

ε – Dissipation per unit mass

λ – Wave length

μ – Molecular viscosity

μ_t – Eddy viscosity

ν – Kinematic molecular viscosity

ν_t – Kinematic eddy viscosity

ρ – Density

τ – Shear stress

τ_{ij} – Specific Reynolds stress tensor

ω – Specific dissipation rate

Subscripts

LES – Large Eddy Simulation

NSE – Navier Stokes Equations

$RANS$ – Reynolds Average Navier Stokes Equations

Pd – Pressure difference

SF − Safety factor

TVD − Total variation diminishing

URANS − Unsteady Reynolds Average Navier Stokes Equations

1. Chapter 1

Introduction

The nasal cavity performs a variety of physiological functions which are crucial to the respiratory system. These functions may be impaired due to disorders associated with the nasal cavity. One of the most common diseases encountered in Rhinology is the nasal blockage which can be quite problematic for a healthy functioning of the human nose, and therefore it is desirable to be assessed and diagnosed accurately. Unfortunately the assessment of the nasal blockage has proven to be quite limited based on the available clinical tools, due to their low clinical significance. This has created a demand to search for new tools. One promising field is based on dynamics assessment, using the nasal airflow. This has been brought to attention since the nasal physiological function is strongly dependant on the nasal airflow dynamics. It is believed that a comprehensive understanding of the nasal airflow may alternatively lead into a computer assisted tool which can assess the nasal obstructive disorders and help towards drug delivery via the nasal cavity.

1.1 Nasal Anatomy & Physiology

The nose is the entrance to the respiratory system and is the passageway for the airflow. It functions as an odour detector an air conditioner [1] and can be divided into external and internal parts. The external nose is formed and supported by the nasal and maxilla bones on the upper half and cartilage on the lower half. This

supporting framework of bones and cartilage are covered with muscles and skin. The internal nose also known as the nasal cavity, is the large passageway which is enclosed by the nasal bones from above, maxilla laterally and the bones of hard plate on its floor. The nasal cavity communicates with the external nose via the nostrils and is connected to the pharynx from the other end. The cavity is divided medially by a thin vertical plate called the nasal septum into two distinct passageways, each with its own separate blood supply and nerve pathway. Each of these passageways which on occasion may operate quite independently can be further partitioned into different sections of nasal vestibule, nasal valve, turbinated nasal airway (respiratory region) and the nasopharynx.
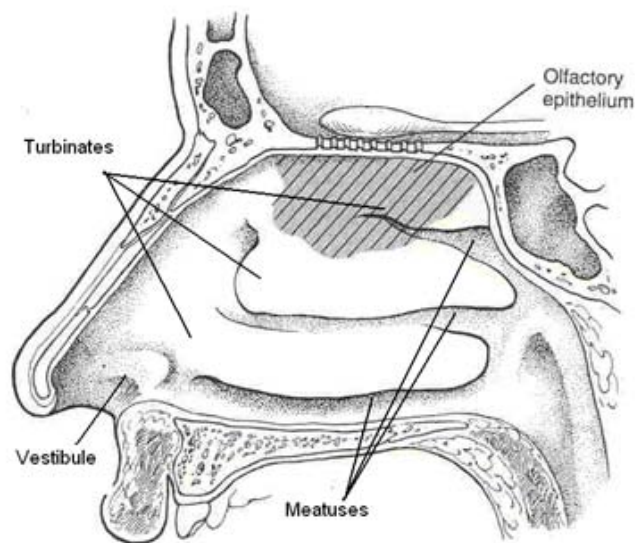
Figure 1: Schematic description of the human nasal cavity [2].

The nasal vestibule lies immediately posterior to the external nares and is stiffened by cartilage to which the facial muscles such as the alae nasi, are attached. During

inspiration these muscles contract and splint the vestibule to prevent collapse [1].
The tube shape of the vestibule redirects the flow entering the nares from the front,
below and sides towards the internal cavity [3]. This section is lined by stratified
squamous epithelium and sweat and sebaceous glands. The vibrissae in this region
trap large particles which have entered the nasal cavity with the inspired air [4] .

The nasal valve is the cartilage and the erectile tissue located at the anterior tip of
the inferior turbinate and the nasal septum which acts as a valve, regulating the
airflow [3] . This section has the narrowest cross sectional area within the nasal
cavity and contributes the most to the nasal resistance. At the posterior end of the
nasal valve, there is an abrupt increase in the cross sectional area marking the
beginning of a section referred as the respiratory region where the lining of the cavity
becomes pseudostratified ciliated columnar epithelium (respiratory epithelium)
containing goblet cells. The respiratory epithelium rests on a basement membrane
which is connected to a thick layer of lamina propria, rich in blood vessels and
seromucosal glands [2].

The surface of the lateral wall holds three bony projections called the upper, middle
and lower turbinates (choncae). These outgrowths form three airways and meatuses
named after their neighbouring turbinate, providing air passageways and drainage for
the sinuses and the naso-acrimal duct. The presence of the turbinates in this region
adds to the surface area to facilitate the conditioning. Temperature of the air
reaching the main nasal airway is adjusted near the body temperature by the blood
vessels. Also the mucus secreted from the goblet cells supplemented by the secretion
of the seromucosal glands humidify the air and trap other particles which can be a

thread to the lower respiratory system. The movement of the cilia of the epithelial cell in this region moves the mucus towards the throat where it can be discharged [5]. The blood vessels in the lamina propria in the middle and lower turbinates also control the airflow by changing the nasal patency in this region in response to the changes in environmental condition such and temperature and humidity as well as posture. This is done by engorgement of the blood vessels in a cyclic manner under the control of the sympathetic nerve system. This physiological congestion and decongestion of the mucous membrane is known as the nasal cycle [2]. These periodic changes of the nasal cavities volume may control the balance between the fluxes of heat and water vapour required to condition the inspired air and the ability of the nasal blood flow and mucus secretion to supply sufficient heat and water to the surface area [6].

Tissue on the upper part of the nasal septum and the lateral wall forms the olfactory epithelium which contains olfactory receptors (nerve cells) detecting the odorants dissolved in the serous covering the epithelium. The last section located within the cavity is the nasopharynx which joins the cavity to the pharynx.
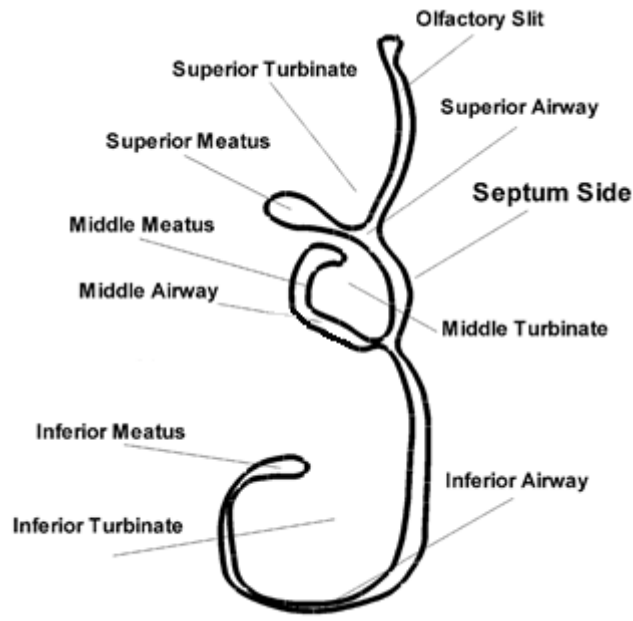
Figure 2: Anatomy of coronal planes of the nasal cavity [7].

1.2 Nasal Obstruction and Assessments

The nasal cavity is the first line of defence, protecting the delicate lower respiratory tract. It also provides ample time for the heat and water exchange to enable equilibrium to near intra-alveolar conditions [8]. Any disorder in physiological function of the nasal cavity can be a potential risk to lower respiratory disease and infection. One of the most common symptoms encountered in multiple sinonasal disease is the nasal blockage. Many factors such as anatomical abnormalities and allergies can lead to a constant sensation of blockage and deterioration of the nasal functioning. Nasal obstruction may also interfere with mucous flow and sinus drainage and cause sinus infection and severe headaches.

The treatment for nasal obstruction should be rationally based on the assessment of type and degree of blockage. Various methods and instruments have been introduced

ranging from the subjective one to more subtle objective criteria. Although the symptoms of the nasal blockage are relatively subjective, they do not always coincide with the nasal cavities findings. Some early works have shown that there is no correlation between the subjective sensation and the actual condition of the nasal cavity [9-11]. Jones et al. [12] has carried out several studies involving local anaesthesia of the vestibule and the mucous membrane in the main airway one at the time and in tandem. The local anaesthesia of the vestibule region was followed by a sensation of blockage despite any change in the nasal cavity's geometry. This suggested that the receptors in this region are responsible for signalling a sensation of patency. Topical anaesthesia of the main airway however was followed by an enhanced sensation of patency, suggesting that the receptors in this region are responsible for sensation of blockage [13]. When both regions were anaesthetized the overall sensation was the nasal obstruction without any changes to the actual condition of the nasal cavity [14]. This suggested that any judgement on the internal condition of the nasal cavity based on the subjective sensation must be avoided or only be used complementary to the objective assessments. [15]

Nasal obstruction can be assessed objectively using structural or dynamic tests. Structural assessment of the nasal patency gives information about the condition of the cavity's geometry such as cross sectional area, and the volume. Some of the traditional techniques include rhinoscopy, rhinostereoscopy or radiologic studies such as CT and MRI. Acoustic rhinometry is one the most recent techniques which uses an audible reflected sound wave that is converted to produce an area-distance graph [16]. Cory et al. [17] showed the acoustic rhinometry is sensitive enough to

indicate the difference between a normal and an allergic respond of the nasal cavity to a decongestion and therefore is a valuable technique. However this technique is limited to give measurements of the posterior part of the nasal cavity since the results might vary as a result of alternation in size of the nasopharynx caused by movement of the soft plate. There might also be an overestimation due to influencing of the nasal cavity' branching at the end of the septum. Other variation in measurements might occur due to modification or loss of sound waves along the opposite nasal passageway and alternating nasal cycle that influences individual measurements. These findings were also confirmed when the validity of acoustic rhinometry was assessed by comparing the results to those obtained by high resolution computer tomography. The result shows that acoustic rhinometry is capable to give accurate objective information about the cross sectional area and volume of the anterior and middle parts of the cavity, and its accuracy decreases towards the posterior part [18].

Structural information is critical for understanding the nature of the blockage but in many cases it is difficult to translate these objective findings into an assessment as to whether the narrowing of the nasal passages actually impairs the physiological function of the nose. Therefore in recent years considerable attention has been paid to quantify the degree of the nasal patency by measuring some of the aspect of the nasal airflow. Initially cold mirrors were used to enable observation of condensed vapour water patterns [19]. Mirrors were replaced in 1950s when Rhinomanometry was developed allowing numerical measurement of the patency. Since then new techniques have been introduced and old ones have been refined and improved. Clark et al. [20] described a method to assess the patency by measuring the nasal peak

flow at inspiration and in 1980s Youlten made a modification to the write peak flow meter which currently is in use for nasal peak flow aspiratory measurements. The most common techniques currently used in clinics are rhinomanometry and the nasal peak flow.

Rhinomanometry is a well established method, assessing the nasal patency by measuring the nasal airway resistance which is the ratio between the transnasal pressure and the volumetric flow rate. Mean total resistance has been reported to be around 0.23 $pa.cm^{-3}.s$ ranging from 0.15 to 0.39 where 0.30 is considered as an upper limit of the normal range [21]. Rhinomanometry can be divided into active and passive and further into posterior and anterior [22]. Yaniv et al. [23] measured the subjective sensation of sixteen patients with recurrent maxillary sinusitis due to an enlarged uncinate process using a visual scale before and after uncinectomy during functional endoscopic sinus surgery. These measurements were compared to the nasal resistance values calculated using the anterior rhinomanometry. No correlation was found between the two measurements, since the subjective measurements of all patients showed a sense of increase in the nasal airflow after the uncinectomy whereas the nasal resistance values were the same. Lund et al. [24] in 1991 also took the subjective and objective measurements of the nasal patency before and after functional endoscopic sinus surgery using rhinomanometry and confirmed the results reported by Yaniv [23]. Other studies [25, 26] have also shown a significant difference between the nasal resistance values, measured using rhinomanometry and the minimal cross sectional areas using an acoustic rhinometry, suggesting the low diagnostic value of rhinomanometry for evaluating the obstructive disorders.

Nasal peak flow measures the peak flow during inspiration or expiration. This is a cheap, simple and non invasive technique, which can provide information about the condition of the cavity. For nasal peak expiratory flow (NPEF), a mini Wright peak flow meter is used along with an airtight face mask. Patients are required to inspire to the total lung capacity and expire with maximum effort through the nose while keeping the lips tightly closed [21]. A potential drawback of this technique is the blowing of mucus into peak flow meter. Alternatively nasal peak inspiratory flow (NPIF) is measured using a Youlten Peak flow meter which is an inverted mini-Wright flow meter. In this procedure an anaesthesia mask is placed over the nose and mouth which acts as an airtight seal around these areas. Patients are then asked to inspire air forcefully through the nose, again with lips tightly closed. NPIF is associated with a small risk of nasal vestibular collapse. Many works have confirmed the suitability of nasal peak inspiratory flow by showing positive correlation to the nasal resistance and subjective measurements [27, 28] . However there are other studies which have shown that the nasal peak flow measurements are not as sensitive as other objective techniques, and not reproducible [20, 21].

Despite many years of establishments and modifications on all current clinical techniques there are still discrepancies on their actual relevance to assess nasal patency. Also the information given by these methods is very limited to specific measurements such as the cross sectional area and the volume flow rate. In order to fully understand the physiology of the nasal cavity, more enhanced dynamic information is required. This has drawn the attention of experts into investigate the nasal cavity's airflow characteristics.

1.3   Aims and Objectives

The primary aim of this study is to assess the nasal blockage based on nasal airflow dynamics. However the dynamics of the nasal airflow is still considered a new topic in the scale of scientific research even though it has been studied since the early nineteenth century. There are still many uncertainties even in some of the most basic flow principles, such as the nature and the main path of the nasal airflow. Some of the discrepancies in the nasal airflow fields when investigated by CFD methods arise due to different numerical methods and flow assumptions. The accuracy of the experimental data on the other hand is always limited due to the small size and the complex geometry of the nasal cavity. It is therefore essential to continue the investigation of the nasal airflow dynamics until the flow field is fully understood and a similar thought is observed in recent publications. In this study the internal nasal airflow is investigated computationally using an accurate cavity model constructed from the CT images of a healthy adult. The results are validated against the available computational and experimental literature. Furthermore there are only limited studies which have investigated the influence of various nasal obstructive disorders on the nasal airflow. More research is required in this area to allow assessing the possibility of using the airflow dynamics as a diagnostic tool. For this the nasal airflow has been also investigated for various obstructed cavities. This has been done by varying the nasal cavity's internal geometry to represent some of the most common conditions of nasal blockages. Moreover since, flow visualisations and measurements of the internal nasal airflow can be quite challenging due to the small size and the complex geometry of the nasal cavity, the possibility of using the

external nasal airflow to assess the obstructive disorders, is investigated by extending the computational grid to a region outside the nostril. The external flow pattern is studied for the normal and obstructed cavities. This is the first attempt to the knowledge of the author. Finally the external nasal airflow has also been investigated experimentally using Particle Image Velocimetry and Schlieren optical technique to allow commenting on the external computational results and to assess the possibility of using simple flow visualisation techniques for clinical use respectively.

1.4 Research Design and Methodology

In this work the internal respiratory nasal airflow is investigated computationally using a cavity model constructed from the CT scans of a healthy human subject [29]. An in-house CFD code (*Lithium*) is used to calculate the steady (in the mean) and incompressible airflow field at normal breathing rates of 50 up to 300 *ml/s*. To account for the possibility of turbulence the low Reynolds number k-ω Reynolds-Averaged-Navier-Stokes (RANS) model is applied [30]. In addition to the internal nasal airflow field, the computational grids are extended so that the expiratory flow outside the nostril can also be investigated.

Since the ultimate aim is to assess the nasal blockage, based on the nasal airflow dynamics and due to the limited literature on the relationship between the nasal blockage and the airflow pattern, the computational geometry is altered to simulate various nasal cavities with obstructive disorders. The blockages are added to simulate cavities with deviated septum, enlarged lower and middle turbinate and nasal polyps. These conditions are the most common disorders that can lead to a

permanent nasal blockage. The calculated airflow fields from both normal and obstructed nasal cavities are then compared to investigate the influence of the nasal blockage on the airflow pattern. This forms the core of the thesis which assesses nasal blockages on the basis of airflow dynamics.

The external nasal airflow dynamics is also investigated experimentally using Particle Image velocimetry (PIV) on a scaled up silicon model of the nasal cavity constructed from the computational model, and the Schlieren optical technique on a human subject. The latter is of importance since it can be used on human subjects with no harm and little cost unlike the PIV technique. These experimental results are compared to the computational data of the external nasal airflow for validation.

In this work, a literature review on both the experimental and the computational studies on the nasal airflow dynamics is given in chapter 2. The computational and the experimental procedures are described in details in chapter 3 and 4 respectively. The calculations on the nasal airflow dynamics for the normal nasal cavity and cavities with obstructions are presented in chapter 5 and chapter 6. In chapter 7 the computational results are compared to the experimental data for validation. The final chapters include the discussion, conclusion and recommendations for future work.

1.5   Accomplishments

The accomplishments of this research are reviewed in this section.

- The in-house CFD code (*Lithium*) was used successfully to compute the steady laminar and steady (mean) transitional nasal airflow dynamics through a

computational nasal cavity model constructed from CT scan images of a healthy adult at both respiratory phases and for various flow rates.

- The computational code was modified and updated for the calculation of the external nasal airflow field. The internal and external nasal airflow fields were investigated for the normal nasal cavity and blocked cavities by adding the blockages at specific regions within the cavity. The influence of the most common conditions of nasal blockages on the nasal airflow pattern was considered in this study.

- The computational results of the internal nasal airflow field were compared against the available literature data for verification. The CFD calculations for the nasal airflow field outside the nostril were verified against experimental results produced in this study using a two dimensional Particle Image Velocimetry (PIV) and Schlieren techniques. For the PIV experiments, a 2.54:1 scaled silicon model was manufactured. The optical Schlieren technique was applied to human subjects without any difficulties. In general fair to good qualitative agreement was found between the CFD and the experiments where the differences were discussed.

- Variations in the nasal cavity's anatomical geometry were shown to significantly influence the nasal airflow, both inside and outside the nasal cavity. This supported the possibility of using the nasal airflow dynamics (specifically the external nasal airflow) to assess the nasal obstructive disorders. The nasal airflow was found to be laminar for normal breathing rates, and exhibited turbulent characteristics at higher inspiratory flow rate of 200 ml/s and higher.

2. Chapter 2

Literature Review

Under normal condition, the nasal cavity holds a specific aerodynamics geometry which allows for clear air passageways and provides ample time and contact for the nasal airflow so that the physiological functions of the nasal cavity are fulfilled sufficiently [31, 32]. Any disorder within the nasal cavity influences the nasal airflow and disturbs the physiological functioning of the upper respiratory system. There is no doubt that the knowledge of the nasal airflow patterns is a prerequisite for understanding nasal physiology, pathology and surgical treatment of disease of the nose [31]. However comprehensive understanding of the airflow field can be very difficult if based only on the rheological diagnostic tools available today and therefore other methods of studying the airflow patterns have been sought.

Studies of the nasal airflow patterns have been conducted for decades. Early attempts involved in-vivo observation of the airborne powder distribution [33]. The results from these studies were unsatisfactory and provided conflicting results due to the small size and the complex geometry of the nasal cavity. From late 1930s onwards in-vitro models were introduced by nasal cast of cadavers, allowing examination of airflow with various techniques. However these models made from cadavers suffered from inherent limitations associated with the post-mortem shrinkage of soft tissue or the use of flat transparent nasal septa for visualisation [34]. In the early 1990s nasal cavity models were made based on magnetic resonance

imaging (MRI) and computed tomography (CT) images. These images were used as templates to cut clear plastic or Styrofoam slabs which were then glued together serially to produce nasal cavity models. More recently Hopkins et al. [35] in 2000 established a procedure based on rapid prototyping and water soluble material for negative models which allowed constructing an accurate transparent model using high resolution CT scan data.

Experimental tools for nasal airflow measurements have also been varied over the years. Particle Image Velocimetry method currently is the leading experimental tool. This whole field measuring technique offers more advantages over other conventional one-point experimental techniques such as laser Doppler velocimetry and hot wire anemometer [36]. However creating an accurate transparent nasal model to represent the normal and abnormal characteristics of the cavity for application of PIV is quite challenging and very time consuming due to the small size and the complex geometry of the nasal cavity. It has also been suggested that a two dimensional PIV technique is short of providing an accurate description of the complex nasal airflow [37].

These difficulties involved with experiments led into investigation of the nasal airflow field by means of computational fluid dynamics (CFD). The recent developments in medical imaging, three dimensional geometrical modelling and numerical mathematics as well as computer science has opened new possibilities for physically realistic numerical simulations of nasal airflow based on anatomically precise computer models of the nasal cavity [38]. CFD allows detailed measurements of the local and global distribution of flow parameters without any intervention and

clinical risk for the patient. Considerable efforts have been put in computational research to predict the flow inside the nose and its relation to alternation in nasal geometry. It is hoped that this can lead to a computer assisted tool that will help to derive a criteria to better predict the outcome and improve the success of nose operation [39]. To begin the CFD process, initially a geometric model of the nasal cavity is required. This means either assuming a simplified geometry or obtaining a CT or MRI scan in its electronic format so that it can be loaded into a computer. For a realistic CFD flow calculation, the nasal cavities must be accurately represented in the geometric model. This requires closely spaced scan images, less than 2-mm which only became possible without exposing the patient to a large radiation dose after introduction of helical CT scanning. If this thickness becomes greater than 2.5 mm a decision on the margin between the airway lumen and the nasal mucosa becomes very difficult, restricting the accuracy of the nasal model [40]. This geometric model is then divided into smaller sections (cells) to create a mesh which can be either structured on unstructured. The flow equations are then solved numerically for each and every cell to give information about the flow parameters within the entire nasal cavity model.

2.1   Experimental Studies

The first quantitative in vitro velocity measurements were carried out by Procter et al. [41] using a miniature pitot device that was introduced into the flow passage of a nasal model made from the nasal cast of a cadaver. The flow pattern was visualised with the aid of a transparent plastic flat plate replacing the nasal septum and a dye

injection outside the nostril into a steady flow of water. Flow visualisation suggested that the majority of flow passes the middle airway and a small fraction separates upward forming a standing eddy in the olfactory region. Flow was also found to be laminar at flow rate of 125 *ml/s*. Turbulent flow was detected downstream of the nasal valve as the flow rate was increased to 208 *ml/s*. The resolution of the experiment was rather poor due to the small size of the cast model and results were limited as a result of interaction of the Pitot tube with the airflow.

In 1983 non-invasive measurement of velocity fields in a life size nasal model was conducted by Girardin et al. [42] using Laser Doppler Velocimetry (LDV) for the first time. A transparent model of the nasal cavity was made from the imprint of a normal human nasal cavity and pharynx. The LDV provided information about the velocity field by measuring the speed of water particles suspended into the air flow of 166 *ml/s* passing through the nasal cavity model. High velocities were observed at the floor of the nasal cavity in the area located immediately posterior to the luminal valve. This high velocity was believed to be due to the directional effect of the luminal valve where the flow undergoes a significant directional change. The turbinated area had a streamlining effect by making the flow field more uniform with lower peak velocities. Flow was also found to be greater in lower half with larger velocities near the septum. Flow patterns were quite different at inspiration and expiration and the velocity profiles suggested a turbulent flow despite the low value of Reynolds number.

Hornung et al. [33] constructed an anatomically correct model of the nasal cavity for the first time. Flow pattern was studied by infusion of radioactive Xenon gas 133

into a continuous flow of air through the model. The radioactive gas was released into the airstream at five different release sites in the nostril and for each of these positions the flow field was investigated at three different flow rates of 42, 117 and 334 *ml/s*. Distribution of radioactive gas was captured using a Scintillation camera to detect the γ rays released by radioactive xenon. Results confirmed some of the early studies who used water as the carrier medium [43, 44] by finding the majority of flow to be in the lower nasal airways and an increase in flow in the olfactory region at the elevated flow rates. Although the flow pattern varied significantly among the five positions of the release site, but turbulence was observed in the initial nasal area regardless of the position. In this experiment however detailed flow visualization was limited due to the small size of the model. Therefore, Schreck et al. [45] and Hahn et al. [46] constructed an anatomically accurate enlarged scale model of the cavity.

Schreck et al. [45] constructed a 3:1 scaled replica of a half nasal cavity based on the magnetic resonance images (MRI) spaced in 4-mm increments of the skull of a healthy male subject. Templates were formed from scaled MRI data and were cut into Plexiglas plates to form the nasal model. Pressure measurements, flow visualization and hot wire anemometry studies were performed at flow rates of 50 to 1500 *ml/s*. Point wise velocity measurements with a hot film anemometer revealed, an initial acceleration of the flow from the nostril to the nasal valve followed by a rapid deceleration due to the sudden expansion in the main airway. This expansion created an adverse pressure gradient that led to formation of two distinct inspiratory vortices, one located in the upper part of the main nasal airway and the smaller one in the lower part of this section Figure 3 .
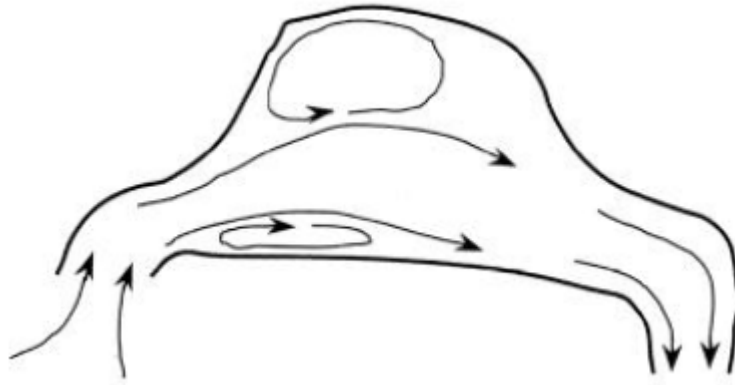
Figure 3: Sketch of flow pattern observed in scale model of nasal passage during steady inspiration, showing two separation vortices [45].

Dye injection into these vortices showed a little exchange between the upper vortex and the main stream as the dye persisted for a period of 1 second, whereas dye in the other vortex was immediately washed out downstream. Since the location of the upper vortex coincided with the location of the olfactory membrane, it was then suggested that the circulation of flow in the vortex transports the air along the membrane, enhances the exchange of the air at the sensing organs and prevent the sensitive olfactory membrane to be directly exposed to the high velocity air stream but rather to weaker secondary flow. During breathing at rest the nasal flow was suggested to be transitional with turbulent at flow rate of 200 *ml/s* and higher. The majority of inspired flow was also found to pass through the combined middle and lower airways and only small fraction through the olfactory region at all flow rates. These results correlated well with results from earlier studies [41, 42]. Nasal resistance was calculated by measuring the transnasal pressure at different volume flow rates. It was shown that 43% of the total nasal resistance comes from the anterior region of the nasal cavity around the nasal valve area whereas the main

airway and the nasopharynx only contribute 25 % and 32% respectively. Finally the model was modified using modeling clay to decrease the cross sectional area of the airway in order to simulate nasal local constriction in the cross section to study the influence of the nasal congestion and collapse of the external nares. The experiment showed that the reduction of cross sectional area in the nasal vestibule increases the size of the vortices for a given flow rate and was followed by a dramatic increase in the value of nasal resistance.

Hahn et al. [46] greatly improved the spatial resolution of velocity measurements in the nasal cavity by building a 20:1 scaled replica model of the nasal cavity from computerized axial tomography (CAT) scans recorded in 2-mm increments from the tip of the nares to the beginning of the nasopharynx. The outlines of the scaled CAT scan data were cut out of Styrofoam slabs, which were then glued together to form the nasal model. The flow field was investigated at steady flow rates of 180, 560 and 1100 *ml/s* using a hot film anemometer. The flow field in inspiration was found to be independent of the flow rate, with 50% of flow passing through the posterior end of the inferior and middle airways, and 14% through the olfactory region. The flow was determined to be turbulent at the two higher flow rates and mainly laminar at the lowest flow rate. Nasal hairs were also modelled using copper wires and were found to have a negligible effect on the velocity profile downstream of the nares.

Brucker et al. [47] were first to use the two dimensional particle image velocimetry technique to measure the instantaneous flow field measurement on a 3:1 enlarged scaled model of the nasal fossa. Results showed a separation region anterior to the middle turbinate which led to a narrow passage for the air to flow towards the

olfactory region in which the flow accelerated and caused significant portion of high velocity in the olfactory region. The flow was also mainly found to pass through the middle and upper airways in inspiration, and lower and middle airways in expiration with highly irregular and non uniform pattern just before the turbinated region. Another flow separation was also observed in the expiration posterior to the middle turbinate. This study however was limited due to the low resolution of the anatomic data used for model generation.

Simmen et al. [48] made a model using a 55 years old cadaver nose with no nasal abnormality. The septum was replaced by a transparent replica to allow visualisation of an anatomically correct model. The cavity was connected to a piston pump in an airtight fashion, which simulated the respiration. For visibility of airstream water particles were aerosolised by an ultrasonic generator. The airflow was recorded with photographs and a videotape recorder for both decongested and congested nasal cavities at flow rates of 167, 384 and 584 *ml/s*. Three different structures were constructed to simulate congested nose using a modelling paste, to enlarge the turbinates , creating a septal spur and study the effect of turbinectomy by partially resecting the inferior turbinate. The flow pattern observed on real time showed that inspiration is divided into three phase of acceleration for 0.6 seconds, a near steady state phase of 1.6 second followed by a deceleration of 1.1 second. In expiration only two phases of acceleration and deceleration were observed. In most parts of the nasal cavity partially turbulent flow was reported with it onset occurring in the nasal valve region during the entire steady state phase. Turbulent flow is reported in other references [33, 44-46, 49]. The amount of turbulence was increased as the flow rate

was increase. This increase in the flow rate and hence the velocity, shortens the acceleration and deceleration, causing the near steady state to be reached sooner and therefore dominate the flow. The flow was mainly found to pass over the head of inferior turbinate through the middle airway. Same result was found in previous works [33, 44]. More evenly distributed streamlines were observed with increasing the flow rate as more air flew through the lower and upper meatuses. There were no changes in the phases of flow for congested cavities but flow patterns were altered depending on the geometry. In the case of septal spur the flow was deflected significantly towards the inferior and middle airways whereas for the enlarged turbinate and the cavity model with turbinectomy, streamlines were concentrated exclusively in the middle airway and along the floor of the nasal cavity, respectively.

Kelly et al. [7] studied the flow patterns using PIV in the nasal cavity model based on Hookins et al. [35] method. In this method an accurate model of the complex internal anatomy of the nasal cavity was made from rapid prototyping and liquid translucent silicone consolidation technique which utilized CT images. The flow measurement for a non-oscillatory flow rate of 125 *ml/s* suggested smaller fraction of the flow in the olfactory region in both inspiration and expiration, than reported by Hahn et al. [46]. The amount of flow appeared closer to the lower end of Stuiver's [43] observations which was 5 %. This difference may be due to the geometrical variation between the two nasal models studied. Only a small fraction of flow was found to pass through the meatuses confirming the results of some previous works [45, 46, 50]. Peak velocities were observed in the nasal valve due to its small cross

sectional area and along the nasal cavity floor in the inferior airway where the resistance was the least to the flow.

Kim et al. [51] constructed a cast of the nasal cavity obtained by a combination of rapid prototyping which was fed by high resolution CT images at 1-mm thick of a healthy individual and solidification of clear silicone. This model was connected to a pump which simulated a physiological pressure in the upper airway system for the flow volume of 125 *ml/s*. A glycerol-water mixture was used as the flow material. The airstream was marked using spherical polyvinyl particles that could be observed through the solidified clear silicone model. Flow visualisation revealed that in both respiratory phases the main nasal passageway is the middle airway where the flow was also found to be mainly laminar. Highest velocities were reported to occur in the superior airway in contrast to Kelly et al. [7] despite using the same method to investigate the flow field. This disagreement between the two studies is believed to be a result of having different inlet structures to the nasal cavity models. Occurrence of turbulent flow was also reported in this experiment at a low flow rate of 125 *ml/s* confirming the work of Simmen et al. [48] with its onset in the nasal valve region in inspiration and the nasopharynx in expiration.

2.2   Computational Research

Elad at al. [52] for the first time conducted a numerical simulation of steady incompressible laminar flow through a three dimensional trapezoidal geometry which resembled the functional structure of the nasal cavity. Due to the memory limitation a first order simulation was produced by applying linear Stokes equations

which neglects the convective terms in the momentum equations. Initially the flow was investigated for the nose-like cavity without the turbinates. Then the effect of turbinates-like structures modelled as plates was studied by adding them one at the time. Results suggested that the largest flow flux is along the floor of the cavity where resistance to the air flow is the lowest. The turbinate structure plates determined a path for the airflow and directed the flow towards the olfactory region. Flow patterns were found to be similar in both respiratory phases with flow being more uniform in expiration which is believed to be a result of the geometry of the nasal cavity. Similar results have been reported in other references [42, 45] but the role of turbinates are in conflict with the results reported in [53]. This confliction may be due to the inaccuracy of nasal models in both studies. In this experiment a trapezoidal geometry was used to model the nasal cavity and the turbinates were modelled as wing shaped projections (plates). In addition only a linear equation of motion was solved which showed up to 20% deviation when the flow analysis was compared to the non-linear model.

Keyhani et al. [54] for the first time created a finite element model of a human nasal cavity obtained from axial CT scans of the experimental model used by Hahn et al. [46]. Flow equations were solved for a quasi steady, laminar flow at breathing flow rates of 125 and 200 *ml/s* using the commercial CFD package FIDAP. The results confirmed the laminar nature of the nasal airflow for quiet breathing which was found in Hahn's experimental work. For the inspiratory phase, about 30% of the flow was found to pass through the lower airway and 10% through the olfactory. Highest velocities were reported at the floor of the cavity and at the mid way

55

between the septum and the middle airway. Secondary flows were induced by the curvature and the rapid changes in cross sectional area with relatively low velocities compared to the axial velocity in most of airway. At expiration the peak velocities were smaller than the inspiration phase and the flow field was more uniform. No changes were observed in the flow pattern as the flow rate was varied and the overall flow was found to be laminar inside the cavity. These results were validated by comparison with the experimental data by Hahn et al [46] and showed a good agreement.

Subramanian et al. [55] for the first time reported the use of computer tomography CT scan to form a realistic nasal model for the CFD calculations. In this work the steady laminar nasal airflow was investigated in an attempt to improve Keyhani's [54] work by reconstructing the both sides of the human nasal passages which included the posterior nasal airway and the nasopharynx, the two parts that were excluded in Keyhani's [54] model. To determine the airflow profile at resting and for a light exercise, two volume flow rate of 250 and 433 *ml/s* through both nasal cavities were investigated. Calculations showed strong secondary components in the anterior and posterior regions of the nasal cavity while largely streamlined and smooth in the main nasal passages. The nasal airflow was laminar for both volume flow rates confirming Keyhani's [54] and Hahn's [46] studies. Swirling air currents and recalculating flow were predicted in the nasal vestibule as a consequence of an abrupt change in the slope of the nasal roof rising vertically upwards from a nearly horizontal orientation in the anterior region. Also the expansion in the nasopharynx gave rise to two downwards counter currents spiralling vortices. The flow field was

found to be independent on the flow rate with the peak velocity located at the posterior region of the nasal valve and no flow separation in the main nasal cavity.

Sarangapani et al. [56] studied the airflow field through the extrathoracic airway computationally assuming incompressible flow under steady state condition adapting an approach similar to Subramanian et al. [55] . The flow patterns were found to be similar at two flow rates 125 and 200 *ml/s*. The highest airspeed in the main airway occurred along the nasal floor towards the septum in the anterior part, moving towards the lateral wall as the flow moved forward. The middle airway was the passageway for the second highest velocity where the superior region contained the lowest air velocities close to the nasal roof. Similar results were also found in [54, 57].

Horschler at al. [39] employed a structured mesh solver with an advective upstream splitting method to study the airflow pattern of a nasal cavity model. Results (Figure 4) for the inspiratory phase revealed a pronounced twisting of streamlines through all airways. This was explained to increase the time spent by the airflow within the main nasal airway and therefore enhance the conditioning. In expiration the airflow was shown to mainly pass through the middle and upper airways as the tip of the inferior turbinate was located outside the main flow regime. These computational results were compared against the experimental data of Park's worked [47] which showed a good agreement.
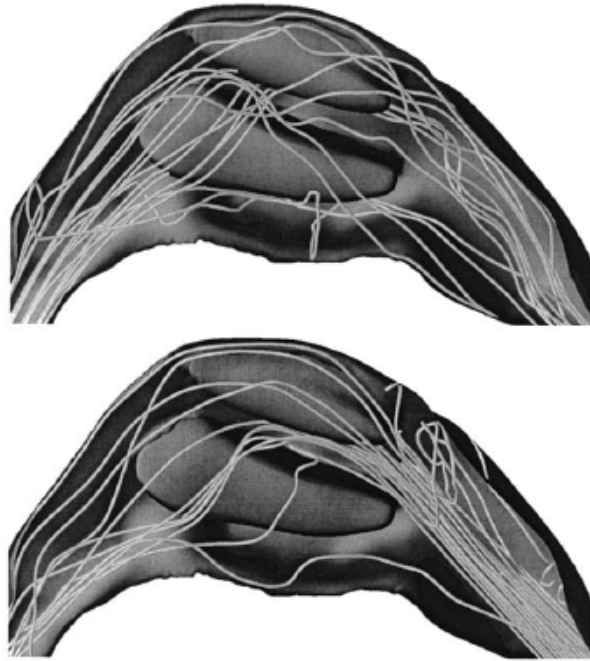
Figure 4 : Streamlines at inspiration (Top) and expiration (Bottom), showing more twisting in inspiratory phase and more uniform flow field in expiration [39].

Weinhold et al [38] studied the inspiratory nasal airflow dynamics using both computational and the experimental tools for a wide range of flow rates up to 1400 *ml/s*. Various models were constructed based on an established in vivo casting technology [31] representing both normal and abnormal nasal cavities. The numerical simulation were carried out using an enhanced $k - \varepsilon$ turbulence model and were compared against the experimental data using the same methodology as in Mlynski's work [31]. The result showed that the airflow passed through the entire surface of the turbinated region. The obstructed cavities were accompanied by an increase in nasal resistance and the turbulent intensity. For the nasal cavity with an inferior turbinectomy two recirculation zones were observed, one located in the olfactory region and the other along the floor of the nasal cavity before the head of

the inferior turbinate. This was later confirmed by Croce et al. [58]. There was a good agreement between the computational and the experimental pressure flow curves for all nasal cavity models. This study was limited to provide detailed information about the airflow field since the results only contained few streamlines and pressure drop figures.

Zhao et al. [59] in 2004 developed a method which allowed a quick conversion (few days) of CT scans of the nasal cavities to a 3D numerical model. Applying this method, a model of the nasal cavity including the nasopharynx of a human subject was used to predict a laminar and quasi-steady nasal airflow for the respiratory rate of 248 *ml/s* through both nostrils. This model was also modified to depict various anatomical deviations to investigate their influence on the airflow pattern. These modifications were made in two specific regions, the nasal valve and the olfactory region. Distribution of air flow within the cavity showed that the highest velocities occur along the nasal floor of the lower airway, second highest at the middle airway close to the septum and the lowest velocities in the superior region in both respiratory phases. These results are in a good consistency with those from previous literature [46, 54]. In inspiration only 10 % of the airflow passed through the olfactory region which is in the range of previous reports [7, 43, 46]. The slight variation in the amount of air through the olfactory region is probably due to the differences in the geometries of the nasal cavities studied. Modifications on the model showed that any changes in the airway volume of the valve section, strongly influences the airflow patterns through the whole cavity and hence the nasal valve acted as a key controlling region for regulating the total airflow through the nostril

and the local airflow at different region especially the olfactory. Also changes in the airway volume of the olfactory slit were followed by changes in the local air flow without any influences on the flow elsewhere. The flow through a specific region was suggested to be originated at a specific location on the external nares with no flow separation of vortices in an uncongested nose. Only few recirculation streams were observed in the nasal vestibule and nasopharynx. For the cavity with a slight nasal obstruction in the nasal valve region however, the flow started to separate close to the blocked region forming two vortices in the anterior upper nasal airway and posterior upper part of the nasal cavity close to the olfactory region.

Grant et al. [60] studied the flow in an anatomically accurate model of the left passage of a healthy adult male both computationally and experimentally. The physical and numerical models were from the same CT scan images to achieve the highest possible degree of geometrical similarities. For experiments the PIV technique was applied and for computations, the steady incompressible Navier stokes equations were solved considering both laminar and turbulent flows. For the turbulent flow difference two equation models were tested where the result presented was only based on the RNG $k - \varepsilon$ model. Good correlation between the two results validated the numerical techniques. The experimental and computational pressure flow curves were similar. In both laminar and turbulent conditions the measurements agreed within 6% of the experimental data. The very close agreement between the laminar and the turbulent predictions suggested that the influence of turbulence on the flow was very low, indicating that laminar flow predominates at the considered resting breathing rates. Even at higher flow rates the laminar flow assumption did not

have a significant effect on the accuracy of predictions. The flow was found to be dominated by a separation at the posterior end of the nasal floor and a large recirculation zone was formed along the inner walls of the nasopharynx.

Ishikawa et al. [61] carried out a numerical investigation of a nasal and pharyngeal cavity constructed from a computed tomography images of a healthy adult. The flow was considered to be unsteady, laminar and incompressible. A complete respiration cycle of 5.2 s including a 0.1 s, zero mass flux period between the inspiration and expiration, called as the resting phase was simulated using Fluent. In inspiration the highest velocity in the nasal cavity occurred along the middle meatus with the lowest velocity recorded in the superior regions of the nasal cavity. High vortices were recorded at the anterior portion of the nasal cavity and at the area close to the middle turbinate at the posterior portion of the nasal cavity, regions with sharp velocity gradients. The resting phase in this study is numerically questionable since it does not suppress the unsteady flow phenomena caused by the changed flow direction between inspiration and expiration. Similar velocity measurements were reported by Shi et al. [62] who simulated the transitional laminar airflow fields and nanomaterial depositions using a MRI derived model of representative nasal cavities.

Horschler at al. [63] studied the nasal airflow dynamics both experimentally and computationally using an identical model of the cavity which only included the lower and middle turbinates. Experimental data were taken using PIV technique on a transparent model. Numerical simulation, assuming steady incompressible laminar equations were carried out using a finite volume approach of block structured curvilinear grids. Results from computations and experiments were similar and

suggested that the flow patterns in expiration were almost independent on the Reynolds number, whereas in inspiration an increase in Reynolds number was accompanied by a generation of vortices. Flow was found to be laminar along the cavity and more susceptible to changes of cavity's geometry in inspiration. The turbinates were found to serve as a guide vein to ensure homogeneous velocity distribution in the lower, centre and upper channel between the nostril and the throat. The lower turbinate was shown to posse the major impact on velocity distribution since this is the part of cavity which primarily interacts with the flow immediately after sudden expansion. Later this reference was used in a study [64] to validate a numerical investigation of a incompressible flow field in a nasal cavity model constructed based on brucker's work [37] and lattice Boltzmann numerical method. The comparison showed a good agreement between the two studies.

Leedan at al. [65] carried a numerical study of unsteady incompressible flow field on a staggered rectangular grid using a second order central scheme for the diffusion terms and a second order WENO scheme for the convection terms. The computational model was generated from the computed tomographic (CT) scans and the flow through the model was driven by a time varying transnasal pressure up to 200 Pa. In this work, highest flow velocities were found to be in the nasal valve region and lowest in the inferior and the middle meatuses. The area with highest velocities was found to have an irregular pattern which was caused due to a vortex generated between the nasal valve and the head of the inferior turbinate. In overall the velocity contours were quite similar in both respiration phases only with slightly higher velocities in expiration. The volumetric flow rate distribution was found to be

similar regardless of the transnasal pressure which was in agreement with the experimental data in [66]. The flow was shown to pass through the combined inferior and middle airways, while the olfactory slits and the upper airway contributed about 15% and 10% respectively. Similar results were reported in other numerical investigation of airflow field [67] using two models of nasal cavity derived by spiral and cone beam CT scans for comparison.

Wen et al. [68] conducted a numerical investigation of a steady laminar flow through a model based on CT scan images of a healthy 25 years old nasal cavity. The finite volume approach was used with a third order accurate QUICK scheme for the approximation of the momentum equation and the SIMPLE method for the pressure-velocity coupling. Two flow rates of 125 and 250 *ml/s* were imposed through both cavities, to simulate light adult breathing. The differences in geometry between the left and right sides of the cavity as well as inter-subject variations provided a different flow pattern. Highest wall shear stresses were found in the nasal valve region which was the region of the peak velocity. The nasal valve was shown to contribute to the majority of the nasal resistance. Flow observation revealed the presence of vortices in the upper olfactory region and just posterior of the nasal valve, where the geometry began to expand and experienced sharp changes. These vortices appeared and were reported in other studies [54]. There were also multiple secondary flow regions in the valve area just underneath the middle part where the bulk of flow travelled. The majority of flow within the valve region was found to stay close to the septum and only a small portion reached the olfactory region.

Ishikawa et al. [69] studied the unsteady, incompressible flow using the same model in Ishikawa's previous investigation [61] with modelling assumptions and parameters adjusted to fit the observed properties of physiological human nasal respiration and sniffing. In this work two re-circulating flows were observed in the same location as previously reported in [54, 68] who measured the flow field under steady and quasi steady assumption. Also it was shown that the location of the upper most streamline is displaced closer to the olfactory area as the velocity was increased in inspiration. The olfactory velocity and streamline profiles were consistent with those obtained by Zhao and Croce [58, 59].

Wang et al. [70] recently investigated the air flow pattern and detailed local deposition patterns of the micron and submicron particles in a computational model of the nasal cavity built from CT scans, under different steady laminar flow rates using a Lagrangian approach. The flow streamlines were captured by tracking the path traversed by particles released from the inlet of the cavity. Results showed different streamlines for different injection locations. The streamline released from the anterior half of the nasal cavity was shown to go through the upper, middle and lower airways with the majority of flow passing through the middle and lower airways, while most of the streamlines from the posterior half was shown to flow along the floor of the cavity. This confirmed Zhao et al. [59] observations. Different flow patterns were also observed for each side of the nasal cavities. While for the left nasal cavity a flow separation and a reversed flow was observed posterior to the nasal valve at the olfactory region, for inspiratory flow rate of 125 *ml/s*, no recirculation was observed at the right nasal cavity. As the volume flow rate was

increased to 250 *ml/s*, the reversed flow became smaller and moved further towards the back of the cavity and two vortices were formed in the right nasal cavity at the olfactory region and at the back of the nasal cavity. These differences in the flow pattern may be due to the small differences in the geometry of each sides of the nasal cavity.

Tan at al. [71] investigated the airflow characteristics through the nasal airways and sinuses computationally using a cavity model based on the CT images of 0.625 mm thickness of a Chinese adults' nose with normal nasal structure and function. The steady incompressible Navier Stokes equations were solved using a k-e turbulent model at a breathing respiratory rate of 125 ml/s. The respiratory airflow was generally found to be laminar and passed through the entire nasal cavity. The inspiratory streamlines showed a changed into the horizontal direction before reaching the nasal valve where the flow gained velocity. This also resulted into an increase in both pressure and wall shear stress. The regions of high wall shear stress were shown to be similar to the regions with sharp velocity region. This behaviour is also reported in other studies [72, 73]. The velocities were also higher towards the nasal septum. Immediately after the nasal valve, the flow was shown to form small vortices and twisted streamlines, all located at the anterior region where they transformed to laminar flow before reaching the posterior part. The computed expiratory calculations revealed much smoother streamlines, without any vortices or turbulences.

3.   Chapter 3

Computational Procedure

The nasal airflow is cyclic and has a typical time period of 5 seconds. However for relevance to the experimental procedure where the flow measurements are taken from steady inhalation or exhalation, the in house CFD code *Lithium* is used to calculate steady (in the mean) incompressible flow for a nasal cavity topology of a healthy adult patient taken from CT scans. This code has already been used successfully to simulate the nasal cyclic airflow [29]   and simulated flow of transitional and turbulent nature [74]. To account for the possibility of turbulence the low Reynolds number $k - \omega$ Reynolds-Average-Navier-Stokes (RANS) model is used [30, 75]. The Navier-Stokes equations are solved using the projection method and an implicit 1st order time marching scheme. The Van-Leer TVD second order scheme is used for the convective terms and a second order central scheme is used for diffusion terms. A rectangular staggered grid is used along with no-slip wall boundary conditions. The nasal airflow is calculated over the entire nasal cavity as well as for an area outside the nostril.

3.1   Governing Equations of Fluid Dynamics

Nasal airflow is modelled using the steady incompressible Navier Stokes Equations. A Mach number of <0.3 certifies the incompressibility assumption. Steady inhalation and exhalation are to be considered in this study since one of the

aims is to simulate and measure the nasal flow of a patient blowing air for a few seconds. The low Strouhal number of $St = \dfrac{fL}{U} = 0.3$ (where f is the breathing frequency, L is the axial characteristic length of the nasal airways and U is the average velocity in the nasal cavity) at normal breathing also supports the approximation of steady inhalation or exhalation for investigating the normal breathing cycle.

The flow of the mucus as well as the deformation of the turbinates due to the nasal cycle is not considered, since these changes caused by the small velocity of the mucus and the large time scale of the nasal cycle have a negligible effect on the nasal airflow dynamics [76].

Two flow conditions are considered, the first strictly laminar and the second of possible turbulence, modelled using the low Reynolds $k - \omega$ RANS model.

3.1.1 Laminar Flow

The incompressible Navier-Stokes-Equations (NSE) are governed by the continuity, momentum and energy equations as follows:

Continuity;

$$\frac{\partial u_i}{\partial x_i} = 0 \qquad\qquad 3.1$$

Momentum;

$$\frac{\partial u_i}{\partial t} + u_j \frac{\partial u_i}{\partial x_j} = -\frac{1}{\rho}\frac{\partial P}{\partial x_i} + \nu \frac{\partial^2 u_i}{\partial x_j^2} \qquad\qquad 3.2$$

Energy;

$$\frac{\partial T}{\partial t} + u_j \frac{\partial T}{\partial x_j} = \frac{1}{\rho c_p} \frac{\partial^2 T}{\partial x^2_j} \qquad\qquad 3.3$$

Where u, t, ρ, P and ν are the velocity field, time, density, pressure and kinematic viscosity respectively. At a temperature of $30^\circ C$, the air density and kinematic viscosity are $1.164 \times 10^{-3} \, g/cm^3$ and $0.160 \quad cm^2/s$ respectively. The time derivative in the momentum equation is kept and equations (2.1) and (2.2) will be marched in time until a steady solution is found for steady inhalation and exhalation. The energy equation is uncoupled for an incompressible flow since the dynamic viscosity coefficient is taken as constant. Once the flow field is known the temperature field can be calculated using the energy equation [77].

3.1.2 Boundary Conditions

The nasal cavity is assumed to be symmetrical in the lateral direction which allows the consideration of one cavity only. This helps to reduce the computational cost. The walls of the nasal cavity are considered to be rigid, ignoring the valvular deformation, given that the maximum flow at which the nasal valve collapses is far above the flows considered here [78]. As a result of this assumption, no penetration and no slip boundary conditions are applied for the velocities (i.e. $u = 0$). For the pressure a Neumann boundary condition is employed at the wall (i.e. $\frac{\partial p}{\partial n} = 0$) following the projection method. Zero values and zero gradient values are imposed at the inflow and outflow boundaries respectively for the transverse velocities while the

inlet normal velocity is given. The phase of respiration is decided based on the directions of the normal velocity at the nares or nasopharynx. [77].

An image of the nasal cavity is plotted in Figure 5, where the location of the nostril and the nasopharynx are indicated which are the inlet and outlet to the flow depending on the respiratory phase.
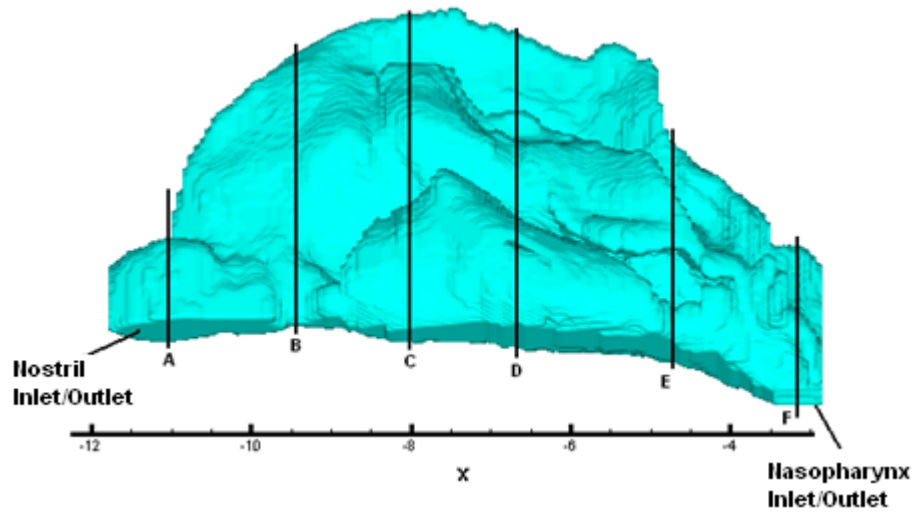
Figure 5: Sagittal view of the nasal cavity, indicating six sections of A: Nasal vestibule, B: Nasal valve, C: Anterior region of the main nasal airway, D: middle section of the main nasal airway, E: Posterior region of the main nasal airway and F: nasopharynx.

3.1.3 Turbulent Flow

The governing equations are derived using the Reynolds decomposition, which replaces all fluid properties in equation (3.2) by the sum of a mean ($\bar{\phi}$) and fluctuating component (ϕ'). These equations are called the Reynolds- Average-Navier-Stokes (RANS) equations which are as follows:

Continuity:

$$\frac{\partial(\bar{u}_i)}{\partial x_i} = 0$$

3.4

Momentum:

$$\frac{\partial(\bar{u}_i)}{\partial t} + \frac{\partial}{\partial x_j}(\bar{u}_i\,\bar{u}_j + \overline{u_i'u_j'}) = -\frac{1}{\rho}\frac{\partial \bar{P}}{\partial x_i} + \nu(\frac{\partial \bar{u}_i}{\partial x_j} + \frac{\partial \bar{u}_j}{\partial x_i})$$

3.5

Equations (2.4) and (2.5) are solved for $\bar{u}_i$ and $\bar{P}$, i.e. the Reynolds averaged properties which in our case are the mean flow properties. The $\overline{u_i'u_j'}$ term is the Reynolds stress which needs to be modelled. For this the $k-\omega$ model which was proposed by Wilcox, based on the Boussinesq eddy viscosity approximation is applied. In this model the Reynolds stresses are linked to the mean velocity gradients via turbulent viscosity as follows:

$$\overline{u_i'u_j'} = -\nu_t(\frac{\partial \bar{u}_i}{\partial x_j} + \frac{\partial \bar{u}_j}{\partial x_i}) + \frac{2}{3}\delta_{ij}k$$

3.6

Where, k and ν_t are the turbulent kinetic energy and the turbulent kinematic viscosity. Wilcox $k-\omega$ model is a two equation model, where the velocity scale and the length scale are described by equations for turbulent kinetic energy and specific dissipation respectively. The exact transport equation for kinetic energy is derived using the Navier Stokes equations. The model k equation is then derived by modelling the unknown terms which are the production, turbulent diffusion and dissipation. The pressure diffusion term is neglected since it is small.

Using dimensional analysis the kinematic eddy viscosity is taken as:

$$v_T = \frac{k}{\omega} \qquad\qquad 3.7$$

The modelled k equation is:

$$\frac{\partial k}{\partial t} + \bar{u}_j \frac{\partial k}{\partial x_j} = \tau_{ij} \frac{\partial \bar{u}_i}{\partial x_j} - \beta^* k\omega + \frac{\partial}{\partial x_j}\left[(v + \sigma^* \frac{k}{\omega})\frac{\partial k}{\partial x_j}\right] \qquad\qquad 3.8$$

And the equation for the specific dissipation rate ω is:

$$\frac{\partial \omega}{\partial t} + \bar{u}_j \frac{\partial \omega}{\partial x_j} = \alpha \frac{\omega}{k} \tau_{ij} \frac{\partial \bar{u}_i}{\partial x_J} - \beta\omega^2 + \frac{\sigma_d}{\omega} \frac{\partial k}{\partial x_j} \frac{\partial \omega}{\partial x_j} + \frac{\partial}{\partial x_j}\left[(v + \sigma \frac{k}{\omega})\frac{\partial \omega}{\partial x_j}\right] \qquad\qquad 3.9$$

The closure coefficients and auxiliary relations can be found in reference [30] for a low Reynolds number flow.

3.2   Numerical Discretization

The computational domain is divided into a finite number of discrete points using the staggered mesh approach where the pressure is located at the centre of the cell and velocities are located at the sides of the cell. The laminar NSE (3.1) and (3.2) or the RANS equations (3.4) to (3.9) are marched in time implicitly using the projection method to avoid the severe time step constraint of an explicit time marching which is found to be too restrictive in the nasal flow due to the CFL condition [79].

The Spatial derivatives are approximated using the finite difference 2nd order central and the Van Leer TVD schemes for the diffusion and convection terms respectively.

3.2.1 Computational Domain

The nasal geometry was constructed from available tomography (CT) scans of a human head which have been examined and found to be free of nasal obstruction. The data set of 191 coronal CT scan slices with an in plane resolution of 0.80 mm and slice to slice separation of 1.0 mm has been processed by Amira ^{TM}, a commercial 3D image processing software package. After segmenting the CT image data into the region that contained the nasal airways, a smoothness algorithm has been applied to remove any non-smooth areas and a three dimensional triangular surface mesh representing the surface of the nasal cavity was generated. However the mesh was then converted to a structured rectangular grid using a cut-cell approach, since the in-house CFD code is based on a structured grid and an irregular grid cannot capture the complicated structure of the nasal cavity. This was accomplished by embedding the triangular surface mesh in a three dimensional Cartesian box grid with different uniform spacing along the x, y, and z direction. All grid cells are located either fully inside the flow region or fully outside the geometry [29].

3.2.2 Staggered Mesh

A Staggered grid type was first introduced by Harlow and Welch in (1965) [80]. This mesh type is mainly used on structured grid for simulation of incompressible flow to avoid some problems associated with the collocated mesh approach. The idea of staggered grid is to evaluate scalar variables such as pressure and temperature at the centre of the cell and the velocities on its faces. The staggering of the velocity allows avoiding the unrealistic behaviour of the discretized momentum equation for

spatially oscillating pressure. Another advantage of using staggered grid arrangement is that the velocities are generated exactly at locations where they are required for scalar transport convection-diffusion computations and hence no interpolation is needed to calculate velocities at the scalar cell faces [79].

3.2.3 Spatial Discretization of Diffusion Terms

The second derivative diffusive terms are discredited using the 2nd order central scheme which is as follows:

$$(\frac{\partial^2 u}{\partial x^2})_{i,j,k} = \frac{u_{i+1,j,k} - 2u_{i,j,k} + u_{i-1,j,k}}{\Delta x^2} + 0(\Delta x^2) \qquad\qquad 3.10$$

This is obtained using a Taylor series expansion.

3.2.4 Spatial Discretization of the Convective Terms

The 1st order upwind scheme is the most stable and unconditionally bounded scheme but it also introduces excessive numerical damping due to its low order of accuracy (first order). Higher order schemes such as central differencing or QUICK although improve the accuracy, also give rise to numerical oscillations particularly near steep gradients and shock waves (in compressible flows) when the slope in a cell becomes larger than the difference of adjacent mean values [81, 82].

For the discretization of the convective terms, it is desirable to use a scheme that has the accuracy of high order and the stability of first order schemes. There are certain conditions which, if are met by the differencing scheme will provide non oscillatory behaviour. An example of such a condition is the concept of bounded total variation

(TV) for non-linear equations which has been introduced by Harten (1983) [83]. Total variation (TV) of a quantity ϕ of a discrete solution is defined as:

$$TV(\phi^n) = \sum_i \left| \phi_i^n - \phi_{i-1}^n \right|,$$ 3.11

However families of such schemes which meet this condition are of 1st order accuracy. In order to achieve higher order schemes which satisfy this condition a non linear component is introduced under the form of limiters which control the gradients of the computed solution to prevent the appearance of over or undershoot [79, 83]. If it is required the limiter switches between a second order accuracy when the solution is smooth to first order upwind in the vicinity of high gradients.

For convective terms this flux limiter is initially added to increase the order of the discretization scheme which in this case is only called a convective flux. This flux differs for different high order scheme. The convective flux becomes the flux limiter if it is rearranged in terms of successive gradients on the solution domain. If the flux limiter constrains or limits the flux of the conserved quantity into a control volume to a level that will not produce new overshoots and undershoots (oscillations) in the solution, the scheme is monotonicity preserving. Monotonicity preserving schemes have the property that the total variation of the discrete solution should diminish with time and therefore are called TVD class schemes.

$$TV(\phi^{n+1}) \le TV(\phi^n)$$ 3.12

In this work the Van Leer flux limiter is used which is described as follows:

$$\psi(r) = \frac{r + |r|}{1 + r}$$ 3.13

Where $\psi(r)$ and r, are the flux limiter and the ratio of two successive gradients respectively.

3.3   Method of Solution

If a time dependant mathematical model is used for a steady problem, the solution has to be marched in time until the steady state is reached. This family of methods is called the time marching [84]. Here a 1st order implicit method is used. The implicit scheme gives equations which involve more than one unknown at the same time level. Although using this scheme requires high number of operations, nevertheless a smaller number of iterations will be required to reach the steady state since there is no numerical limit on the time level as compared to the explicit scheme where the time level is restricted by a CFL condition.

3.3.1 Pressure Solution

Solution to the incompressible Navier Stokes equation can be complicated because the pressure term lacks a time derivative. When dealing with compressible flow, the continuity equation yields a time derivative for the density. The pressure term is then determined using an equation of state which links the pressure to the density. However in incompressible flow condition, the density is no longer linked to the pressure. In this case the continuity equation becomes a constraint to the solution of the flow field. In order to overcome this problem the pressure is obtained by solving a Poisson equation derived by the projection method.

3.3.2 Projection Method

The projection method was proposed independently by Chorin (1968) and by Temam (1969) [85]. In its original form, this is a fractional step method with a first order accuracy in time which mean in brief the solution to the NSE is split into two steps [86].

In the first part a provisional value for velocity vector u^* is computed on a staggered grid from the momentum equation without the pressure gradient term.

$$\frac{u_i^* - u_i^n}{\Delta t} + A(u_j^n, u_i^*) - \frac{1}{Re}\frac{\partial^2 u_i^n}{\partial x_i^2} = 0 \qquad\qquad 3.14$$

Where

$$A(u_j^n, u_i^*) = u_j^n \frac{\partial u_i^*}{\partial x_j} \qquad\qquad 3.15$$

Here all the terms are known at time (n), and therefore the equation can be solved implicitly using a matrix solver to give the value of u_i^*. In the second step the difference between the velocity solutions across the time step is related back to the pressure gradients.

$$\frac{u^{n+1} - u_i^*}{\Delta t} + \frac{1}{\rho}\frac{\partial P^{n+1}}{\partial x_i} = 0 \qquad\qquad 3.16$$

Since neither the pressure or the velocity is known at the new time step (n+1), taking divergence of both sides gives:

$$\frac{1}{\Delta t}(\frac{\partial u_i^{n+1}}{\partial x_i} + \frac{\partial u_i^*}{\partial x_i}) + \frac{1}{\rho}\frac{\partial^2 P^{n+1}}{\partial x_i^2} = 0 \qquad\qquad 3.17$$

Since u^{n+1} needs to be divergence free in order to satisfy the continuity equation, it will give:

$$\frac{\partial u_i^{n+1}}{\partial x_i} = 0 \tag{3.18}$$

Taking out this term from equation (3.17), gives Poisson equation:

$$\frac{\partial^2 P^{n+1}}{\partial x_i^2} = \frac{\rho}{\Delta t} \frac{\partial u_i^*}{\partial x_i} \tag{3.19}$$

Now pressure can be calculated from this equation at a new time step which then is

used in equation (3.16), to give the value of u^{n+1} [87, 88].

3.3.3 Further Improvement in the Time Marching Solution

The time marching described above can be used as it is for our problem. However

the solution of equation (3.14) requires solving a sparse matrix if the convective and

diffusion terms are approximated using TVD and 2nd order central differences. Such

a solution will consume long computational time and thus equation (3.14) is further

directional split to achieve tri-diagonal matrices that can be solved rapidly by making

the algorithm simpler [89].

The splitting of equation (3.14) is as follows:

$$\frac{u_i^{*,1} - u_i^n}{\Delta t} + A_{TVD}(u_j^n, u_i^n) - A_{1st}(u_j^n, u_i^n) = 0 \tag{3.20}$$

$$\frac{u_i^{*,X} - u_i^{*,1}}{\Delta t} + u^{*,1} \frac{\partial u_i^{*,X}}{\partial x} - \frac{1}{\text{Re}} \frac{\partial^2 u_i^{*,X}}{\partial x^2} = 0 \tag{3.21}$$

$$\frac{u_i^{*,Y} - u_i^{*,X}}{\Delta t} + v^{*,X} \frac{\partial u_i^{*,Y}}{\partial y} - \frac{1}{\text{Re}} \frac{\partial u_i^{*,Y}}{\partial y^2} = 0 \tag{3.22}$$

$$\frac{u_i^{*,Z} - u_i^{*,Y}}{\Delta t} + w^{*,Y} \frac{\partial u_i^{*,Z}}{\partial z} - \frac{1}{\text{Re}} \frac{\partial u_i^{*,Z}}{\partial z^2} = 0 \tag{3.23}$$

Equation (3.20) introduces the second order TVD scheme explicitly and equations (3.21) to (3.23) are directional split. $A_{1st}(u_j^n, u_i^n)$ is $u_j^n \dfrac{\partial u_i^n}{\partial x_j}$ where the derivative of

$\dfrac{\partial u_i^n}{\partial x_j}$ is approximated using a first order upwind derivative. Approximating the

convective derivatives in equation (3.21) to (3.23) by first order upwind scheme will

cancel out the effect of this scheme in equation (3.20) up to order of $O(\Delta t^2)$ [83].

Most importantly it will yield tri-diagonal matrices for equations (3.21) to (3.23)

which can be solved rapidly. The end result $u_i^{*,Z}$ will be then fed into equation

(3.16) and (3.19) as u_i^* to continue the process of the projection method. The

advantage of equations (3.20) to (3.23) over equation (3.14) is the rapid

computational solution. However there are two disadvantages, first the directional

split may introduce artificially preferred directions. To minimize this effect the order

of splitting is routinely changed in the code from (x, y, z) to (y, z, x) to (z, x, y) and

back to (x, y, z) during the time marching. The second disadvantage is that the first

order upwind scheme in equation (3.20) does not completely cancel the first order

upwind scheme effects in equation (3.21) to (3.23). As Δt increases this cancellation

diminishes and more numerical dissipation is introduced in the solution. This effect

will be studied later by varying the value of the numerical safety factor *SF* defined

as:

$$\Delta t = \frac{\min(\dfrac{\Delta x}{u^n}, \dfrac{\Delta y}{v^n}, \dfrac{\Delta z}{w^n})}{SF} \ , \qquad\qquad 3.24$$

where the numerator is the CFL limit for Δt. Since we use an implicit time marching SF can and will be taken smaller than one.

3.4 Accuracy of the Numerical Solution

In this section the accuracy of the numerical solution is investigated. Initially the flow field is solved using two available grid resolutions and the results are discussed. For an appropriate grid resolution the variation in some flow properties are investigated with respect to the time step. Finally some computations are carried out using different convergence criteria and the results are discussed.

3.4.1 Grid Resolution

Accuracy of the numerical solution has been investigated for two grid resolutions of; $(nx = 129, ny = 129, nz = 65)$ and $(nx = 197, ny = 197, nz = 97)$ using both laminar and RANS flow conditions. The nasal resistance has been plotted (Figure 6) for various volume flow rates considering both respiratory phases.

The plot reveals that the laminar code is more dependent on the grid resolution than the RANS calculations. This can be explained as a result of applying the $k - \omega$ RANS model which satisfies the solution quite close to the solid surface without requiring a wall function and hence reducing the mesh size [30, 77]. The difference between the nasal resistance values is greater in the inspiratory phase and increases with an increase in flow rate due to an increase in flow gradient. The result suggests

that for the RANS flow condition, the lower grid resolution can be considered whereas the laminar flow must be calculated using higher grid resolution.
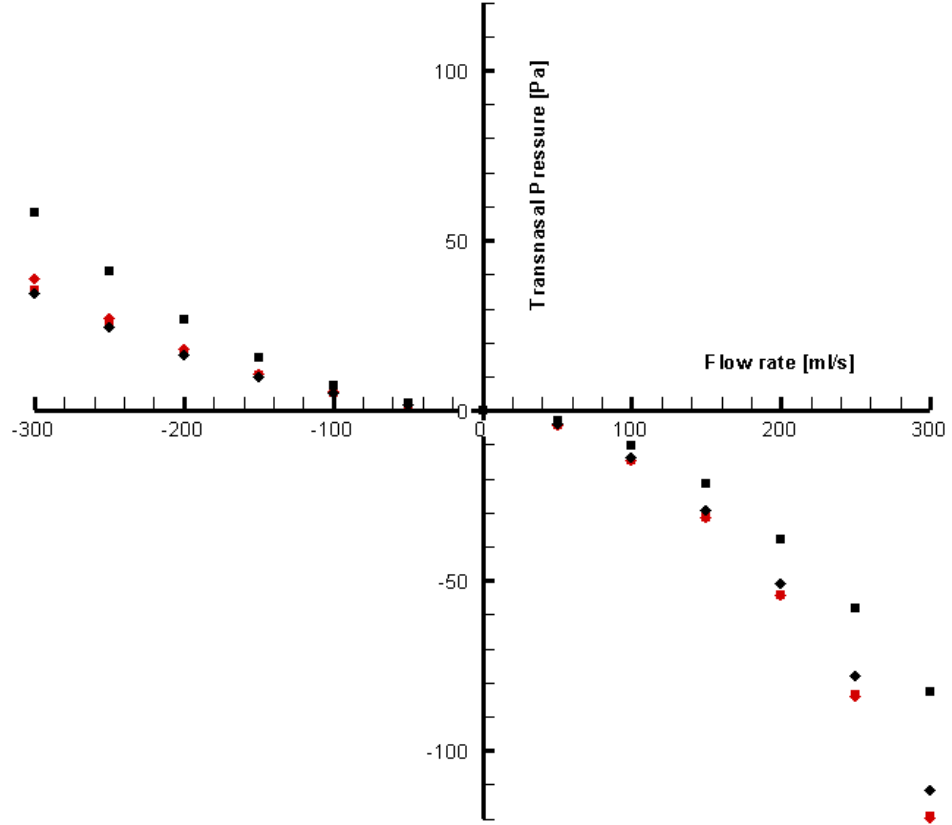
Figure 6: Nasal resistance for laminar (■) and the RANS (◆) calculations using large grid (Red) and small grid (Black) resolutions.

3.4.2 Flow Properties and the Safety Factor Ratio

For the numerical solution an implicit time marching is applied in order to deal efficiently with the strict CFL limit caused by the narrow walls inside the cavity. However taking the time step (Δt) too high, may also lead to inaccurate calculations as a result of obsessive numerical dissipation used to stabilize the solution for a high Δt when trying to march faster than allowed by the physics of the flow.

In this section the effect of Δt on the obtained computational results is investigated for determination of a suitable time step. The Transnasal Pressure (*pd*), defined as the pressure difference between the nasopharynx and the nostril, is plotted against the Safety Factor (*SF*) which is the ratio between the CFL limit and the time step using both laminar and RANS flow conditions. The Negative pressure difference sign indication to the inspiratory phase.
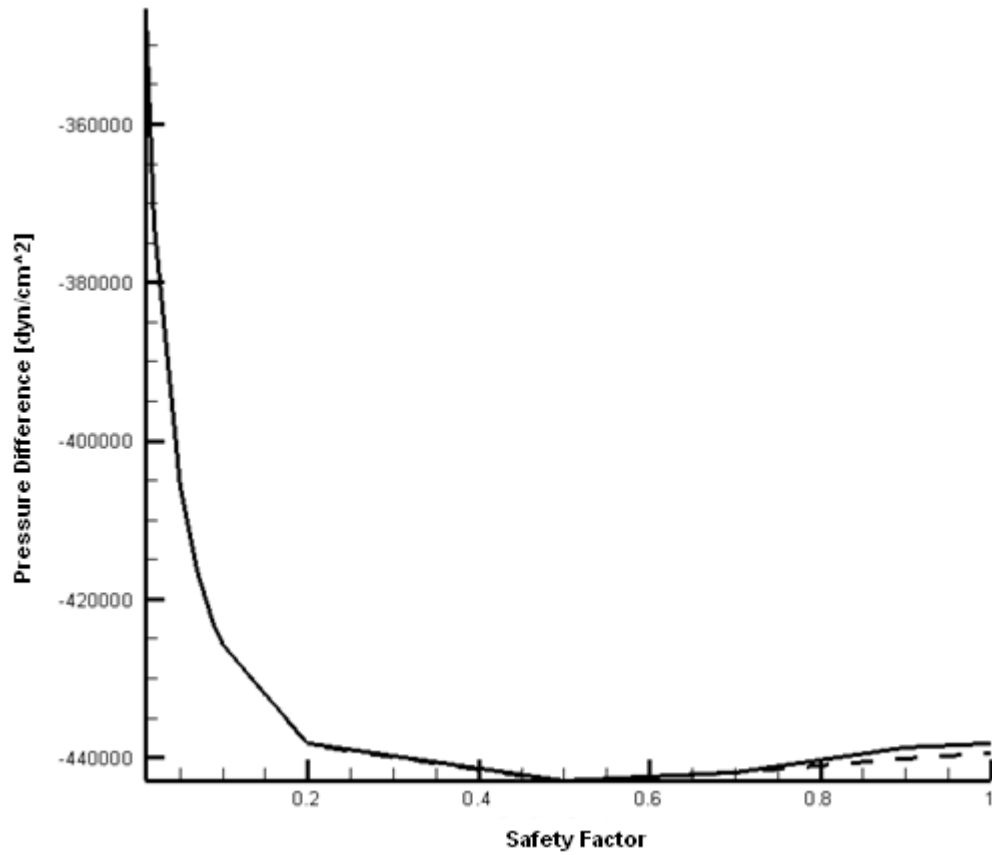
Figure 7: Transnasal Pressure (Pressure difference between the nasopharynx and the nostril) against the Safety Factor (Ratio between the CFL limit and the time step) plot for RANS (Dashed line) and laminar flow (Solid line) conditions at the inspiratory volume flow rate of 200 *ml/s*.
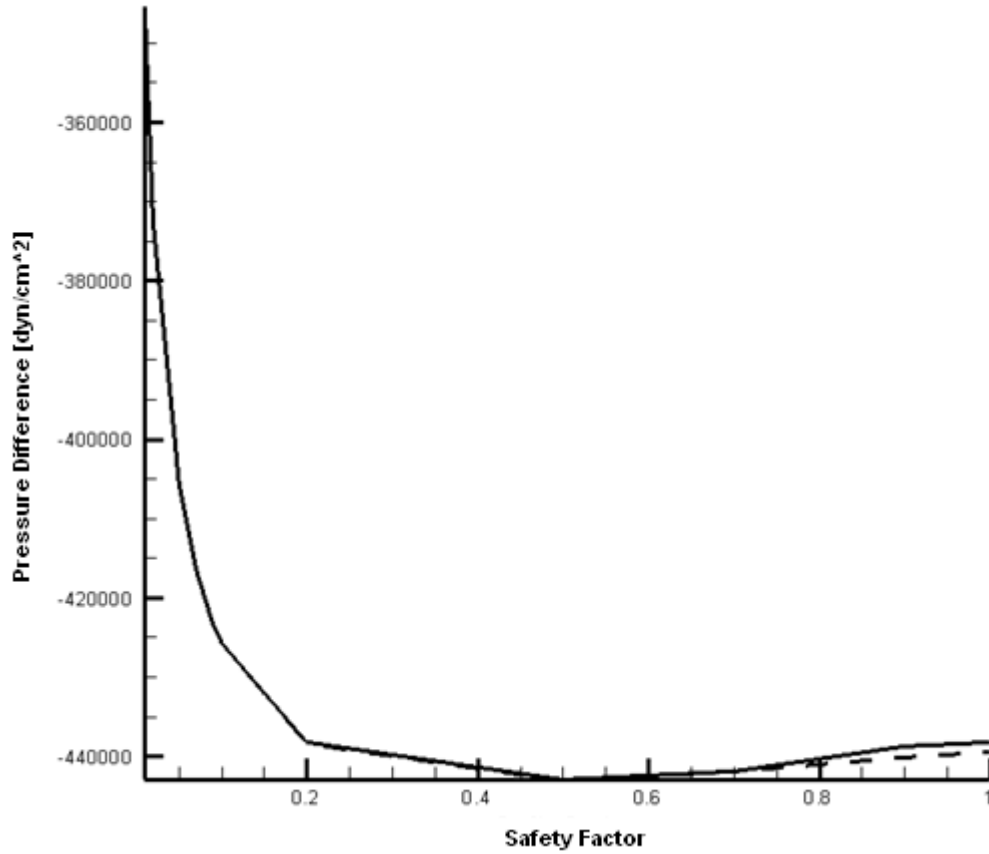
Figure 7 shows that the value of *Pd* increases sharply (ignoring the sign) from *SF* of 0.01 to 0.2 for both RANS and laminar calculations. These rapid changes become more gradual for values of *SF*>0.2. This initial rapid change is due to the numerical dissipation, which has been previously explained, as a result of large time step Δt. As the value of *SF* increases less numerical dissipation is introduced into the solution and hence the value of *Pd* becomes more stable.

Similar behaviour is also observed in Figure 8, where the Peak velocity magnitude and the Peak turbulent kinetic energy are plotted against the *SF* using RANS calculations. Here despite the sharp increase in the peak turbulent kinetic energy, the peak velocity magnitude decreases rapidly up to the *SF* of 0.2. This reduction in velocity can be explained due to the increase in *k* which can remove some of the

energy from the larger scale flow to the smaller scale and hence reducing the mean

flow speed.
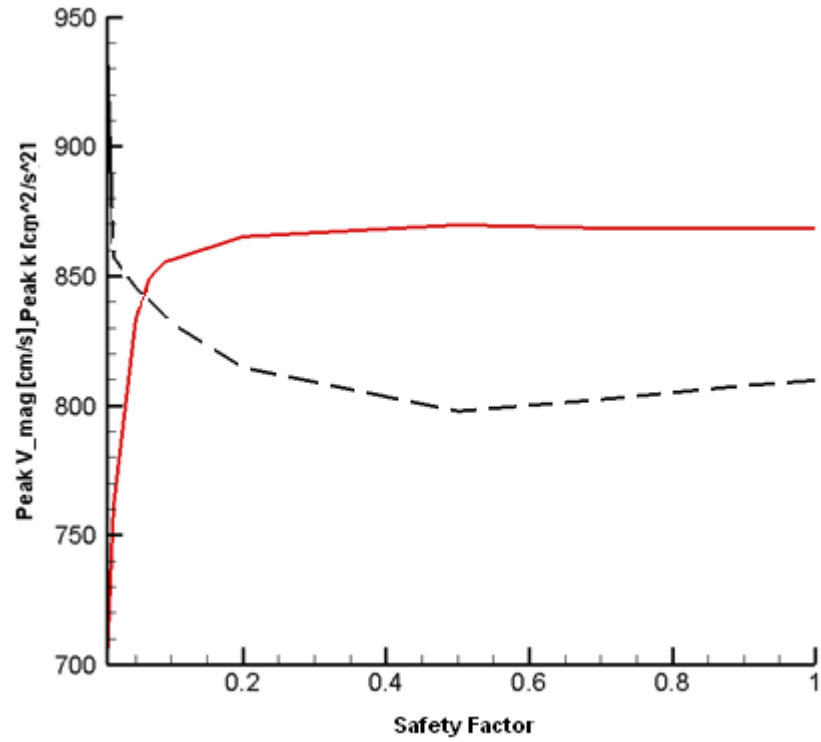
Figure 8: Peak velocity magnitude (Black-dotted) and peak turbulent kinetic energy (Red) for the safety factors of 0.01 to 1 using the RANS code for volume flow rate of 200 *ml/s*.

Figure 9 shows nasal resistance (*NR*) values at two different *SF* of 0.5 and 1. Comparison does not show any significant difference, which allows consideration of *SF* of 0.5 for all calculations.
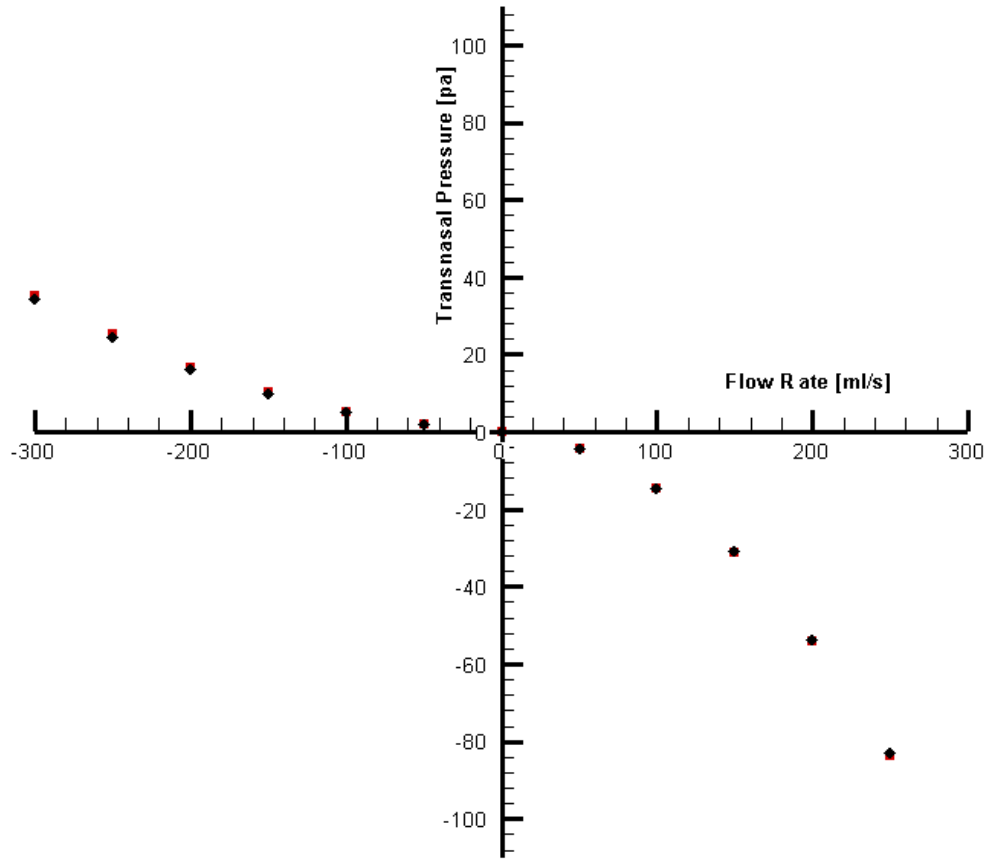
Figure 9: Nasal resistance (Ratio between the Transnasal pressure and the volume flow rate) for safety factor of 0.5 (Black) and 1 (Red) at volume flow rate of 200 *ml/s*.

3.4.3 Convergence Criteria

Two simulations have been carried out for the nasal airflow pattern at the inspiratory flow rate of 200 *ml/s* using convergence criteria (residual) of 10^{-3} and 10^{-5}. The convergence criteria were defined as the L1 norm in the velocity, temperature and humidity variables. Flow properties hold the same values for both criteria as shown in Table 1 and no changes can be observed in velocity magnitude field (Figure 10). This suggest that the residual value of 10^{-3} satisfies the convergence criteria and it is sufficient.

Table 1: Transnasal pressure (*pd*) and velocities at x, y and z directions for the inspiratory flow rate of 200 *ml/s* at two different convergence criteria of 10^{-3} and 10^{-5}.

Residual 10^{-3}	Residual 10^{-5}
$pd = -54.36[Pa]$	$pd = -54.36[Pa]$
$U_x = 5.64 m/s$	$U_x = 5.64 m/s$
$U_y = 7.93 m/s$	$U_y = 7.93 m/s$
$U_w = 3.33 m/s$	$U_w = 3.33 m/s$
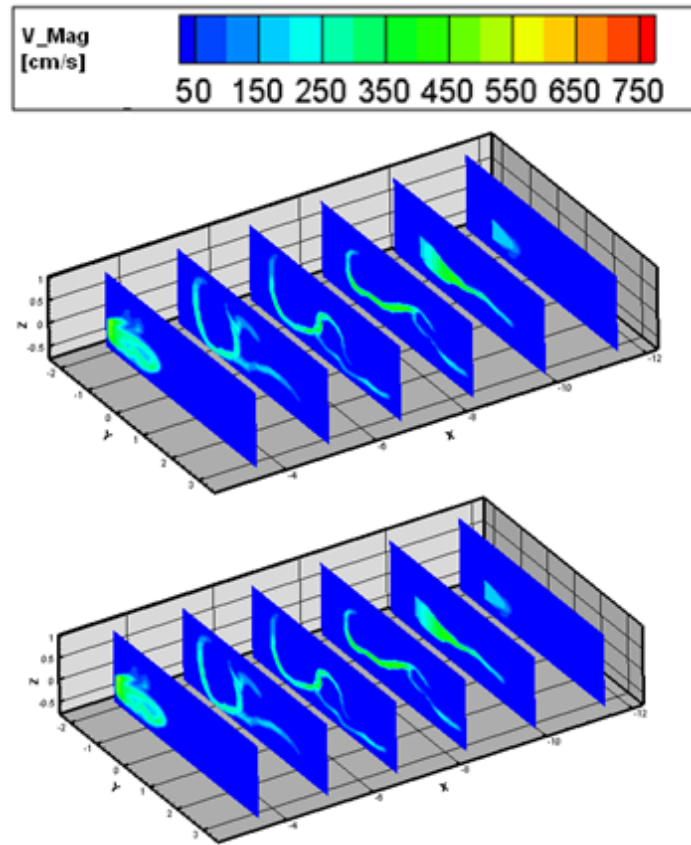
Figure 10: The velocity magnitude contours (V-Mag) for the inspiratory flow rate of 200 *ml/s*, using a convergence criterion of 10^{-3} (Top) and 10^{-5} (Bottom) .

3.5 Parametric Studies

Parametric studies are carried out to validate some of the computational and experimental assumptions used in this study.

3.5.1 Air and Helium Gas & Nasal Airflow Field

In experiments, using the Schlieren optical technique, the helium gas is used to improve the clarity of recorded flow images. The computational nasal airflow is also

simulated using the helium gas at $15°C$ temperature which is the measured laboratory temperature. Properties of helium are calculated as follows:

$$\text{Re} = \frac{\rho.u.l}{\mu} = 8.74 \tag{3.25}$$

$$\text{Re}_t = \frac{\rho.C_p}{k} = 0.59 \frac{J}{cm^2} \tag{3.26}$$

Where helium density, specific capacity, viscosity and the thermal conductivity at $15°C$ are; $\rho_k = 0.169 \times 10^{-3} \frac{gr}{cm^3}$, $C_p = 5.193 \frac{J}{gr.K}$, $\mu = 19.32 \times 10^{-4} \frac{gr}{cm.s}$ and $k = 0.1463 \times 10^{-2} \frac{W}{cm.k}$ respectively. Velocity u (average inlet velocity) and length l (average diameter of the nostril) are taken as 10 $\frac{cm}{s}$ and 10 cm. The nasal flow field suing the helium gas at $15°C$, is compared to the flow fields using the air at two different temperature of $30°C$ and $15°C$ for the respiratory flow rate of 200 ml/s. the results are presented in Table 2 and Table 3.

Table 2: The nasal airflow properties calculated for the helium gas and the air at different temperatures for the inspiratory flow rate of 200 *ml/s*.

q=200 ml/s	Air at $30°C$	Air at $15°C$	Helium at $15°C$
Reynolds number	5.89	6.8	8.74
Peak V_Mag $\dfrac{cm}{s}$	797.72	798.07	798.84
$k_{initial}\ \dfrac{cm^2}{s^2}$	852.28	852.28	852.28
$k_{peak}\ \dfrac{cm^2}{s^2}$	868.54	879.16	924.40

Comparison reveals small changes in flow properties. Both Peak velocity magnitude and the turbulent kinetic energy are shown to increase slightly with an increase in Reynolds number. These changes however are insignificant and show no influence on velocity magnitude fields presented in Figure 11.
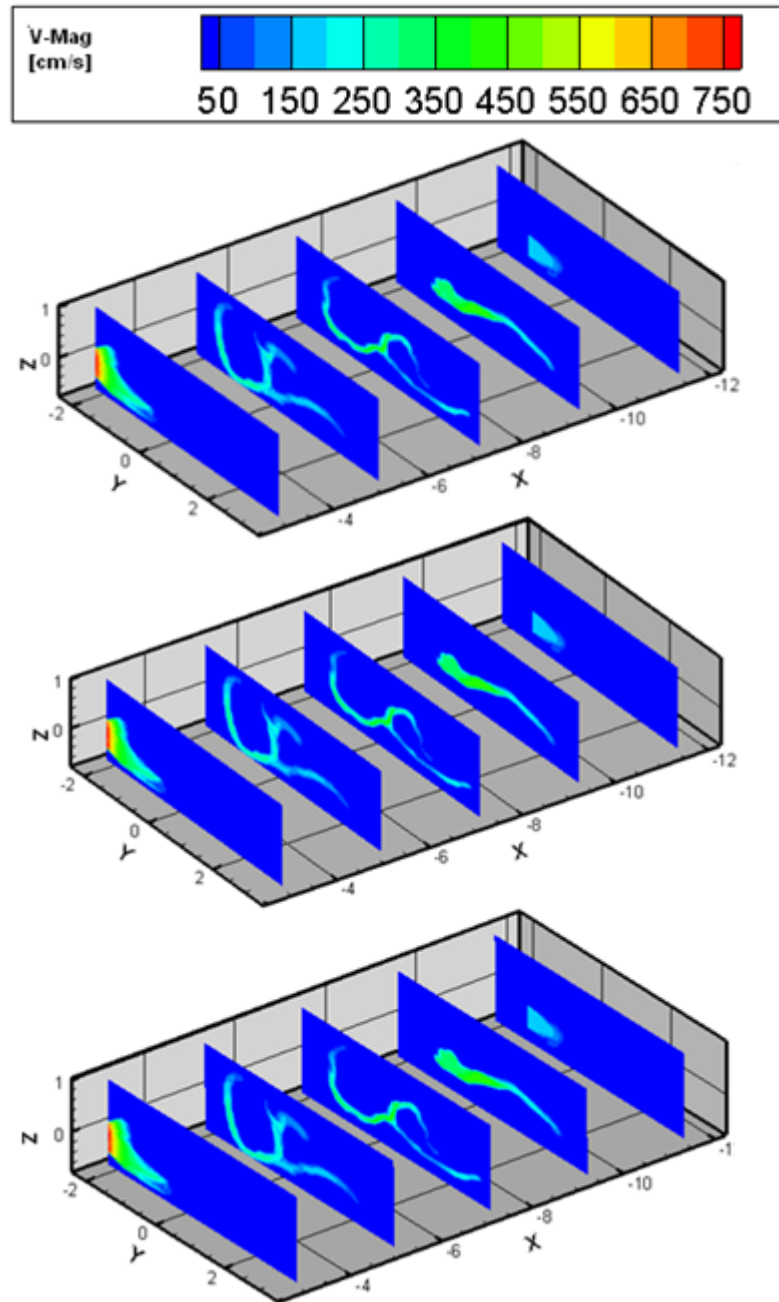
Figure 11: Velocity magnitude contours at the inspiratory volume flow rate of 200 *ml/s*, for helium gas at $15C°$ (Top), air at $30C°$ (Middle) and air at $15C°$ (Bottom).

Table 3: The Nasal airflow properties calculated using the helium gas and the air at different temperatures for the expiratory rate of -200 *ml/s*.

$q = -200\dfrac{ml}{s}$	**Air at** $30°C$	**Air at** $15°C$	**Helium at** $15°C$
Reynolds number	5.89	6.8	8.74
$Vel\_Mag_{peak}\ \dfrac{cm}{s}$	675.61	674.85	673.41
$Vel\_Nor_{peak}\ \dfrac{cm}{s}$	62.50	62.95	64.64
$k_{initial}\ \dfrac{cm^2}{s^2}$	10679.8	10679.8	10679.8
$k_{peak}\ \dfrac{cm^2}{s^2}$	10648	10793	11088

The flow calculations in the expiratory phase reveals a slight reduction in the peak velocity magnitude as the Reynolds number increases while turbulent kinetic energy still continue to increase. In expiratory phase, despite in inspiration where the peak k was higher relative to the initial k value for all three conditions, the k value is only higher for the helium gas and the nasal airflow at $15C°$.
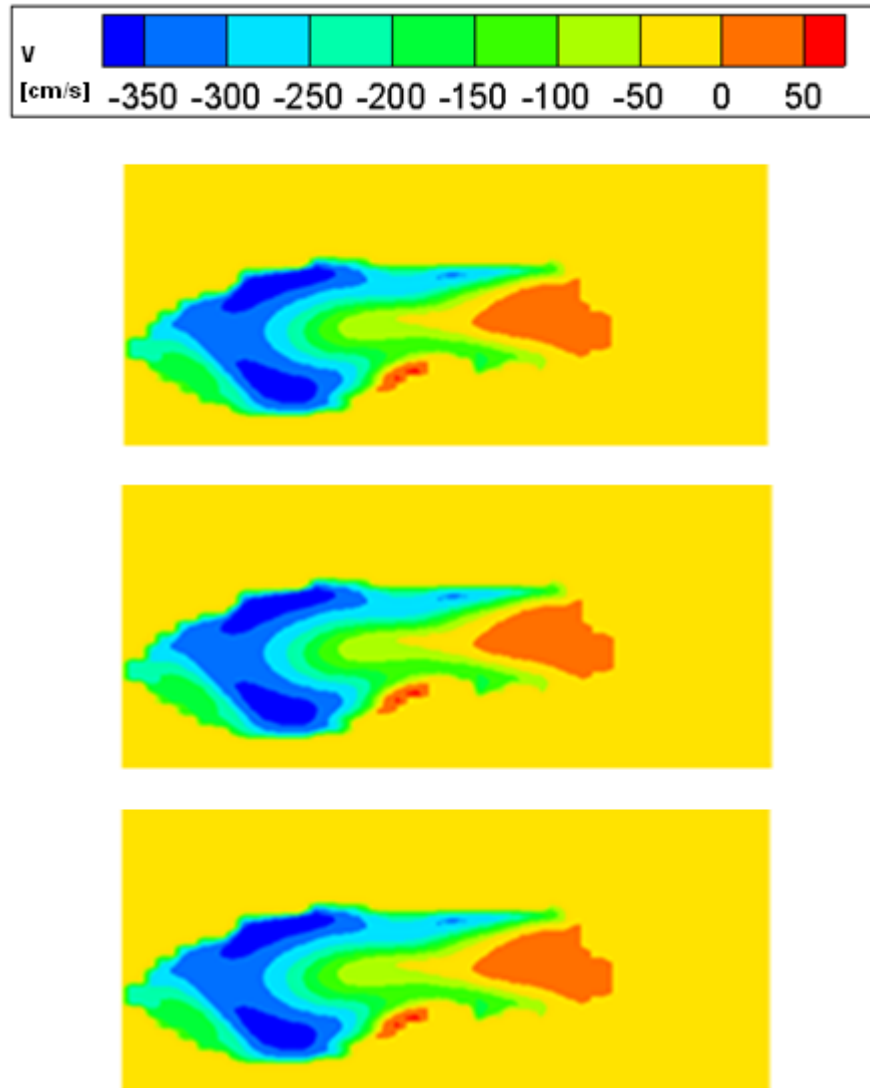
Figure 12: Normal velocity (V) contours at the nostril, for the expiratory flow rate of -200 *ml/s* for the air at $30C^{\circ}$ (Top), helium at $15C^{\circ}$ (Middle) and the air at $15C^{\circ}$ (Bottom).

The normal velocity contours at the nostril, are plotted in Figure 12, at the expiratory flow rate of 200 *ml/s*. The velocity fields are similar despite the small variation in flow properties shown in Table 3. This suggests that the experimental results using the helium gas are valid to give information about the nasal airflow pattern. However judgment on the flow nature and the amount of turbulence should be avoided since the turbulent kinetic energy values were varied.

3.5.2 Air at Different Temperature

Two simulations are carried out using properties of dry air at different temperatures of $15°C$ and $37°C$ for the inspiratory flow rate of 200 *ml/s*. A small reduction in velocity magnitude is observed from 798.06 to 797.75 *cm/s* as the temperature rises, however this small difference is not significant enough to have any influence on the velocity field as shown in Figure 13.
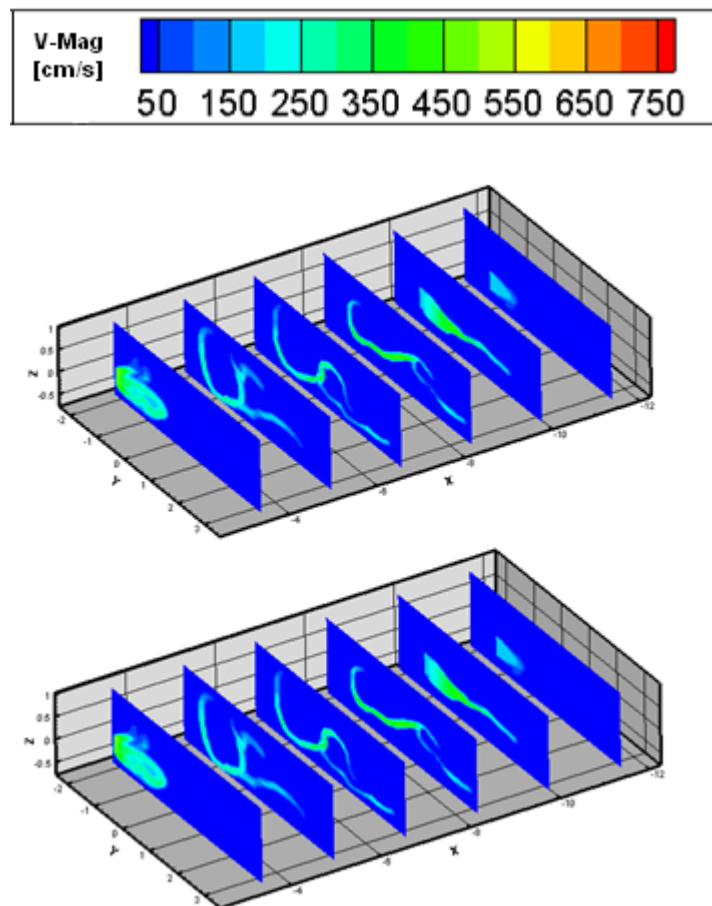
Figure 13: The velocity magnitude field at the inspiratory flow rate of 200 *ml/s* at $15C°$ (Top) and $37C°$ (Bottom).

3.5.3 CO2 & O2 Concentration

The gas mixture varies in respiratory phases (Table 4). In inspiration there is more oxygen and less carbon dioxide than in expiration. Some calculations are carried out to investigate if these changes are followed by a change in air density which needs to be considered in computations.

Table 4: Respiratory Gas mixture.

Gas	Inspired air	Expired air
Nitrogen	78%	78%
Oxygen	21%	16%
Carbon dioxide	0.03%	4%
Argon & noble gases	1%	1%

To calculate the density of air for different gas mixtures, a volume of 1 *liter* of air is considered (≈ 0.4 *liter* is breath in for each inspiration). The air density can be calculated as follows;

$$\rho_{air} = (\rho \times v)_{N2} + (\rho \times v)_{O2} + (\rho \times v)_{CO2} \qquad 3.27$$

The argon and Nobel gases are not considered as the only take 1% of the whole volume and that volume stays the same in both respiratory phases. In inspiration the air density at $0°C$ is calculated as follows:

$$\rho_{air} = (1.25 \times 0.78)_{N2} + (1.429 \times 0.16)_{O2} + (1.97 \times 0.0003)_{CO2} = 1.27 g/l \qquad 3.28$$

And in expiration following the same calculations gives;

$$\rho_{air} = (1.25 \times 0.78)_{N_2} + (1.429 \times 0.16)_{O_2} + (1.97 \times 0.04)_{CO_2} = 1.28 g / l \qquad 3.29$$

Since this difference is not large enough to be considered in computation calculations the air density is taken as a constant in both respiratory phases.

4. Chapter 4

Experimental Procedure

The experiments are carried out on both a human nasal cavity and a scaled (2.54:1) nasal cavity model to validate the computational data.

The Schlieren optical technique is used on a human subject to enable visualization of the nasal airflow field outside the cavity for a steady exhalation. The clarity of the Schlieren images is improved by inhaling and exhaling helium gas which was shown to produce a similar flow pattern to that of air in previous chapter.

A silicon model of the nasal cavity is constructed from the computational model for Particle Image velocimetry measurements. The expiratory flow field is measured at various sections and for different flow rates.

4.1 Particle Image Velocimetry (PIV)

Particle Image velocimetry (PIV) is a powerful optical technique for measuring two or three dimensional instantaneous velocities or other related flow properties over global domain [35]. The fluid is injected with tracer particles which are required to be small in size and with a specific weight close to that of the fluid to ensure, they follow the fluid particles faithfully. It is the tracking of these particles which give information

n about the flow field. The tracer particles are illuminated twice in a rapid succession by means of a pulse sheet laser light. The scattered light by the particles is recorded using a high quality lens and a CCD sensor. Before the CCD sensors both exposures could only be captured on a single frame. As a result there was a directional ambiguity with each recovered velocity vector within the flow field. Nowadays each exposure is isolated on its own frame on a special cross-correlation CCD sensor where its output is stored in the memory of a computer directly in real time [90]. Once the frames are captured the flow velocity can then be calculated by measuring the particles displacement. The most common way of measuring displacements is to divide the plane of the image into small sub regions called the interrogation windows. At each interrogation window the flow is assumed to be uniform. Local displacement of the particles in each interrogation window between the first and the second illumination is then calculated using cross correlation. The cross correlation is used to determine whether the pattern of imaged particles in the interrogation region correspond to a similar pattern in the second image. If similar features are found in both images then the relative spatial displacement can be calculated [34]. Knowing the displacements, the time between the two successive illuminations and the magnification factor, the velocity field can be calculated. This process is repeated for all interrogation spots. The size of each interrogation window should be small enough so that the velocity gradients have no significant influence on the results.

Figure 14 shows a schematic arrangement of an experimental PIV set up in a wind tunnel.
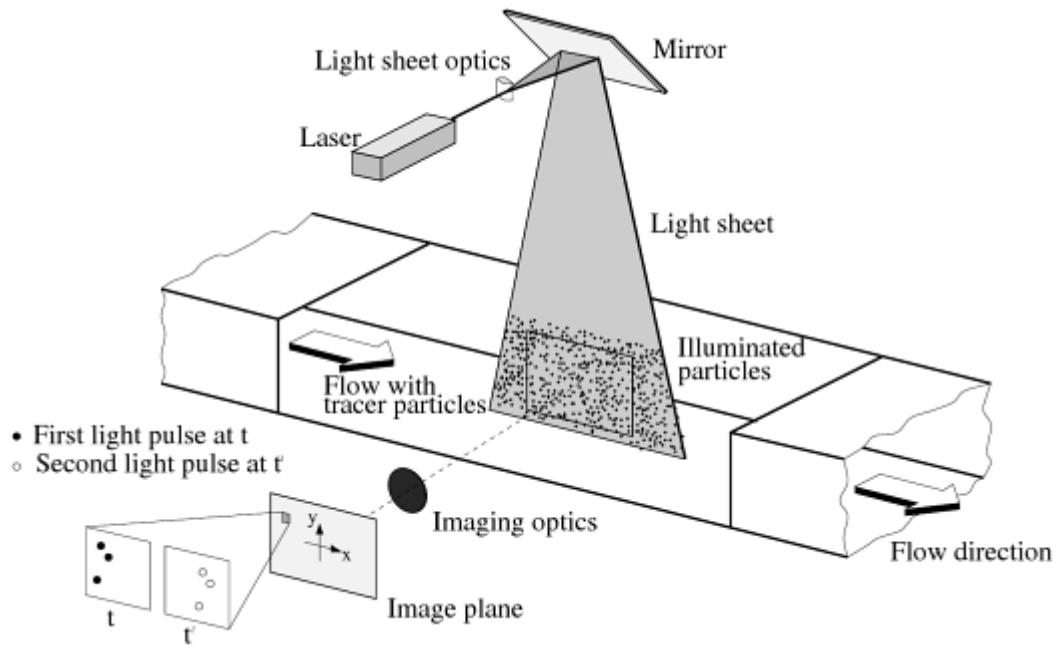
Figure 14: General schematic experimental arrangement for particle image velocimetry in a wind tunnel [91].

4.1.1 Nasal Model

A (2.54:1) model of the nasal cavity is built using Fused Deposition Modeling (FDM) technology from the CAD file of the computational nasal cavity. Since the exact manufacturing process of this model was not available due to the confidentiality, only the general procedure of this technique is outlined.

FDM processing begins by dividing the CAD file into different parts of support structures and extrusion paths by the pre processing Insight software. The model materials in the filament form are supplied to the extrusion nozzle that moves controllably by the computer aided manufacturing (CAD) software package. This extrusion tip is heated to liquefy the thermoplastic model material, ready for extrusion. The model is built layer by layer based on a precise tool path created by

Insight software from the CAD file. The thermoplastic material hardens immediately after extrusion from the nozzle. Final step involves dissolving the supporting structures in a solvable water based material to construct the final complex geometry.

The nasal cavity model was (Figure 15) enclosed in a box to resemble the computational model of the nasal cavity. Since the model was not transparent, only the flow field outside the nostril at exhalation was experimentally investigated.
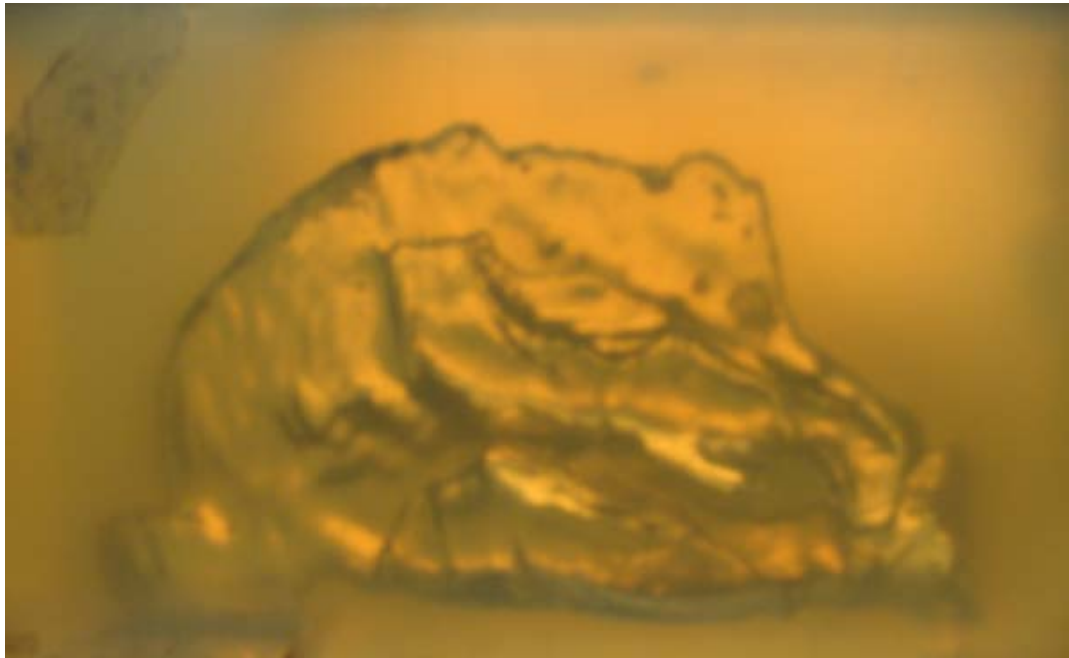
Figure 15: Silicon model (2.54:1) of the nasal cavity built using the FDM technology.

4.1.2 PIV Set up & Procedure

Figure 16 shows a schematic diagram of the PIV apparatus. The PIV experimental set up can be divided into three components of imaging, image capture and analysis and display subsystems. The image subsystem comprises of twin Nd:YAG Lasers (532 nm wavelength, 10-400 mJ/pulse at 10-30 Hz). The lights from the lasers are

combined and directed to the experimental set up via a beam delivery system (Light Arm) and a combination of spherical and cylindrical lenses. The cylindrical lens expands the laser light into a plane and the spherical lens compresses the plane into a thin sheet. The laser head is adjusted so that the laser sheet passes parallel through the model where its thickness is the smallest. The image capture subsystem includes a PIVCAM 13-8 CCD camera which records the scattered light by the tracer particles and a synchronizer. The synchronizer is the timing and the control module for the PIV system which is connected to the computer, camera and the laser and synchronizes their operation. The synchronizer itself is controlled by the Insight software which also analyses and displays the PIV results. Before capturing any image, initially the system is calibrated. After calibration the system uses the calibrating factor to calculate the velocity in *m/s* using the following:

Velocity (*m/s*)= (Pixel displacement $\times$ (mm/pixel) /dt)

After calibration the timing parameters need to be set. Some of the most important of these parameters include; the PIV frame mode (which for the camera to acquire two consecutive single exposure images is need to be set to straddle), laser pulse reputation rate (Hz) and the pulse separation. All these parameters can be varies and set through the Insight software. Pulse separation (*dT*) is the key parameter for matching the PIV system to flow velocity.

  In this experiment the expiratory nasal flow field is measured at three different volume flow rates of 130, 380 and 635 *ml/s* which correspond to 50, 150 and 250 *ml/s* in the computational studies. The pulse separation is found to be different for each of these cases in order to ensure that it is long enough to allow sufficient

displacement between the images of the tracer particles with sufficient resolution and short enough to avoid particles with, out of plane velocity component leaving the light sheet between the subsequent illuminations [90]. The pulse separation values for 130, 380 and 635 *ml/s* are 800, 340, 120 μs respectively. The flow entering the cavity is a mixture of air and olive oil particles. The air flow rate can be adjusted via a flow meter connected to the experimental set up and the density of the oil is controlled using a pressure regulator.
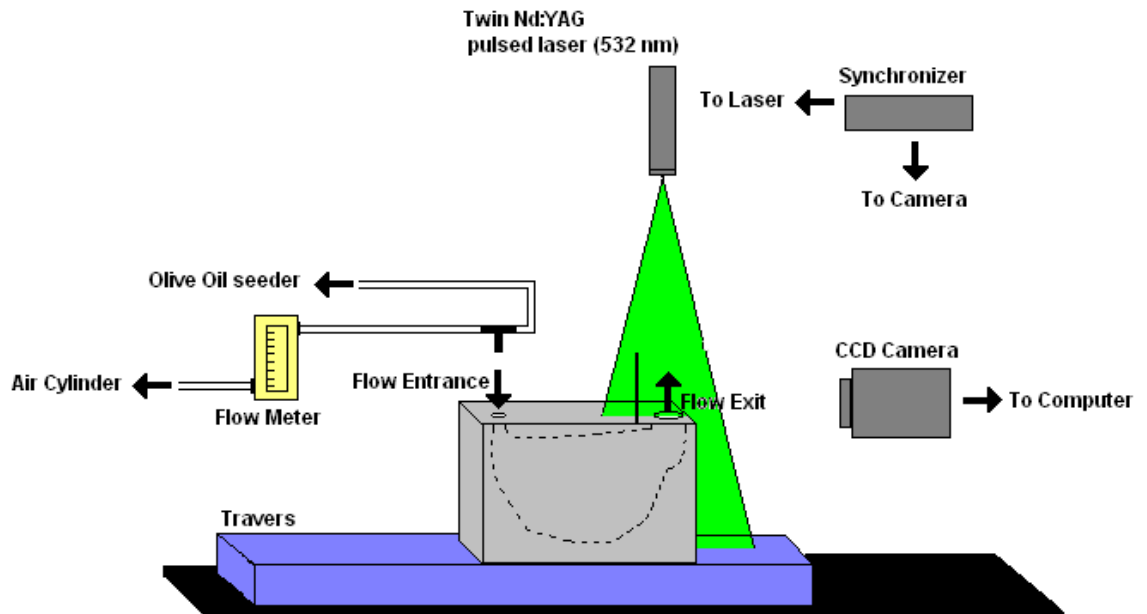
Figure 16: Schematic diagram of the PIV apparatus.
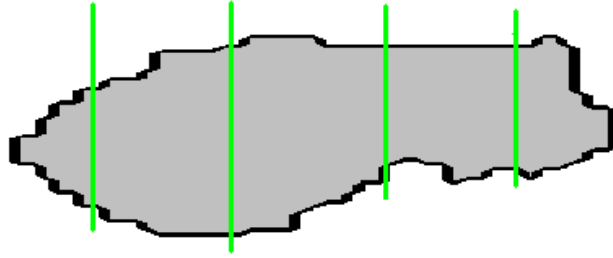
Figure 17: Schematic diagram of four sections for flow measurements.

The nasal flow field is initially measured at four different coronal cross sections in the plane of the flow as shown in Figure 17 for all three volume flow rates. The flow field is also measured at a plane parallel to the nostril (just touching) and on a plane which cuts the nostril medially from one tip to another. For each experiment the nasal cavity model is rotated so that the camera is always located at $90°$ angle to the plane of the laser sheet. This angle ensures that the light scattered by the oil particles are of high intensities. For the spherical oil particles with diameters of greater than the wavelength of the incident light Mie's scattering theory (Figure 18) hold. Although the intensity is greatest at $180°$ degrees but this angle cannot be achieved due to limitations opposed by experimental set up.
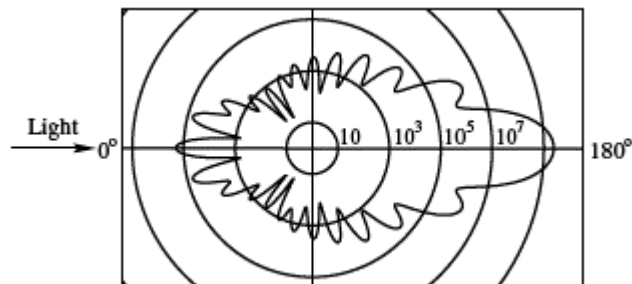
Figure 18: Light ($\lambda = 532nm$) scattering by a 1 μm oil particle in air [90].

The recorded images are saved in the computer and processed using the Insight software. For these experiments processing involves, Image conditioning, grid generation, performing the correlation (cross correlation technique), locating peaks and performing validations. The process data are then analysed using Tecplot software and are compared with computational data for validation at identical planes.

4.2 Schlieren

Some experimental studies are carried out using the Schlieren technique on human subjects inhaling and exhaling helium gas. This technique captures the in-homogeneity in a transparent medium which introduces gradients in the refractive index [92]. These in-homogeneities are called the Schlieren and can be of 1, 2 or 3 dimensions. The Schlieren system however is only capable of portraying 1 or 2 dimensional Schlieren which correspond to gradients of refractive index perpendicular to the direction of the light beam passing through the medium. Light refracts when it reaches the Schlieren with an angle depending on gradient of the refractive index. High angles of refraction results into more clear images of the Schlieren and therefore a less sensitive Schlieren system are required. The refractive index of air and some gases is linearly related to the density as follows:

$$(n-1) = K\rho \qquad\qquad 4.1$$

Where, $(n-1)$ is the refractivity and K is the Gladstone-Dale coefficient which increases slightly as the light wavelength λ increases.

Schlieren can be set up in different arrangements. For these experiment the Z–type Schlieren arrangement is applied (Figure 19) since it is simple to set up and require a small space. This arrangement uses two oppositely tilted concave mirrors, an extended light source, an opaque (knife edge) and a camera or a lens for capturing the images. Using mirror avoids aberrations related to lens type Schlieren such as spherical and chromatic.
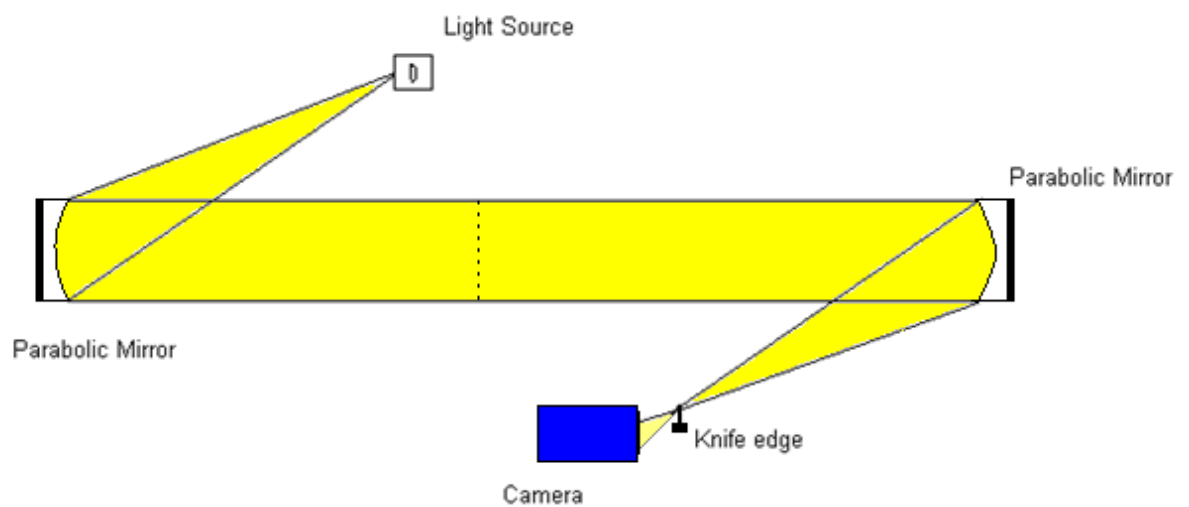
Figure 19: Schematic diagram of the Z-type Schlieren arrangement.

The reflection of the extended light source, (comprises of many elementary point light sources arranged side by side forming a slit) from the first mirror illuminates every point in the test area. The extended light source lends depth of focus (the distance behind the lens where the Schlieren object remains sharply in focus) and produces a composite light source image, which the system would lack in the case of a point light source. This composite light source image at the knife edge plane results into uniform changes of the image as the knife edge is adjusted. This is the fundamental characteristic of a Schlieren image. A parallel beam of light in between

the two mirrors provides the working section. Having a parallel light beam in the test area is essential since it provides the least ambiguous interpretation of the Δa, which is the distance that the refracted light is displaced on the image screen from its original position. Adding the Schlieren in the test area, a bundle of light rays will refract from their original path when reaching this section. Some of these reflected rays will interfere with the knife edge and the rest will pass through the camera producing an image of the particular points within the test area with reduced intensity which is observable compared to the image of the background.

The Z-type Schlieren is accompanied by two optical aberrations known as coma and astigmatism which introduce errors in the faithful production of the light source image in the cut-off plane. Coma occurs when the Schlieren field mirrors are tilted off their optical axis causing the direction of reflected light being dependant on the point of reflection from the mirror. This aberration grows in proportion to the offset angle and thus is minimised by keeping the offset angle small and using long focal length mirrors. Since coma is generated at both mirrors, it is possible to cancel the overall effect by tilting the mirrors by the same angle at opposite direction. An astigmatic system fails to focus a point to a point, and as a result a point light source is imaged as two short lines at right angles to one another. Even at small off set angles and for large f number mirrors some astigmatism is always present. The sensitivity of the Schlieren system depends on the focal length of the second mirror and the un-obstructed height of the light source image [93].

$$S = \frac{f_2}{a} \qquad\qquad\qquad 4.2$$

4.2.1 Schlieren Set up & Procedure

This set up comprises of two identical parabolic mirrors with the focal length of 6 ft, facing each other with the minimum distance of 12 ft (*3.65 meters*) apart. An extended visible light source is used to illuminate the first mirror which collimates the reflected light. This mirror is tilted until the reflected light projects the picture of the first mirror on the entire second mirror. This light is then reflected and produces an image of the light source at the focal length of the second mirror. An opaque which is a razor blade is placed horizontally at the location of the light source image followed by a CCD Panasonic video camera (model WV-F15E). The horizontal razor blade only cuts off the refracted light in the vertical direction and therefore produces an image which only shows the Schlieren in 1 dimension as a result of normal gradients of the refractive index. The camera is connected to a TV screen and a computer via an AD connector which enables recording and editing the images using Adobe premiere software.

The gap between the second mirror and the table (Figure 20) allows the human subject to sit and breathe within the test area. Subjects are asked to tilt their head so that the nasal airflow is perpendicular to the light beam for the best results.

Figure 20: Schlieren experimental set up.

When a disturbance is introduced in the working section perpendicular to the direction of the light beam, reflected light from the first mirror refracts as it passes through the working section. Advancing the position of razor blade to just block a portion of the image of the light source darkens the screen by blocking some of the refracted rays and produces an image of the Schlieren in the screen.

The nasal flow jet is a three dimensional flow and therefore it is not fully characterized by Schlieren which is a two dimensional system. Furthermore this set up uses a horizontal blade which only detects the disturbances in the vertical direction. Despite the one dimensional data, recorded images are still useful for the purpose of this experiment.

The system is also tested for a single and multiple extended light sources in order to find out the optimum set up. Multiple extended light sources are built by placing a grid in front of the light source which is constructed by parallel clear and opaque lines and are proven in literature to increase the field of view and the sensitivity of the system [93]. For this experiment the clarity of the Schlieren images are investigated using different sized of grids. For every grid located at the light soured, its identical grid is used to create a negative copy at the location of the razor blade. A helium tank is placed at the working section with a regulator which allows adjusting the rate of helium jet. Helium gas is used as the Schlieren object since it has a different density from the air. The rate of jet is kept constant for feasibility of comparison when the system is tested for different grids. Comparing the images of Schlieren for the system with and without the grids (Figure 21) shows that the best result is achieved using a single extended light source where no grid is added. This reduced sensitivity can be explained due to the unparallel and dissimilar lines on the grid sheet as a result of poor manufacturing. Furthermore since the negative copy is also cut using the same sheet, the difference between the grid source and the cut off causes the screen to darken or brighten in a non uniform manner. In addition the opaque lines do not completely block the light and allow some lights to pass through them regardless of their position. Finally it is also possible that the grid sheet itself includes some Schlieren which refracts the light from the light source and causes a non parallel light beam through the test area. The images of the Schlieren for a single extended light source and three different grids are presented below.

107
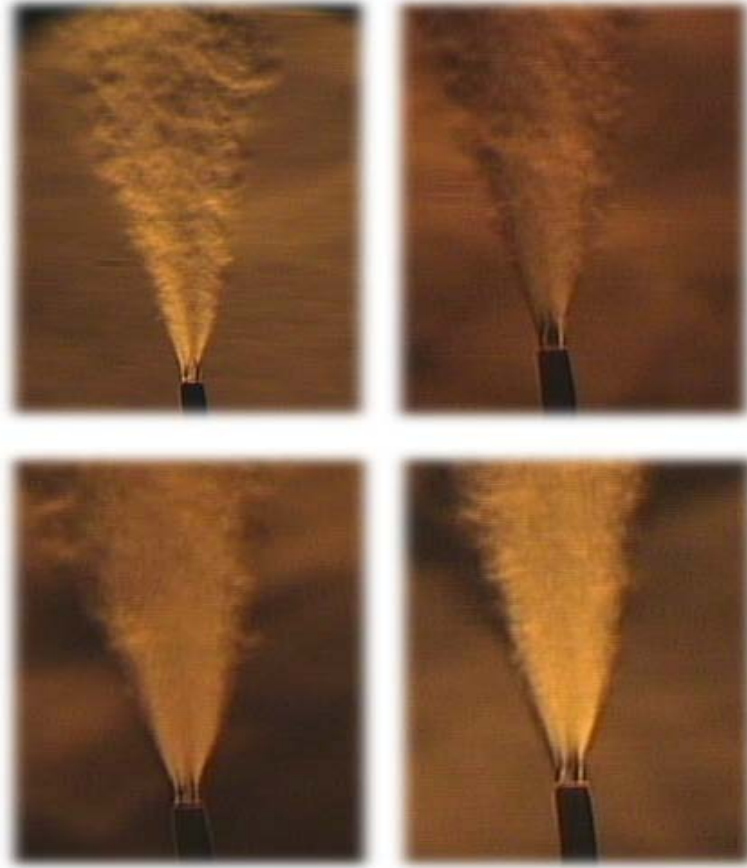
Figure 21: Images of helium gas in the test area using a single extended light source (top left) and different grids of 1, 2 and 3 (top right, bottom left and bottom right respectively).

Since there is no transparent model available, the Schlieren technique is used to capture the image of the nasal airflow outside the cavity on human subject for steady exhale. The subjects in the test area and are asked to blow the air for few seconds at a normal breathing rate. The images captured by the CCD camera are transferred to the computer where the Adobe Premiere software is used for further post processing.

The expiratory flow field is initially captured using 8 human subjects where the images are compared to their subjective nasal patency scores (1 indicating a clear patency and 5 representing a fully obstructed cavity). Next the expiratory flow

outside the cavity is captured for several times using one subject, once blocking one of the cavities intentionally, and once imaging the nasal airflow from both cavities (normal condition). Comparison allows investigating the influence of the adjacent airflows.

5. Chapter 5

Computational Flow Field for the Normal

Nasal Cavity

The CFD FORTRAN 90 codes were run on a local university cluster and Hector, the national computational cluster facilities after implementing thread shearing command of openMP. The results were produced using a computational grid of $(N_X, N_Y, N_Z) = 193,193,97$ points for both laminar and turbulent calculations. The RANS computations were carried out to study the effect of the influx rate on any possible geometry induced turbulence, nasal resistance and the flow pattern. The computational box was then extended to include a portion of the air flow outside of the nostril. The grid was extended to $(N_X, N_Y, N_Z) = (174,173,147)$ due to the increase in the size of the computational domain and various expiratory flow rates were examined. The results for the internal nasal flow computations are discussed next in section 5.1 followed by a discussion on the external airflow field in section 5.2 and a summery in section 5.3.

5.1   Internal Nasal Flow

The internal nasal cavity flow field is investigated by studying the flow velocity magnitude, velocity streamlines, turbulent kinetic energy and the nasal resistance at respiration.

Contours in Figure 22 and Figure 23 represent the velocity magnitudes of the nasal cavity at inspiration and expiration respectively for flow rate of 200 *ml/s* using both laminar and RANS calculations. The volume flow rate of 200 *ml/s* has been suggested in many works as the approximate boundary for triggering turbulence [29]. Similar velocity fields are observed regardless of the computational technique, pointing that at this flow rate most of the flow is laminar. Nevertheless to account for the possibility of turbulence effect the low Reynolds number $K - \omega$ RANS code is used for most of the following computations. The locations of inlet and outlet have been already shown in Figure 5.
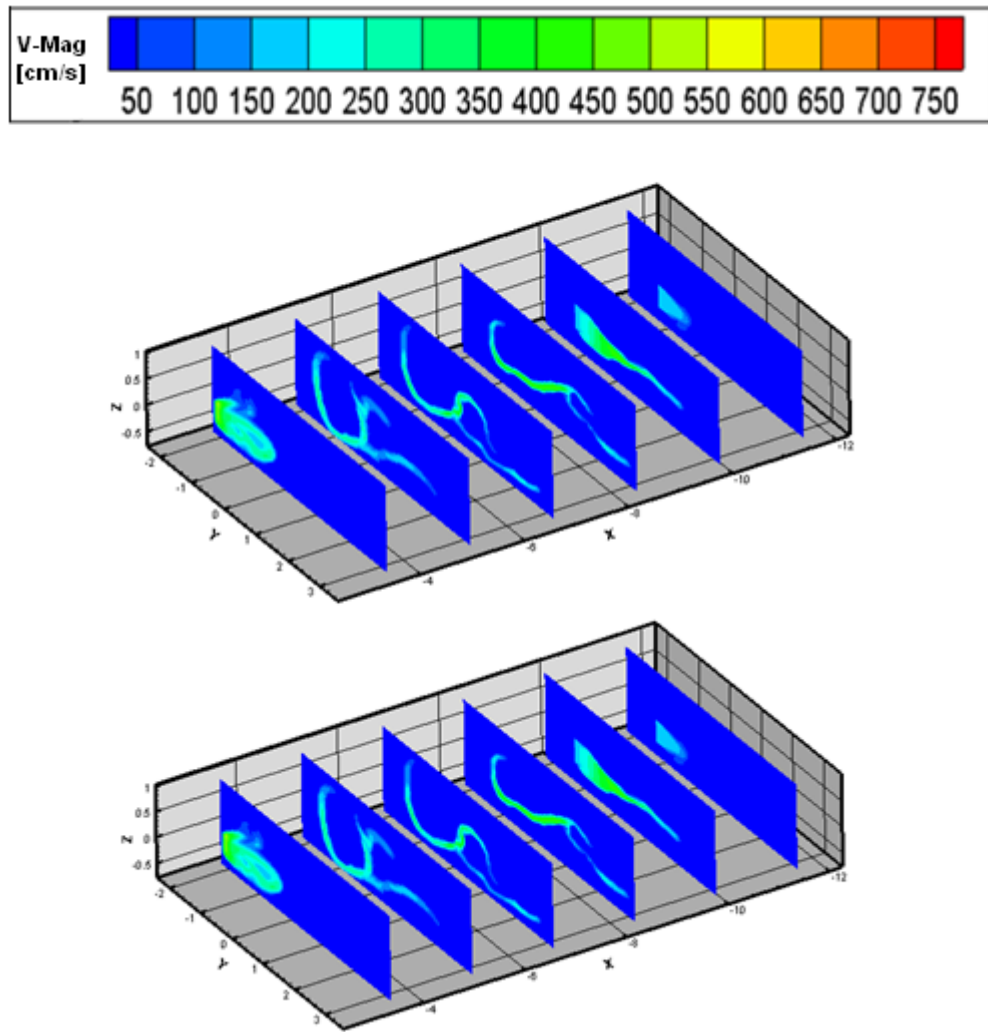
Figure 22: Velocity magnitude (*cm/s*) contours for laminar flow (Top) and RANS (Bottom) at the inspiratory volume flow rate of 200 *ml/s.* For locations of nostril and nasopharynx refer to Figure 5.
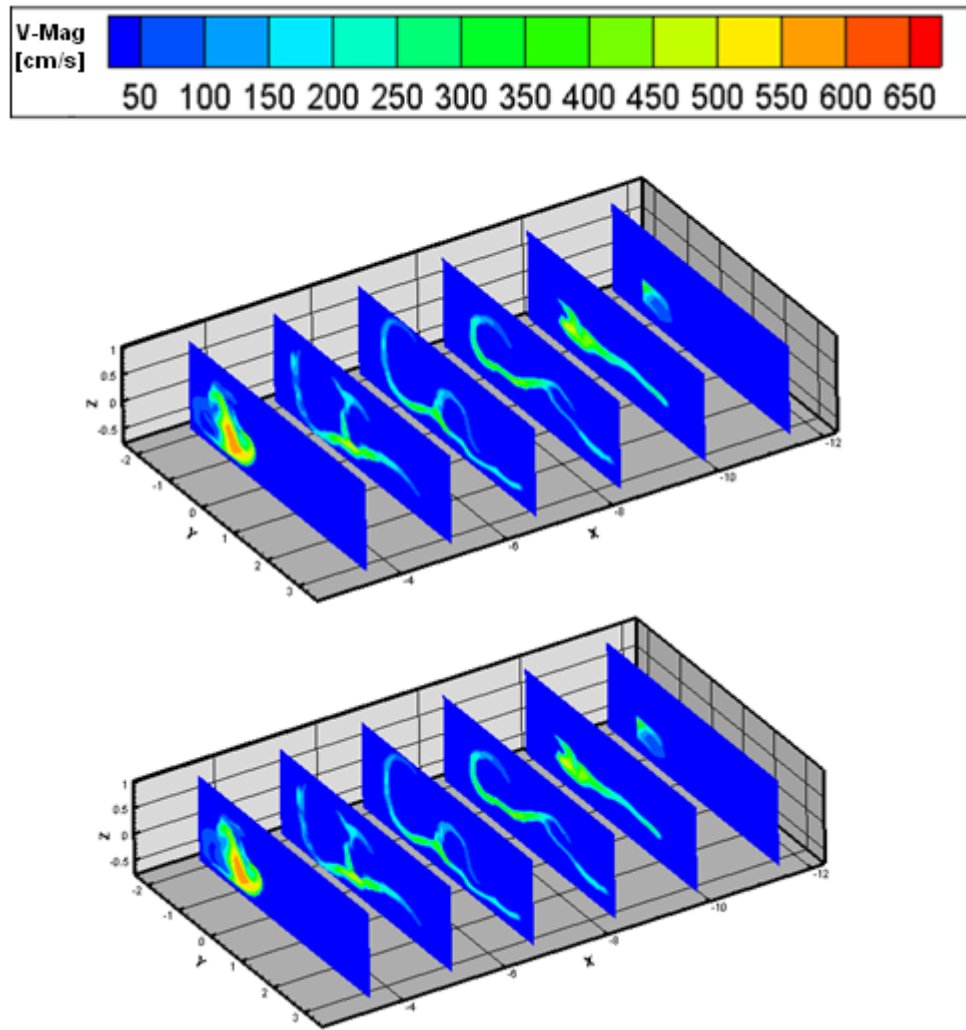
Figure 23: Velocity magnitude (*cm/s*) contours for laminar flow (Top) and RANS (Bottom) at expiratory volume flow rate of q=-200 *ml/s*. For locations of nostril and nasopharynx refer to Figure 5.

5.1.1 Inspiratory Nasal Airflow Field

Figure 24 shows the velocity magnitude contours at inspiratory rates of 100, 150, 200 and 250 *ml/s* respectively from (a) to (d). Highest velocities at the anterior region of the nasal cavity occur around the nasal valve area due to the narrowing of the cross sectional area and mainly in the lower half where the nasal resistance is low. In the turbinated region the highest velocities are along the floor of the lower and middle airways. The velocity magnitude drops towards the meatuses and in the upper half of the nasal cavity. Similar results have been reported in the experimental work of Kelly and the computational studies by Elad and Keyhani [7, 52, 54]. In the posterior region highest velocities are at the nasopharynx region due to the reduction in the cross sectional area. These velocities are also the highest within the entire cavity. Comparison between these contours only reveals an increase in velocity magnitude as the flow rate increases without any changes to the flow pattern itself. This suggests that the pattern of the nasal flow field generally is independent on the flow rate up to 250 *ml/s*, confirming the experimental results by Simmen et al [48].
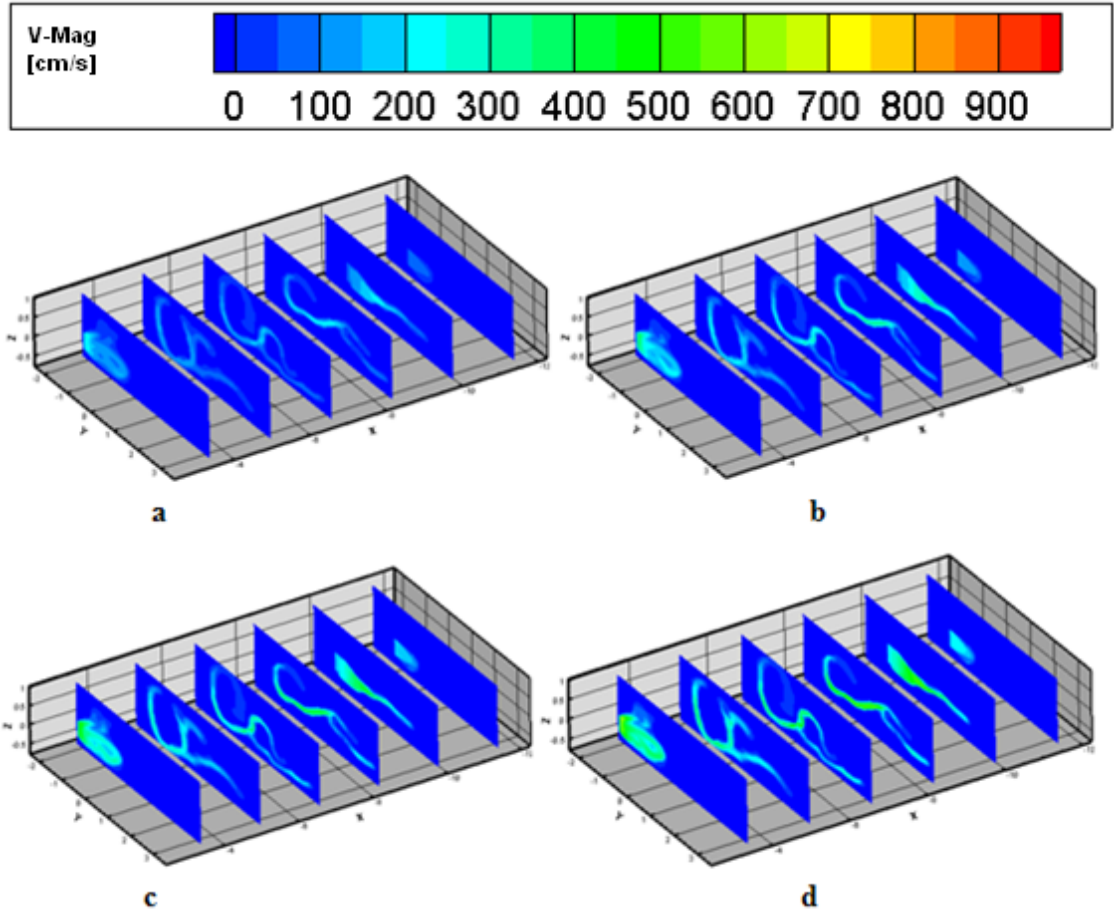
Figure 24: The inspiratory velocity magnitude contours (*cm/s*) within the nasal cavity for flow rates of 100 *ml/s* (a), 150 *ml/s* (b), 200 *ml/s* (c) and 250 *ml/s* (d) using the RANS approach.

A small increase in velocity magnitude in the upper airway at the olfactory region is observed for all inspiratory flow rates. This increase in velocity (shown in Figure 25) is suggested to be part of the mechanism which enhances the olfaction process.
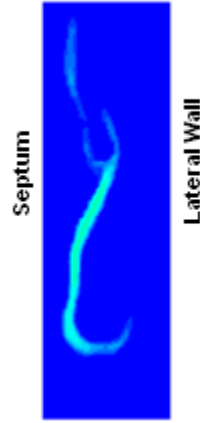
Figure 25: The increase in inspiratory velocity magnitude (X=-8.3 *cm*) at the olfactory (at flow rate of q=150 *ml/s*).
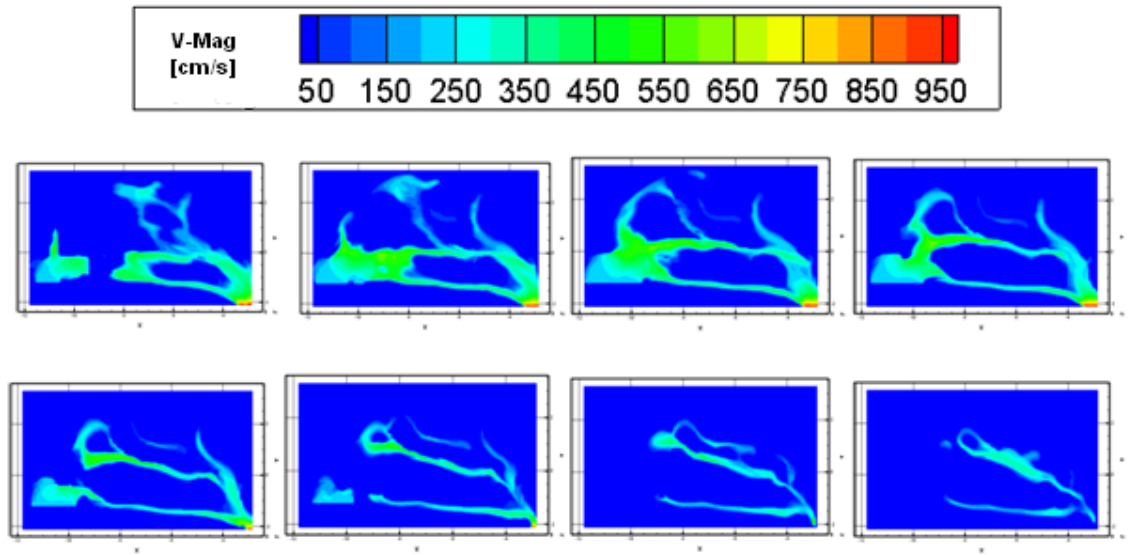
Figure 26: Velocity magnitude contours in sagittal slides on the z-axis; (Top: from left to right, -0.4,-0.3, -0.2, 0.1 *cm*, respectively) and (Bottom: from left to right, 0, 0.1, 0.2, 0.3 *cm* respectively) at the inspiratory rate of 250 *ml/s* showing higher velocities towards the septum.

The velocity contour in the sagittal plane (Figure 26) reveals that the flow velocities are higher towards the septum and decrease towards the lateral wall. This is expected since the air channels are wider towards the septum. Similar behaviour

has also been reported in the computational studies of Sarangapani et al [56]. The location of the septum and the lateral wall on the z-axis is shown in Figure 25.
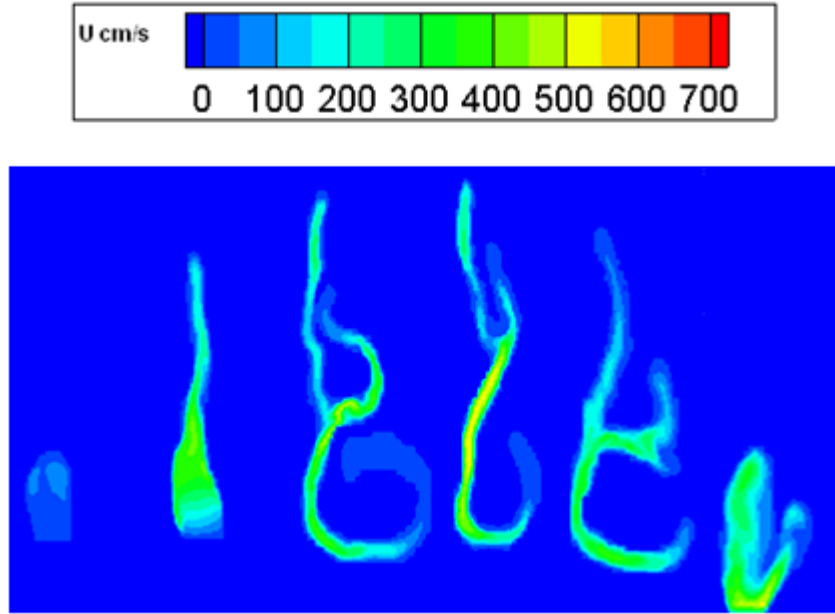
Figure 27: Axial velocities (U *cm/s*) u at x-axis of (-11.5, -.9.9, -8.3, -6.7, -5.1, -3.5) from left to right for q=250 *ml/s* showing higher axial velocities in the lower half of the nasal cavity.

The velocity *U*, *V* and *W* contours (in *X*, *Y* and *Z* directions) are plotted in Figure 27, Figure 28 and Figure 29 respectively for the inspiratory flow rate of 250 *ml/s*. The contour levels of the axial velocity U are adjusted so that they only show positive velocities (no backflow). Highest axial velocity magnitudes are observed in the lower half of the nasal cavity and at the mid section of the turbinated area. At the anterior and the posterior region the axial velocity reduces as the nasal airflow gains speed at other direction. Also comparing all velocity components shows much higher axial velocities within the nasal cavity. This is expected since the nasal cavity's main

purpose is to deliver airflow from the nares to the lower respiratory system which is relative to U.
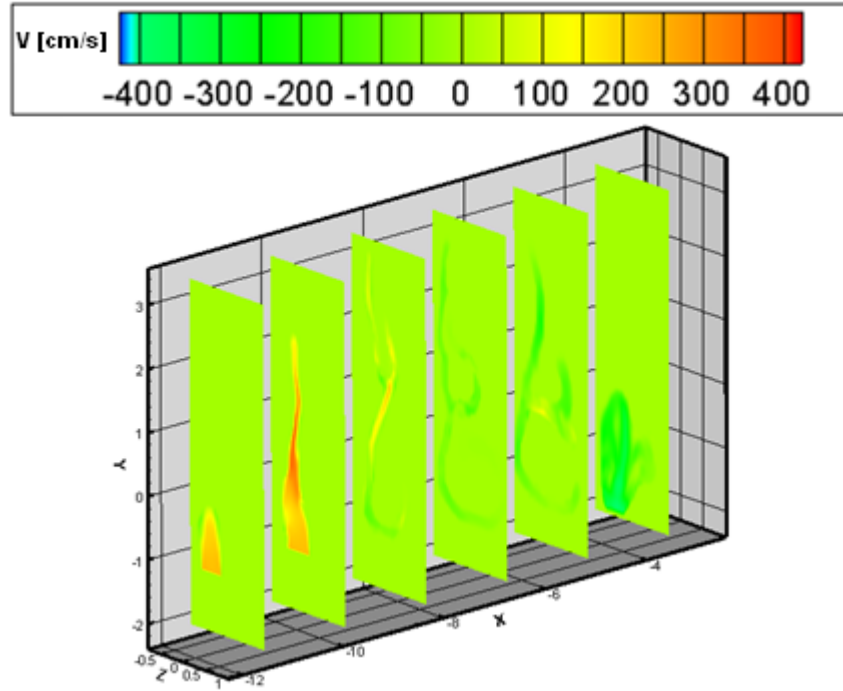
Figure 28: Normal vertical component (V *cm/s*) shown at coronal slides located on the x-axis; -11.5, -.9.9, -8.3, -6.7, -5.1, -3.5 *cm* respectively from left to right for q=250 *ml/s*.

High normal velocity components (*V)* are observed at the anterior region of the nasal cavity. This high velocity combined with the high axial velocity *U*, around the nasal vestibule and nasal valve directs the flow towards the main airway as well as the superior region. In the main airway the normal velocity is small and become almost negligible around the olfactory region. This ensures that the flow which has already reached the olfactory epithelium, spend longer in this region. As the flow is pushed further forwards towards the posterior section of the main airway, normal velocity starts to increase in the opposite direction which directs the flow towards the

nasopharynx. The velocity has its peak magnitude at the nasopharynx which causes a

sharp redirection of flow towards the lower respiratory section.
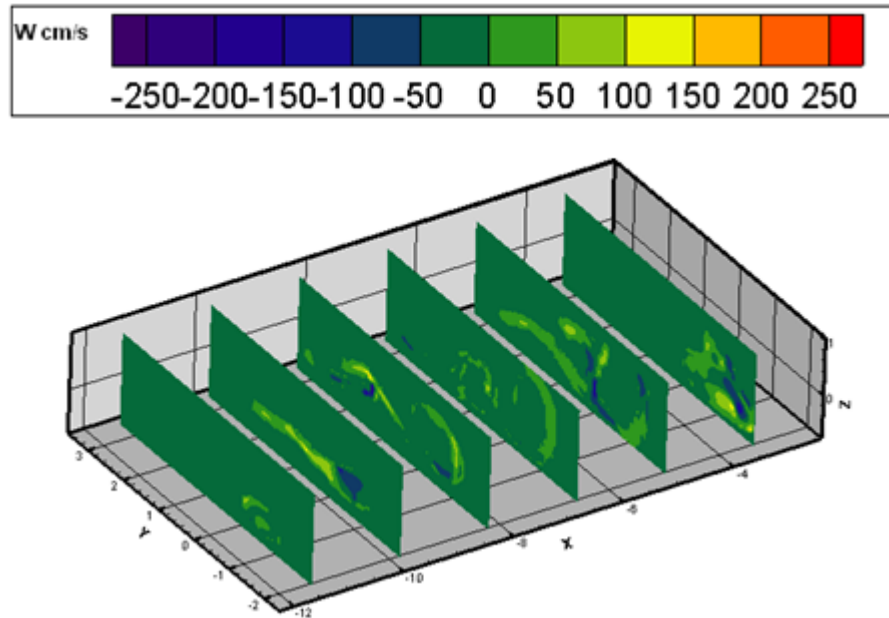
Figure 29: Lateral velocity component W (*cm/s*) in the Z direction, shown at different coronal planes located on the x-axis; -11.5, -.9.9, -8.3, -6.7, -5.1, -3.5 *cm* respectively from left to right (shown at the inspiratory rate of q=250 *ml/s*) showing much smaller lateral velocities compared to other velocity components.

The lateral velocity magnitudes *W* are relatively smaller as compared to other two

components. This can be related to the geometrical dimensions of the nasal cavity

which are longest in the axial direction and shortest in the lateral direction, thus

allowing for the span wise velocity to develop the least. More positive velocities are

also observed, pushing the flow towards the lateral wall from the septum side.

Although the air is directed towards the lateral wall, only a small amount of air is

observed in the meatuses area due to the small magnitude of this component of

velocity. This is expected since the meatuses are to provide drainage for the sinuses.
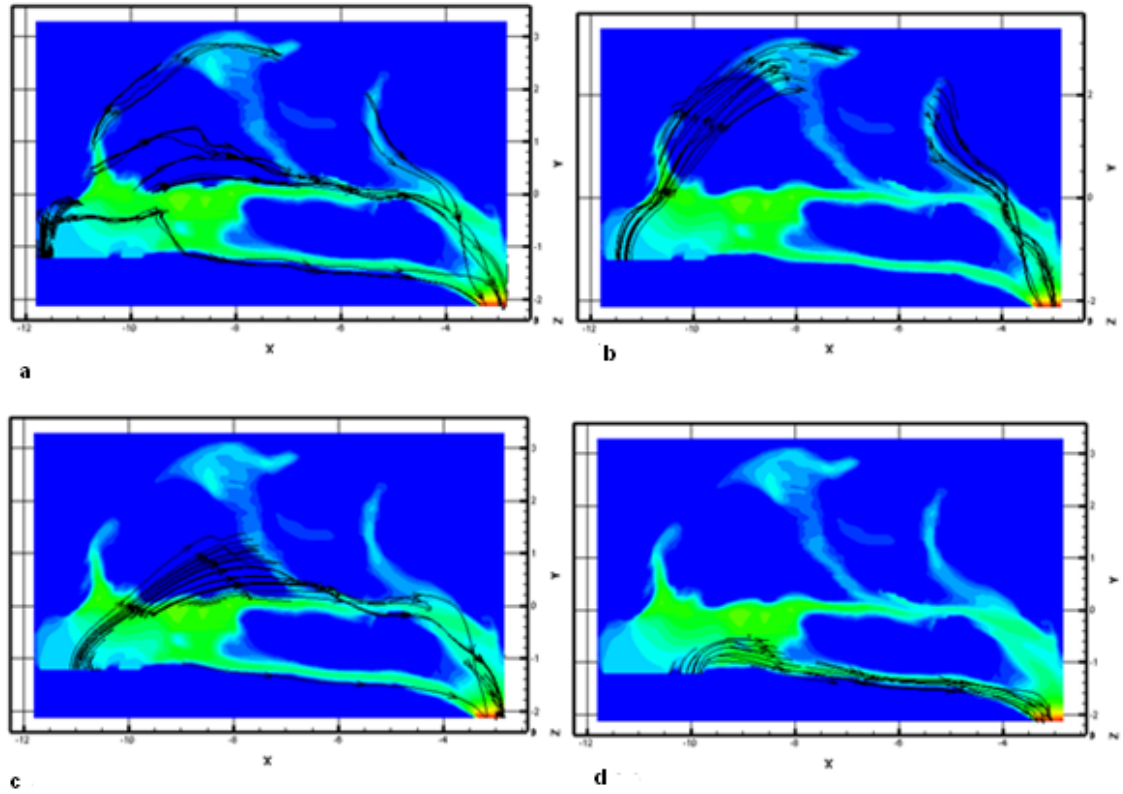
Figure 30: Velocity streamlines entering the nasal cavity, via the anterior section of the nostril which spreads through the entire cavity (a), upper half of the nostril central region which is directed towards the superior region (b), lower half of the nostril central region which passes through the mid section of the main nasal airway (c) and superior section which is directed towards the floor of the nasal cavity (d), at flow rate of q=250 *ml/s*.

Velocity streamlines are plotted at the inspiratory flow rate of 250 *ml/s* to investigate the main flow path and the flow pattern in more details. In Figure 30 the flow stream lines entering the nasal cavity at specific regions are plotted separately. Figure 30-*(a)*, shows the air flow entering the cavity through the tip of the nostril spreads itself throughout the entire airways. Image *(b)* shows that the majority of flow reaching the upper airway is originated from the upper half of the nostril central region, whereas the lower half *(c)* guides the airflow thought the middle airway.

Finally the air coming in via the superior section *(d)* is directed towards the lower airway. Similar flow paths are observed at other flow rates.
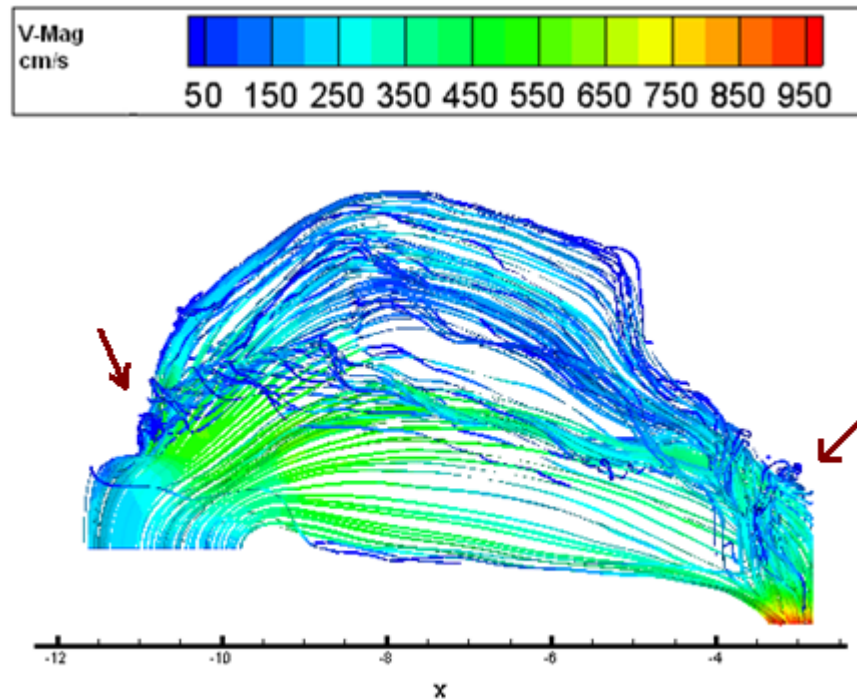
Figure 31: Velocity magnitude streamlines for the inspiratory flow rate of 250 *ml/s* showing two vortices at the anterior and the posterior regions.

Figure 31 shows the streamlines through the entire nasal cavity. Higher velocities are observed at the lower half of the cavity where the flow field is more uniform as compared to the upper half. Two spots of streamlines curling (shown by the red arrow) are observed at the nasal valve (starting as the flow leaves the nasal vestibule) and the nasopharynx. The vortex at the anterior region is mainly the result of sudden expansion of the cross sectional area which exposes the flow to adverse pressure gradient. The anterior vortex gives rise to a swirling flow component throughout the middle airway and to lesser extend through the upper airway which include the

olfactory region. Similar results have reported previously in the computational studies carried out by Weinhold and Leedan [38, 65]. In the nasopharynx the vortex is caused as the flow is exposed to a high degree of directional change, confirming the results from Zhao's computational study [59].
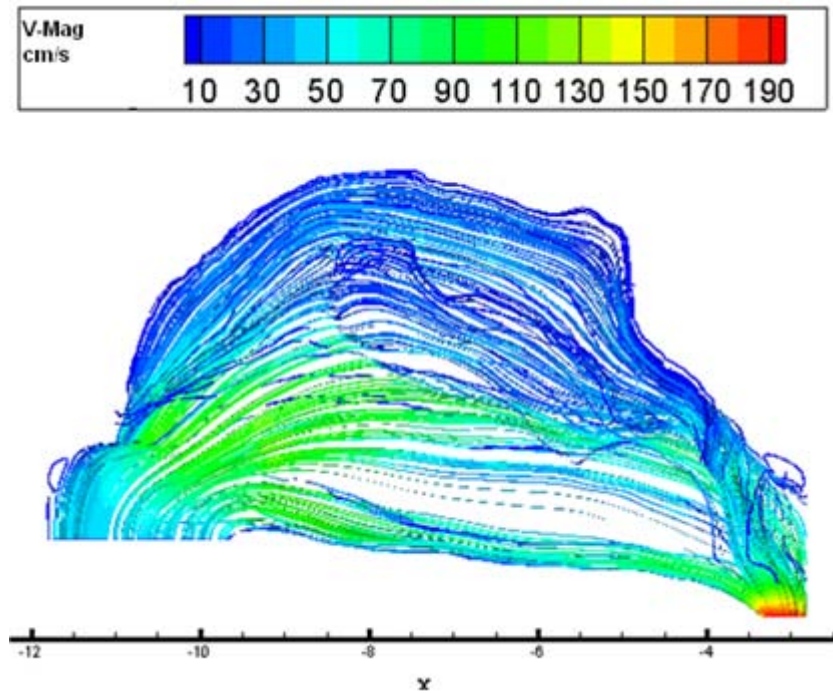
Figure 32: Velocity magnitude streamlines for the inspiratory flow rate of 50 *ml/s*, showing weaker flow vortices.

The velocity streamlines are also plotted for the lower inspiratory flow rate of 50 *ml/s* in Figure 32. The reduction in flow velocity replaces the anterior vortex by a spiralling flow component since the flow has more time to overcome the expansion in the cross sectional area. In the nasopharynx the flow still has strong curls due to the sharp directional change in this region, although the influence of velocity

122

reduction can be observed as the spiralling component is weaker than in the inspiratory phase.

The inspiratory flow calculations reveal that up to 8% of the entire inflow flux passes through the combined lower and the middle meatuses, 25% to 35% through the lower and middle airways and up 15 % of the flow travels through the upper airway and the olfactory region. These fluxes were independent on the inflow flux value. Similar observation has been reposted in other computational investigation of the nasal airflow [52, 54, 59] for the olfactory and inferior regions.

5.1.2 Expiratory Nasal Airflow Field
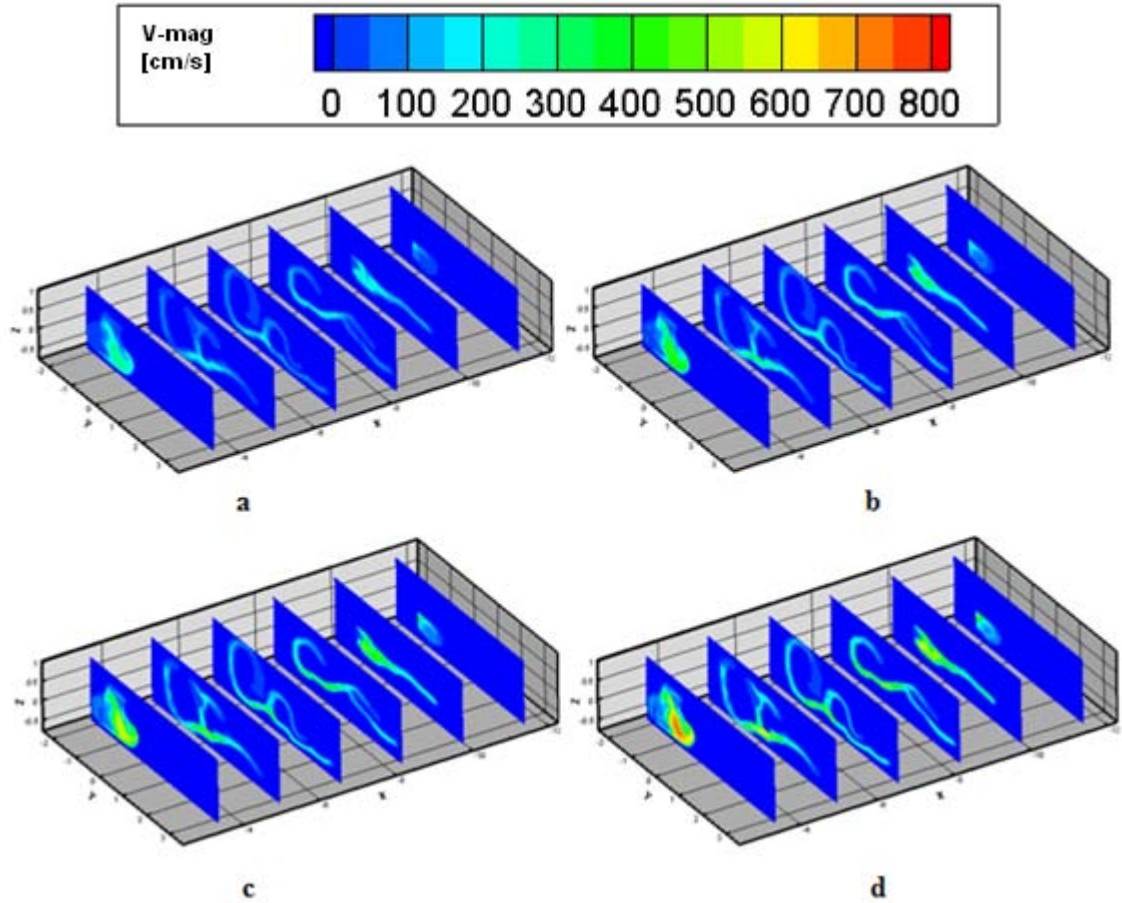
Figure 33: Velocity magnitude (*cm/s*) at expiratory phase for volume flow rates of 100 (a), 150 (b), 200 (c) and 250 (d) *ml/s*, using the RANS approach. For locations of nostril and nasopharynx refer to Figure 5.

Similar to the inspiratory phase, in expiration the flow pattern is also independent of the influx (Figure 33) and decreases from the septum side towards the lateral wall (Figure 34). There is only an increase in velocity magnitude with an increasing flow rate, with no influence on flow pattern. Comparison between the inspiratory and expiratory phases shows more flow in meatuses during expiration, making the flow more uniformly distributed. Similar results have been reported in previous studies

[39, 52, 54] using computational approach. The expiratory peak velocity magnitudes are generally higher than the inspiratory peak velocities apart from the two region of nasopharynx and a section starting from the nasal valve, extended to the anterior region of the main nasal airway as shown in (Figure 35). This is similar to the peak respiratory velocity plot reported in the computational work by Tan et al. [71].
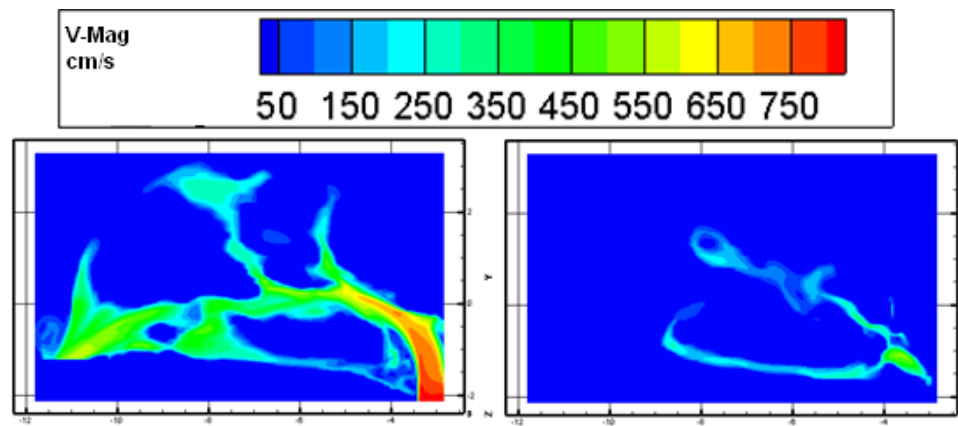
Figure 34: Velocity magnitude (cm/s) contours in sagittal slides on the z-axis; -0.35 and 0.35 *cm* from left to right for q=-250 *ml/s* showing higher velocities near the septum.
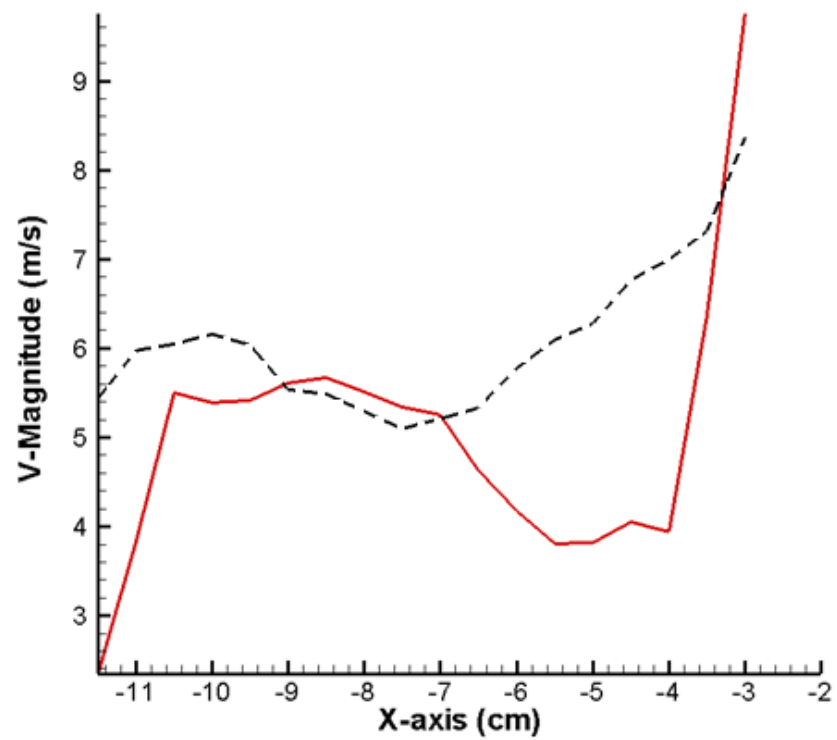
Figure 35: Peak velocity magnitude on the X-axis for inspiration (Red) and expiration (Black- dotted) at flow rate of 250 *ml/s*, showing higher expiratory peak velocities apart from the two regions within nasal valve and the nasopharynx where the inspiratory peak velocity magnitudes are higher.

126
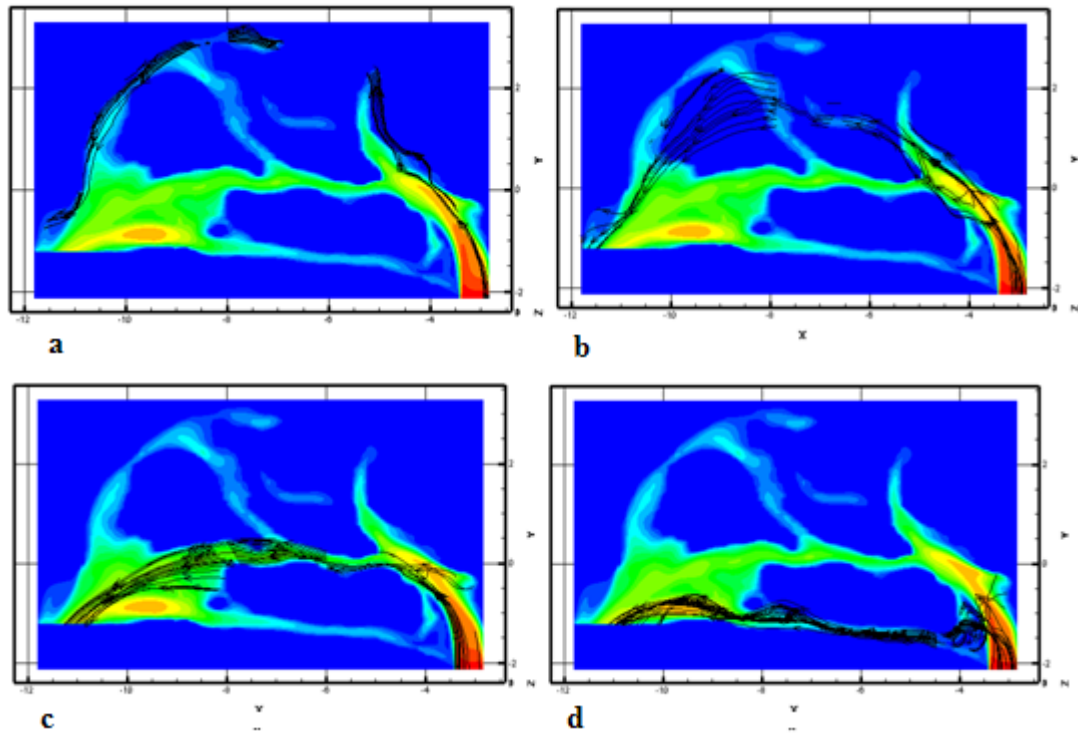
Figure 36: Velocity streamlines entering the nasal cavity via the nasopharynx passing through the (a), upper airway (b), middle airway and meatuses region (c) floor of the middle airway and the lower airway (d) floor of the lower airway at flow rate of q=-250 *ml/s*.

Velocity streamlines are plotted at different airways separately to see whether they originate at a particular area at the nasopharynx. Figure 36 shows that the flow through the upper half of the nasal cavity enters the cavity from the posterior region of the nasopharynx and the air flow through the lower half starts from the anterior region. However image *(d)*, shows the flow through the floor of the lower inferior airway is from almost the entire nasopharynx.

The velocity streamlines through the entire cavity (Figure 37) show higher values in the lower half of the nasal cavity similar to inspiration. There are also two vortices at the nasopharynx and the nasal vestibule which are indicated by red arrows. Comparison to the inspiratory phase shows that the expiratory vortices are much

closer to the floor of the nasal cavity. Considering the location, it can be said that the anterior vortex is due to the nozzle effect caused as the flow merges from a higher cross sectional area to a narrower region in addition to the directional change. The posterior vortex however is due to the steep directional change in this section as well as the expansion in the cross sectional area.
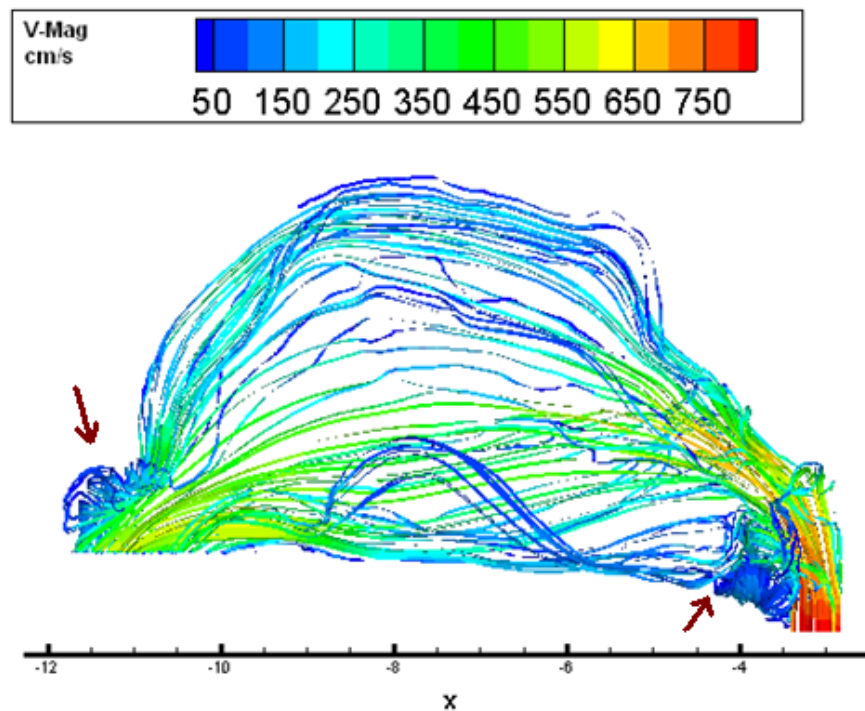
Figure 37: Velocity magnitude streamlines for the expiratory flow rate of -250 *ml/s* showing more uniform flow pattern in this phase and two flow vortices at the anterior and the posterior regions.

Further comparison between the respiratory phases shows that the inspiratory phase is less uniform due to an increased spiralling component in the main nasal airway as compared to the expiratory flow. This maintains the airflow for a longer period in the main turbinated region and hence enhances the conditioning and olfaction. The

increase in flow spiral motion with an increase in the flow rate also explains how a deeper inhalation aids the sense of smell.
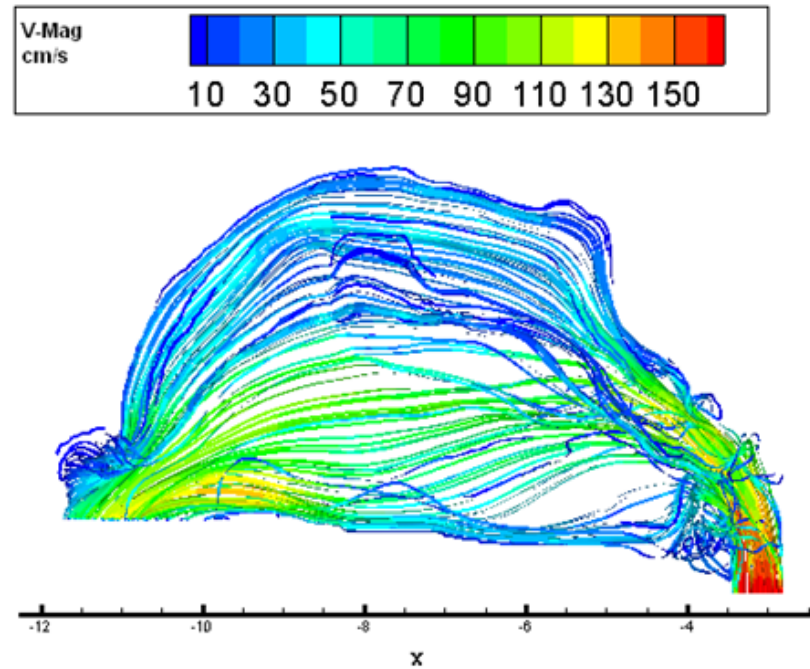
Figure 38: Velocity magnitude streamlines for the expiratory flow rate of -50 *ml/s* showing smaller reduction in flow vortices as compared to the inspiratory phase at a lower flow rate.

The velocity streamlines at the lower expiratory flow rate of 50 *ml/s* are shown in Figure 38. Despite the inspiratory phase, the flow curls are only slightly weaker than those for higher flow rate. This can be explained due to higher cross flow component from the septum side towards the meatuses in the expiratory phase which contributes to a natural clockwise curl. This explains higher flows in the meatuses in the expiratory phase.
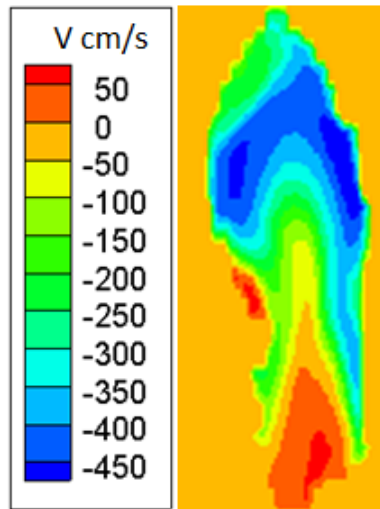
Figure 39: The normal velocity magnitude in *cm/s* at the nostril for the expiratory flow rate of 250 *ml/s*.

The normal velocity contour at the nostril is shown for the flow rate of -250 *ml/s* in Figure 39. The normal velocity is in its peak prior to the tip of the nostril. Two regions on the nostril, one located at the lower part and one at the corner show positive flow velocities i.e. reverse flow. This is due to the expiratory vortex in the anterior region.

5.1.3 Turbulent Kinetic Energy

In the RANS calculations, an initial value of turbulent kinetic energy k is defined at the nostril in inspiration and at the nasopharynx in expiration. If the flow becomes turbulent there will be an increase in k from the inlet value defined at these two regions, due to an increase in turbulent fluctuations. In the case of laminar flow, it is expected that this initial value of k to diminish as the flow develops into the nasal cavity.

5.1.3.1 Inspiratory Turbulent Kinetic Energy

For an inspiratory flow rate of 300 *ml/s* the contours of turbulent kinetic energy are shown in Figure 40. The contours show the expansion of *k* up to the anterior region of the turbinated area. The same behaviour is also observed for all other inspiratory flow rates. However there is only an increase in turbulent kinetic energy from the influx values of 200 *ml/s* and higher.
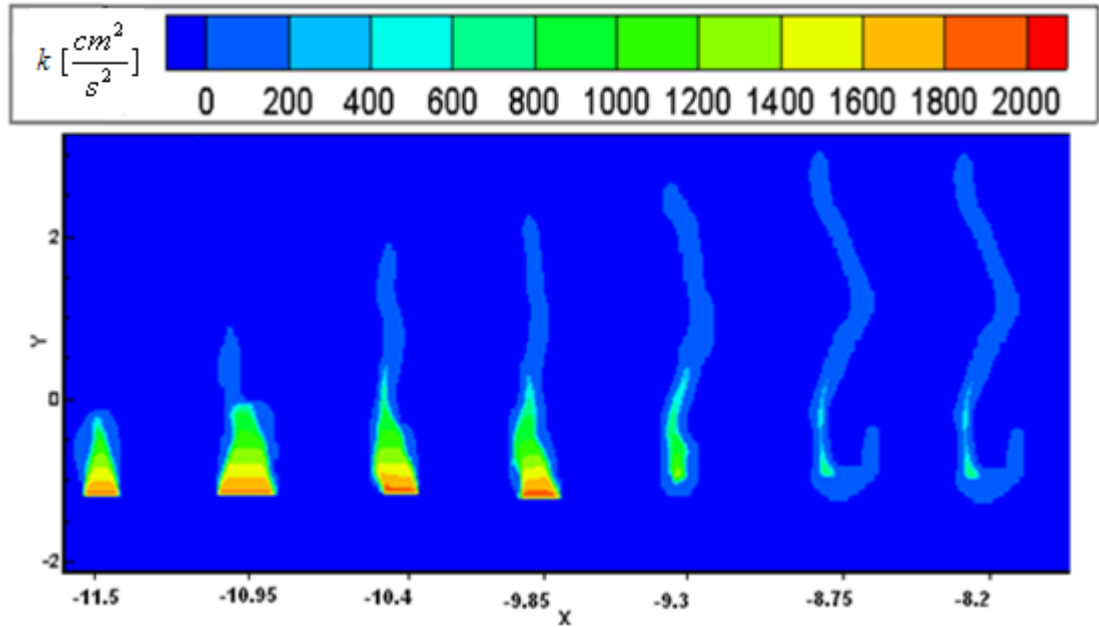
Figure 40: The extension of turbulent kinetic energy k $[\frac{cm^2}{s^2}]$ for the inspiratory flow rate of q=300 *ml/s* along the coronal planes located on the X-axis (-11.5, -10.95, -10.4, -9.85, -9.3, -8.75, -8.2 *cm*) from left to right, starting at the nasopharynx up to the main turbinated region.

Figure 41 shows the turbulent kinetic energy along the nasal cavity (X-axis) at different heights (Y-axis). Just after the nostril (*Y=-1.2*), *k* has its peak value at the tip of the nostril influenced by the initial value. It then decreases with some weak oscillations as the flow continues. Further away from the nostril but still close (*Y=-1.16*), the turbulent kinetic

energy profile is quite different. After a decrease in the *k* value at the tip of the nostril, turbulent kinetic energy raises again at two small regions both located at the nasal valve area. At these two regions the value of *k* reaches to a value higher than the inlet *k* value. The same behavior is still observed for the next slide (*Y=-1.06*) which is still located close the floor of the nasal cavity. As the distance from the nostril increase the *k* profile varies and the peak points on the graph are no longer observed.
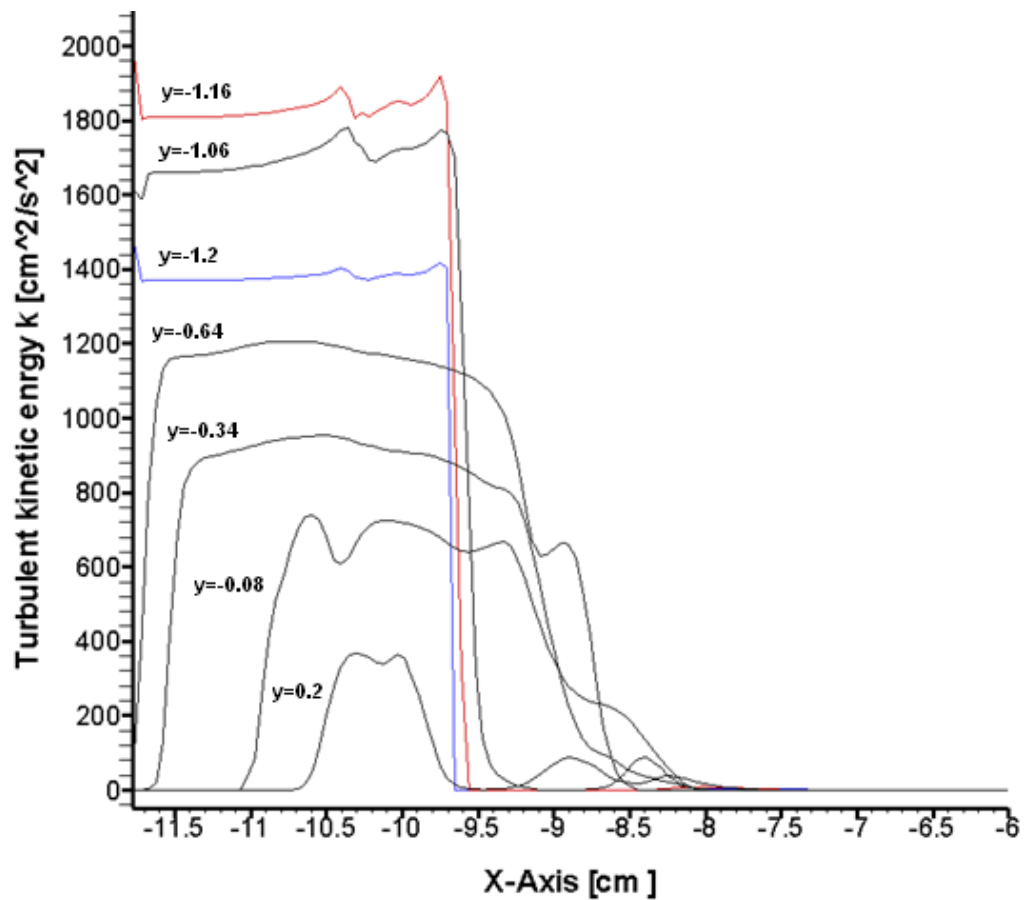
Figure 41: Turbulent kinetic energy k at different location on the Y-axis (blue at the nostril; Red after the nostril) for constant z=-0.25 at inspiratory flow rate of 300 *ml/s*, showing two regions of high turbulent kinetic energy close to the floor of the nasal cavity at the nasal valve.

Turbulence intensity *I* which is a common measure of the strength of turbulence [94] is shown in Figure 42, on the same slides as in Figure 41. Despite higher *k* values at the slide after the nostril (*Y=-1.16*) as compared to the slide on the nostril (*Y=-1.2*), the turbulent intensity is higher at the nostril. This increase in intensity is a result of lower flow velocities at this region which is inversely proportional to the turbulence intensity. Although at the second slide the intensities are lower than at the nostril but there is a peak value around the nasal valve region (about 2.2%) where the turbulent kinetic energy was shown to have a peak value for the same slide in Figure 41. The turbulent intensity profiles then start to decrease as the slides move further from the nostril. For this nasal cavity model, the peak turbulent intensity of about 9% is found located at a plane close to the nostril (Y=-1.19 & Z=-0.25) at the nasal valve, posterior to the main nasal airway.
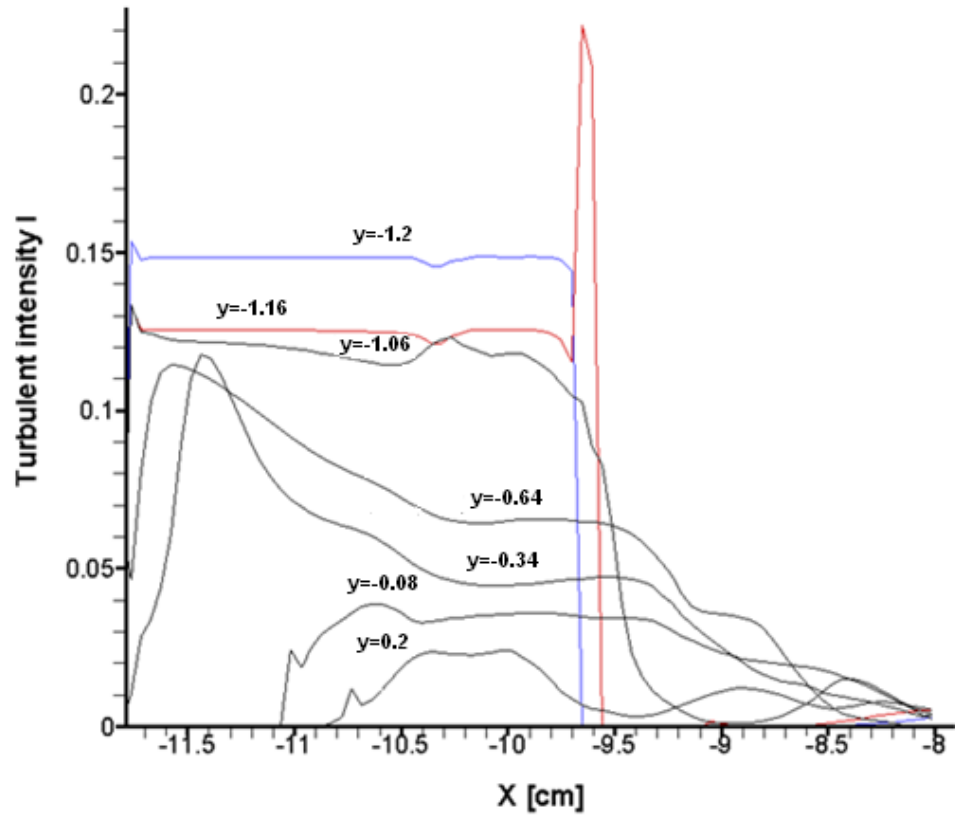
Figure 42: Turbulent Intensity I at different location on the Y-axis (blue at the nostril; Red after the nostril) for constants z=-0.25 at inspiratory flow rate of 300 *ml/s*. The location of the peak turbulent intensity is close to the floor of the cavity at the nasal valve region.

Both increases in *k* and *I* in the nasal valve region can be explained due to the abrupt reduction in the cross sectional area followed by a high degree of directional change in the flow which causes the nasal airflow to experience adverse pressure gradient which could promote transition to the turbulent flow. Similar computational results were reported by Doorly and leung [66, 67]. Same variation is observed for both *k* and *I* for two other flow rates of 250 and 200 *ml/s*, however as the flow rate decreases, there is a reduction in both Δk (difference between the peak *k* and the initial *k* value) and turbulent intensity *I*. Values of Δk are shown in Table 5 for different flow rates.

Table 5: Difference between the peak turbulent kinetic and its initial value, at different flow rates of 200, 250 and 300 *ml/s,* showing a reduction in Δk as the flow rate decreases.

$q[ml/s]$	$\Delta k[\frac{cm^2}{s^2}]$
300	8.79%
250	4.21%
200	1.90%

5.1.3.2 Turbulent Kinetic Energy in Expiration

The contour of turbulent kinetic energy is plotted for the expiratory flow rate of 300 *ml/s* in Figure 43. Unlike in inspiration, these contours are only extended for a short distance within the nasopharynx area. An increase of 3.96 % and 1.89 % in *k* relative to the inlet value is observed for the expiratory flow rates of 300 and 250 *ml/s* respectively which are almost halved from the increase observed in inspiration for the same flow rates. The peak turbulent kinetic energy occurs at the same region where the posterior vortex was observed in Figure 37.

The turbulent kinetic energy plotted at different slides on the Y-axis (Figure 44) shows that *k* has its highest value at the back of the nasopharynx close to the floor of the cavity and decreases as the flow progresses towards the main nasal airway. The graph of turbulent intensity (Figure 45) shows that close to the floor of the nasal cavity, highest intensities occur at the back of the nasopharynx, and move forward as the air flows further up towards the main nasal airway. This region of high turbulent intensity is also the region where the flow undergoes a rapid directional change.

These turbulent intensities are also smaller than the turbulent intensities measured in the inspiratory phase.

The flow field is also studied for different values of inlet turbulent kinetic energy. Despite the large changes in the inlet k value, there is no significant change in the flow field and the transnasal pressure values.
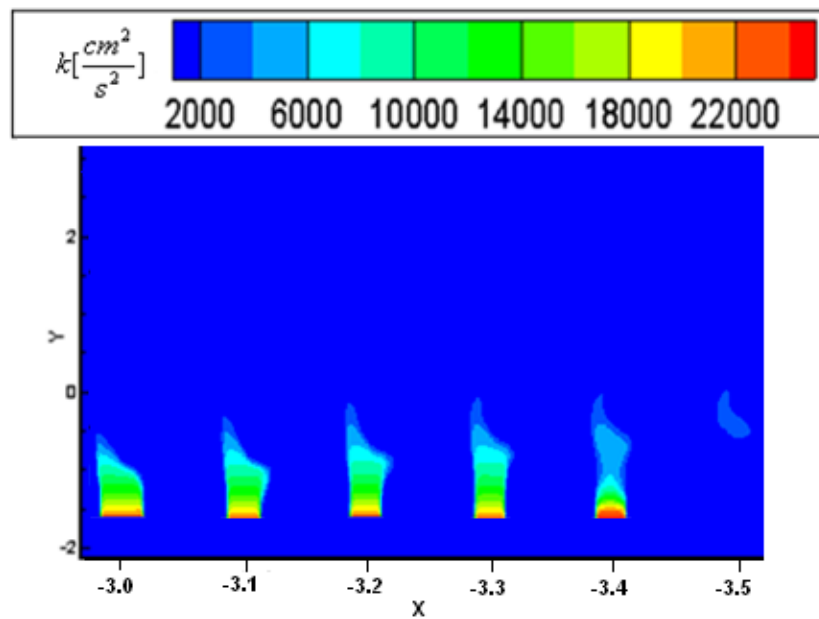
Figure 43: Turbulent kinetic energy k [$\frac{cm^2}{s^2}$] at x-axis of (-3, -3.1,-3.2, -3.3, -3.4 and -3.5 cm) from left to right for q=-300 *ml/s*, showing smaller region of extension as compared to the inspiratory phase.
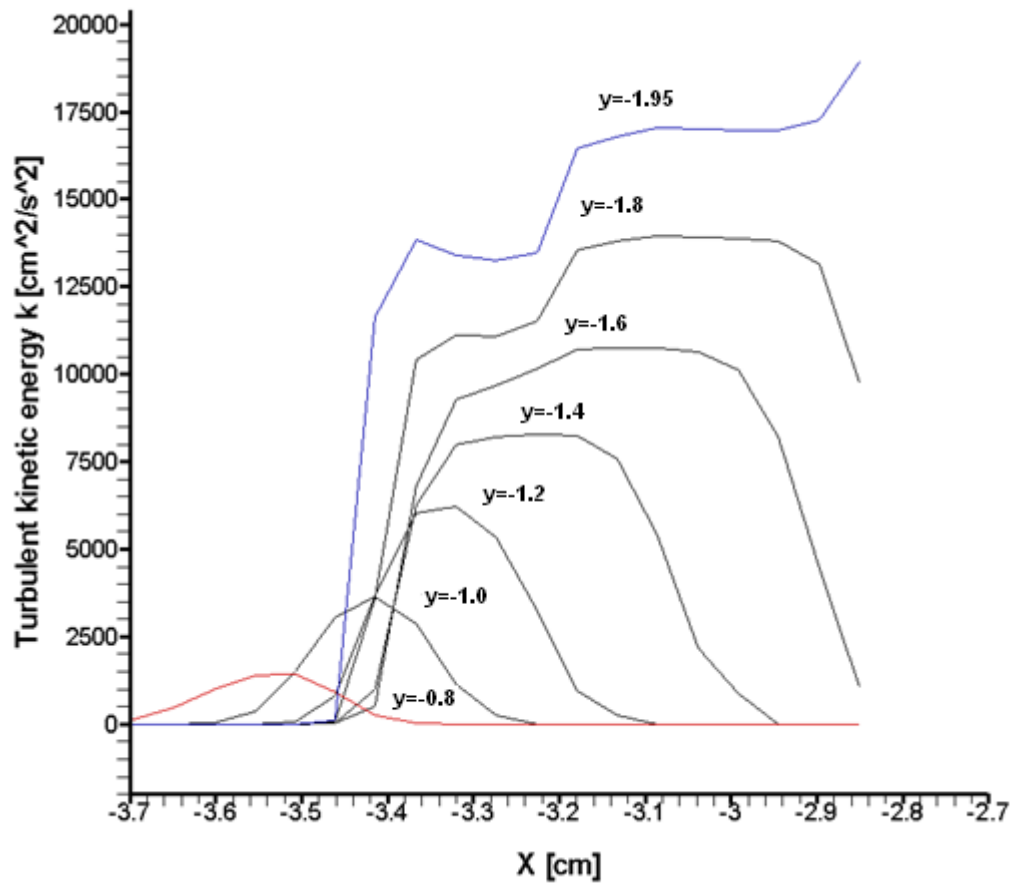
Figure 44: Turbulent kinetic energy k at different location on the Y-axis (blue closest to the nasopharynx; Red, Furthest to the nasopharynx) for constant z=-0.05, at expiratory flow rate of -300 *ml/s*.
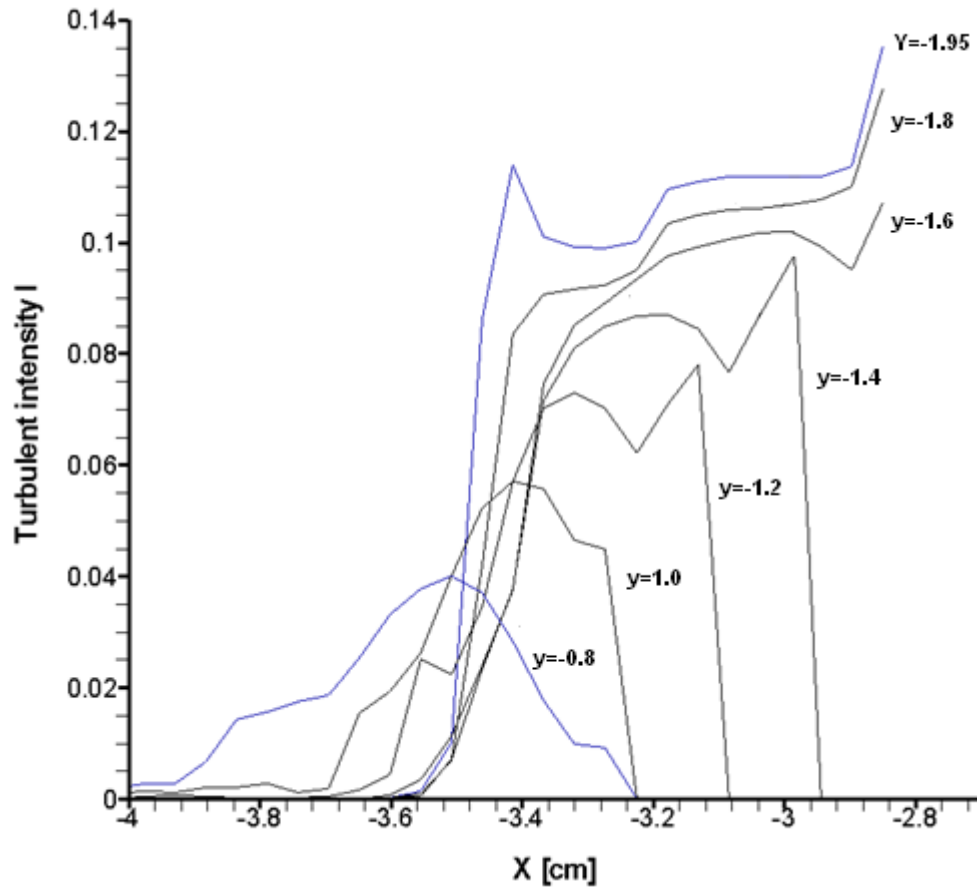
Figure 45: Turbulent Intensity I at different location on the Y-axis for constant z=-0.05, at inspiratory flow rate of 300 *ml/s*.

5.1.4 Nasal Resistance

Nasal resistance is defined as the ratio between the transnasal pressure and the volume flow rate. It is one of the most important parameters pointing how effective the nasal cavity is, in delivering the required influx. Unfortunately subjective assessments of patients suggest that despite experiencing a normal level of nasal resistance the patient may still suffer from nasal blockage [10, 11].   Therefore judgements on the condition of the nasal cavity only based on NR values should be

avoided. However NR when used with other flow characteristics can yield to suitable conclusion on the nasal cavity's inner condition.

The values of nasal resistance (*NR*) are plotted for both laminar and the RANS calculations at different volume flow rates for the safety factor (*SF*) of 0.5 which was shown to give the least numerical dissipation in Figure 7. The transnasal pressure-flow rate curve shown in Figure 46 is for an inflow value of 5% for the turbulent kinetic energy *k* as relative to the inflow value of the mean flow kinetic energy when the RANS model is considered. Both plotted curves fall within the 5%-95% of the experimental mean curves of Pallanch et al. [95], although for our particular geometry they are much closer to the 5% curve. Both the laminar and turbulent flow curves are also found to overlap with the transnasal pressure flow rate curve from experimental study of Kelly et al. [96], up to 100 *ml/s* where they start to diverge for higher flow rates. This difference between the NR resistance values maybe due to the small differences between the airway dimensions of the computational model in this study and the experimental model in Kelly's. Lower local Reynolds number in his model causes less spiralling flow component throughout the cavity and therefore less NR values.
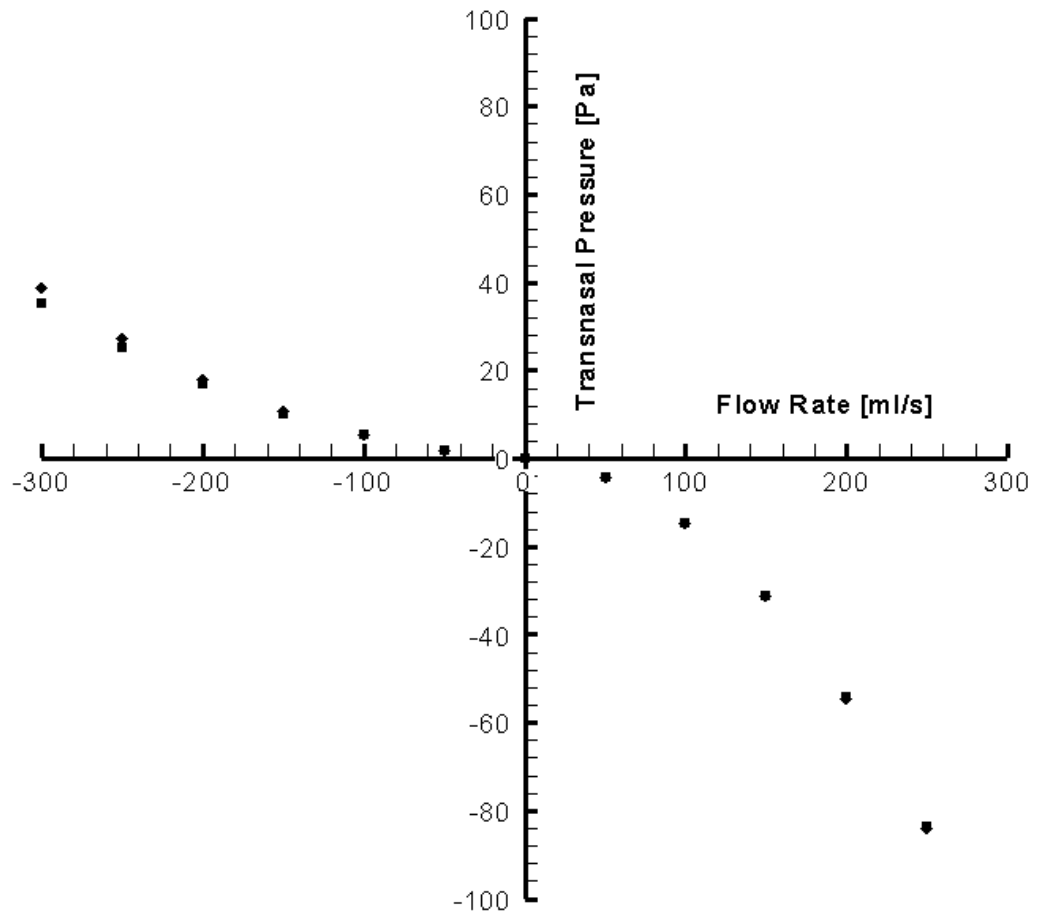
Figure 46: Transnasal-pressure flow rate mean curves calculated assuming laminar flow (▪) and transitional-turbulent flow (◆) using the low Reynolds number $k - \omega$ RANS model using the large grid, showing close predictions using both Laminar and RANS code up to 200 *ml/s*.

Using both flow cases higher nasal resistance is observed in inspiration as compared to expiration for all values of flow rate. This different is the result of higher spiralling flow component and less uniform flow pattern in the inspiratory phase which was reported earlier.

Adding the effect of turbulence by considering the RANS model shows an increase in the nasal resistance as expected especially for flow rate of 200 *ml/s* and higher. This behaviour corresponds fairly closely to the threshold of about 220 *ml/s* quoted in the literature for the onset of the effect of turbulence (Van der Leeden [29]). However this increase in higher in the expiratory phase. This is the result of introducing a higher initial turbulent kinetic energy at the nasopharynx in expiration than the initial value specified in the nostril in the inspiratory phase. Since the nasopharynx has smaller cross sectional area, 5% of the mean velocity is higher in this region than at the anterior region.

The nasal resistance values are also plotted for a wider range of flow rates in Figure 47 using the RANS flow condition only. Comparison reveals much higher pressure loss in the inspiratory phase than in expiration.
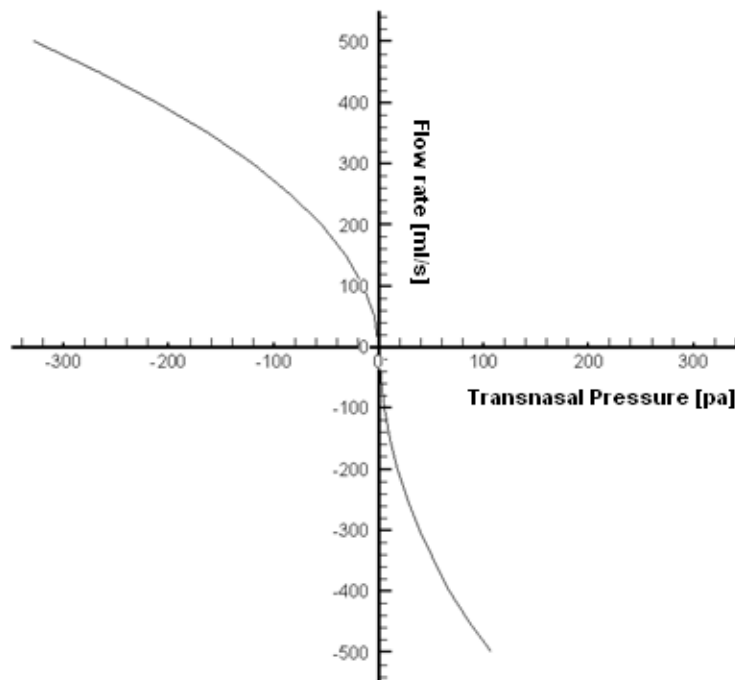
Figure 47: Nasal Resistance values using the RANS code.

Considering the variation in both *k* and *I* in addition to the respiratory flow streamlines, this increased pressure loss in inspiration can be explained as a result of turbulent at the nasal valve for flow rate of 200 *ml/s* and higher. This agrees with the experimental results from Hornung et al. [33] who also found turbulent flow in the anterior region of the nasal cavity. In expiration this transition occurs at much higher flow rates.

The inspiratory axial velocities have been measured approximately along a line on the X-axis located the nasal valve region to produce an estimated velocity profile at the inspiratory flow rate of 300 *ml/s* shown in Figure 48. Comparing this profile to the general outlines for the laminar and turbulent flows, also suggest that the velocity profile is closer to the turbulent flow.
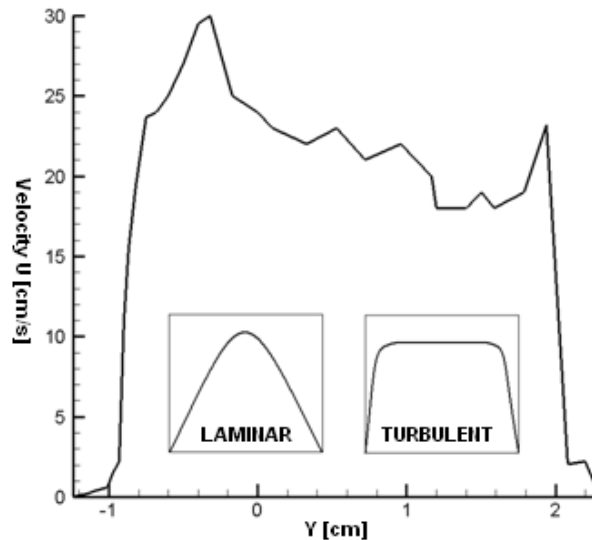
Figure 48: Approximate 2 dimensional velocity profile at the nasal valve region for the inspiratory flow rate of 300 *ml/s*. Inserted graphs are general outlines for laminar and turbulent velocity profiles.

5.2 External Nasal Flow

The computational grids are extended to allow calculations of flow outside the nasal cavity. Information about the nasal airflow outside the cavity is then going to be compared to the PIV experimental results for further analysis. This is a vital step if the idea of using information on the external airflow field to gather information about the cavity's inner flow pattern (open or blocked) is to take place. The nasal cavity including the regions for the external flow is shown in Figure 49.

Flow calculations have been carried out using a grid resolution of $(N_X, N_Y, N_Z) = (174, 173, 147)$ points. Constant pressure was used for the boundary condition on the outer computational domain edges, coupled with zero gradient condition for velocities. Thus the computations mimicked the conditions where the patient blocks one of the nostrils. Only the expiratory flow was considered due to its importance for assessing the effect of internal cavity blockage on the external flow. In this section the nasal cavity is considered to be free of any blockage similar to in the previous section.
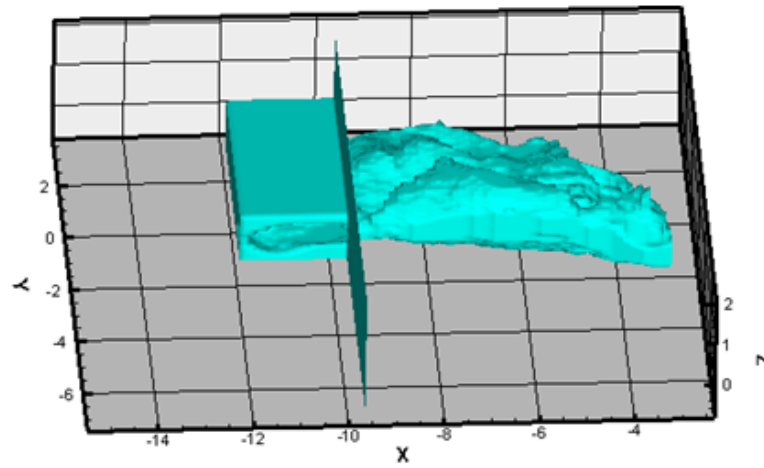
Figure 49: Nasal cavity computational model including the external region for investigation of the external nasal airflow pattern.
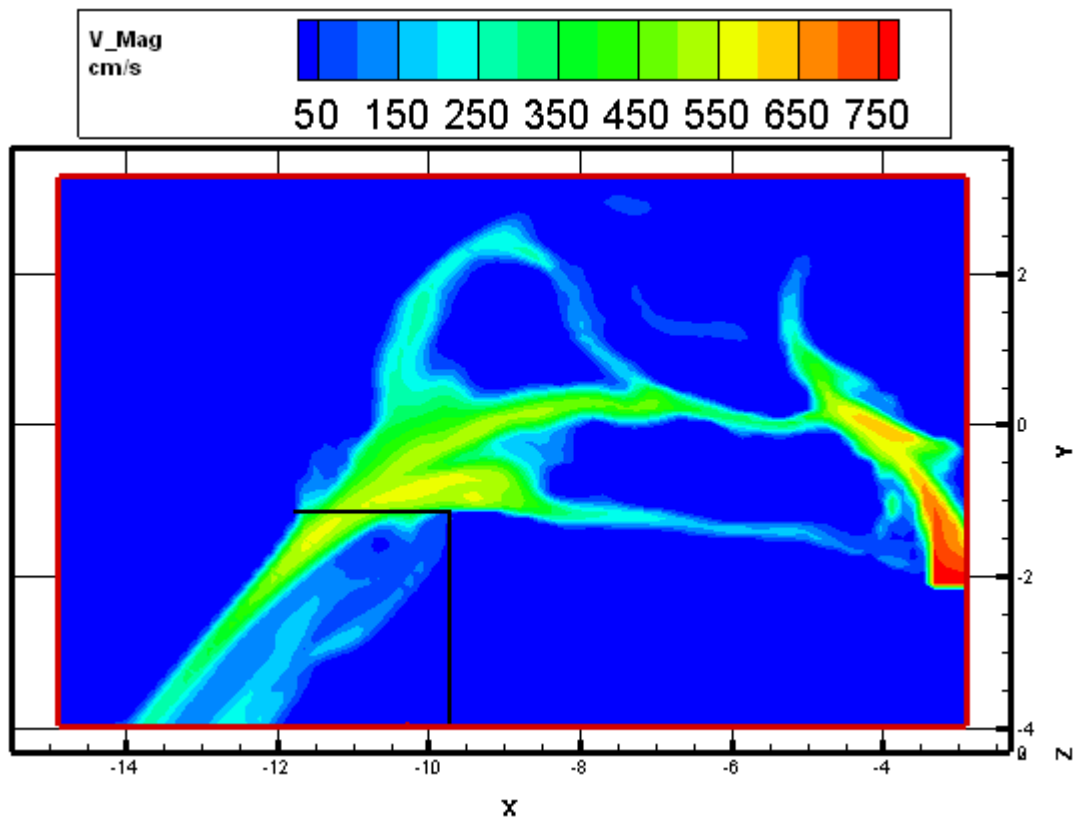
Figure 50: Sagittal velocity magnitude contours at the expiratory flow rate of -250 *ml/s* showing both internal and external nasal airflow pattern.

The velocity magnitude contour in the sagittal cross section, shown in Figure 50, reveals that the highest velocities occur at the tip of the nostril as the flow leaves the cavity and continue to be higher at that region as the flow progress. Similar flow field is also observed for expiratory flow rate of 50 *ml/s,* with only smaller velocities, suggesting the independency of the external flow field of the expiratory flow rate.
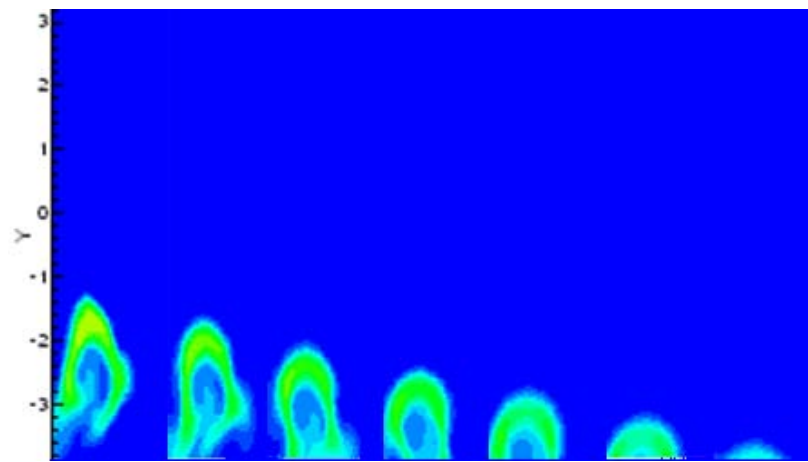
Figure 51: Velocity magnitude contours outside the nasal cavity at different X-axis (from left to right: -11.8, -12.13, -12.46, -12.8, -13.13, -13.46 and -13.8 *cm*) at expiratory flow rate of - 250 *ml/s*.

Plotting the coronal velocity contours (Figure 51) outside the nasal cavity on different X-axis initially shows a horse shoe shape which converges as one side rolls up, as the flow moves downstream. This convergence occurs as a result of cross flow component which is shown in *(Figure 53: a)*.
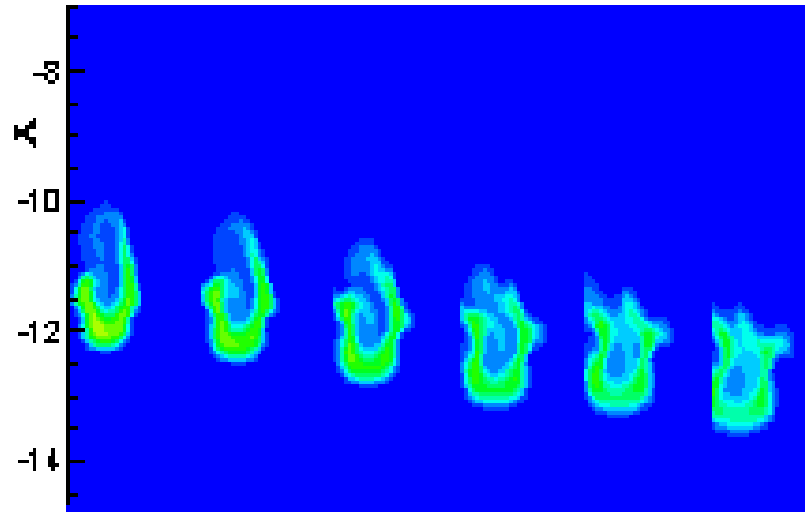
Figure 52: Velocity magnitude contours outside the nasal cavity at different Y-axis (from left to right: -2, -2.33, -2.66, -3, -3.33 and -3.66) at expiratory flow rate of -250 *ml/s*.

Figure 52 present the external velocity magnitude at different Y-axis. Here the flow profile forms a close ring as the flow progresses. This closure occurs due to strong cross flow component which is shown in (Figure 53: b).
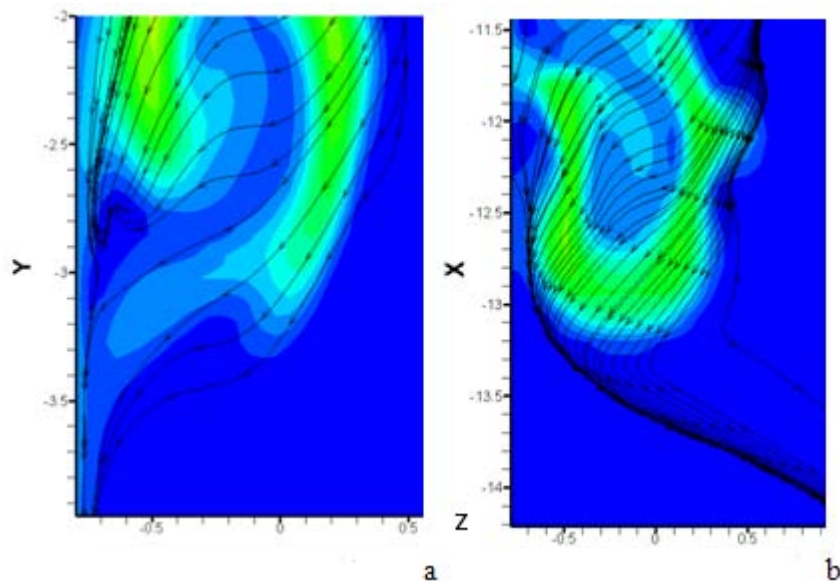
Figure 53: Velocity streamlines at a slide located at -11.5 *cm* on the X-axis showing, flow leaving the nostril (a) and on the Y-axis at -3 *cm* in (b) at -250 *ml/s*.

The cross flow velocity component outside the nostril occurs as the airflow in the middle airway is deflected towards the lower region at the exit of the nasal cavity (Figure 54) as well the velocity gradient across the external flow. As the flow moves further downstream this velocity component becomes weaker. The deflection in airflow pattern occurs due to the anterior vortex observed in the nasal cavity, which is also responsible for the reverse flow noted previously at the nostril cross section. Similar behavior is also observed for other expiratory flow rates.
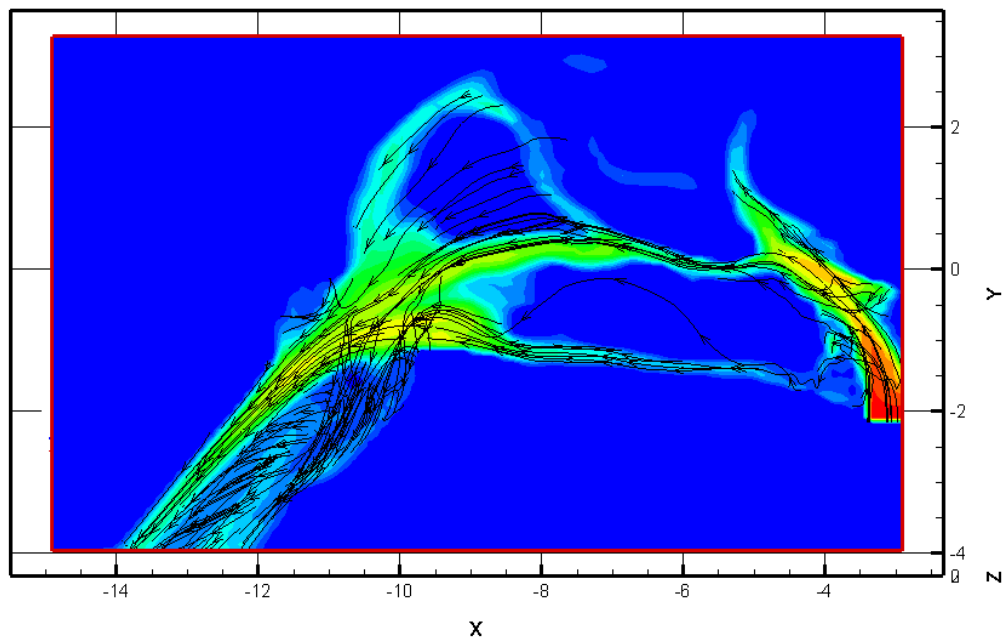
Figure 54: Internal and external flow streamlines inside and outside the nasal cavity at expiratory flow rate of -250 *ml/s*.

Looking at the normal velocities at the nostril cross section, using both extended and the normal RANS codes at expiratory flow rate of -250 *ml/s* in Figure 55 shows

a similar flow patterns. The similarity between the two flow patterns confirms the reverse flow reported previously.
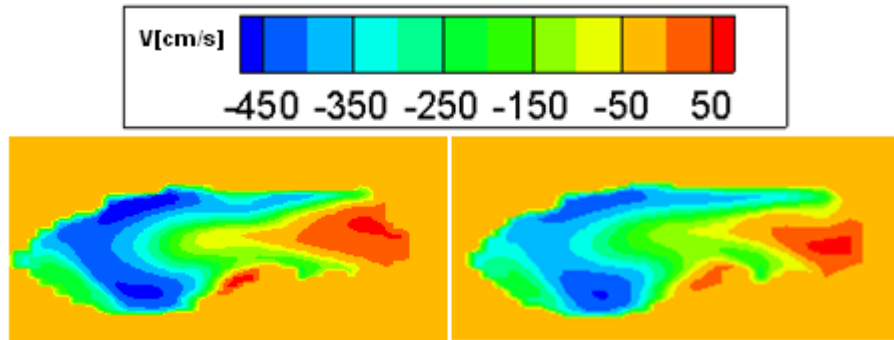
Figure 55: Nasal airflow field at the nostril using the RANS computational code (Right) and the extended RANS computational code including the external flow (Left) at expiratory flow rate of -250 *ml/s*. Both contours show reverse flow at the lower part of the nostril.

5.3   Summary

For the internal nasal airflow pattern, in the anterior and posterior sections the highest velocities were observed in the nasal valve and the nasopharynx regions due to the reduction in the cross sectional area. In the turbinated region the flow had its highest velocities along the floor of the lower and middle airways, where the nasal resistance is lowest. A reduction in velocity magnitude was also observed, as the flow moved from the septum side towards lateral wall. Despite the small amount of flow observed in the upper airway throughout the nasal cavity, there was an increase in the inspiratory nasal airflow in the olfactory region which is believed to aid with the olfaction. Higher flow velocities in expiration as compared to the inspiratory phase, suggests that the inspiratory flow spends longer in the nasal cavity which enhances the nasal conditioning. This difference was explained due to stronger

vortices in inspiration. The expiratory field was found to be more uniformly distributed due to an increase in flow through the meatuses as a result of stronger cross flow component. In both respiratory phases the flow field was found to be independent on the influx rate. Only an increase in velocity magnitudes was observed as a result of increasing volume flow rate.

The inspiratory velocity streamlines suggested that the flow path is dependent on the location of entrance on the nostril. Two flow vortices were observed at the influx rate of 250 *ml/s* in the nasal valve region and the nasopharynx due to the sudden expansion in the cross sectional area and the steep directional change respectively. The anterior vortex was shown to disappear at a lower volume flow rate of 50 *ml/s*, where the flow still exhibited swirling pattern in the posterior region. This was explained due to the reduction in flow velocity which allows the flow to handle the sudden expansion in the anterior region more efficiently. Two flow vortices were also observed at the expiratory flow rates of 250 at the anterior and the posterior regions of the nasal cavity, due to the nozzle effect and the directional change in flow direction respectively. The expiratory vortex in the anterior region was found to be responsible for the reverse flow observed at the nostril in expiration.

An increase in turbulent kinetic energy relative to the inlet value was observed for both inspiratory and expiratory phases, at the nasal valve and the nasopharynx respectively. However in inspiration these values were higher, and occurred for lower flow rates. In inspiration also the turbulent kinetic energy was expanded up to the main nasal airway whereas in the expiratory phase, it was only observed in the nasopharynx. Highest turbulence intensities were observed at the nasal valve region

149

close to the floor of the nasal cavity in inspiration and at the nasopharynx in expiration. Turbulent intensities were also higher in the inspiratory phase.

Studying the variation in NR using both the Laminar and RANS codes showed higher nasal resistance in inspiration than the expiratory phase. There was also an increase in transnasal pressure as a result of adding the effect of RANS flow condition. Considering the NR values coupled with the variations in turbulent kinetic energy and turbulent intensities suggests that there might be an increasing proportion of turbulence only in the inspiratory flow phase with its onset at the nasal valve region for flow rates of 200 *ml/s* and higher. Promotion of turbulence in the inspiratory phase at the nasal valve region explains the lower inspiratory velocities observed at the main turbinated region which can be a mechanism for enhancing the air conditioning due to an increasing convective mixing. At lower flow rates (less than 200 *ml/s*), there is no turbulence as the low speed flow can spend sufficient time in the main airway for air conditioning. Having a laminar flow in the expiratory phase is logical since the flow does not need to be conditioned and it requires less effort. This assumption was confirmed by plotting an estimated velocity profile at the nasal valve region which was found to be closer to the turbulent profile outline than the laminar profile.

The investigation of the nasal airflow field outside the nostril revealed that the highest velocity magnitude of the nasal airflow leaving the cavity is located close to the tip of the nostril. The flow streamline was shown to converge as the flow progressed. The flow was also found to have a component towards the septum side across the main flow stream as a result of flow deflection caused by the anterior

150

vortex. Comparison between the flow fields at the nostril cross section for the inner flow field and the external flow field confirmed the reverse flow at the nostril during the expiration which is believed to be a result of anterior vortex. The external flow patterns were also found to be independent on flow rate.

6. Chapter 6

Influence of Nasal Blockage on Flow Dynamics and Physiology

The most obviously functions of the nasal cavity are the respiration and the sense of smell. The nasal cavity also efficiently conditions the inspired air to alveolar conditions by the time it leaves the nasal cavity into the nasopharynx [97]. All these functions are strongly dependent on the nasal cavity airflow dynamics. Any obstruction within the nasal cavity may interfere with the nasal airflow and impair the physiological functioning of the cavity. It is therefore important to investigate the influence of obstruction on the nasal airflow pattern for diagnostic purposes.

For this the nasal cavity was blocked at various regions in an attempt to simulate clinical situations. These blockages were created by putting zero airflow through certain regions to simulate some of the most common anatomical abnormalities such as deviated septum, hypertrophic inferior and superior turbinate and nasal polyps. The internal and external nasal airflows were then investigated and results were compared to the airflow field from the normal nasal cavity free from any obstruction.

6.1   Deviated Septum

A deviated septum is a common anatomical variation in healthy adults [98] and occurs when there is a shift in the nasal septum from the centre position due to birth defect or injury. Minor deviation usually does not influence the breathing and there are no symptoms associated with that. However severe cases may cause many problems such as inflammation, infection of sinuses, nosebleed and headache. Blockages have been added to two different regions inside the cavity one at a time to produce computational models of cavities with septal deviation in an anterior and posterior section. Figure 56 compares the normal nasal airways and those with deviated septum.
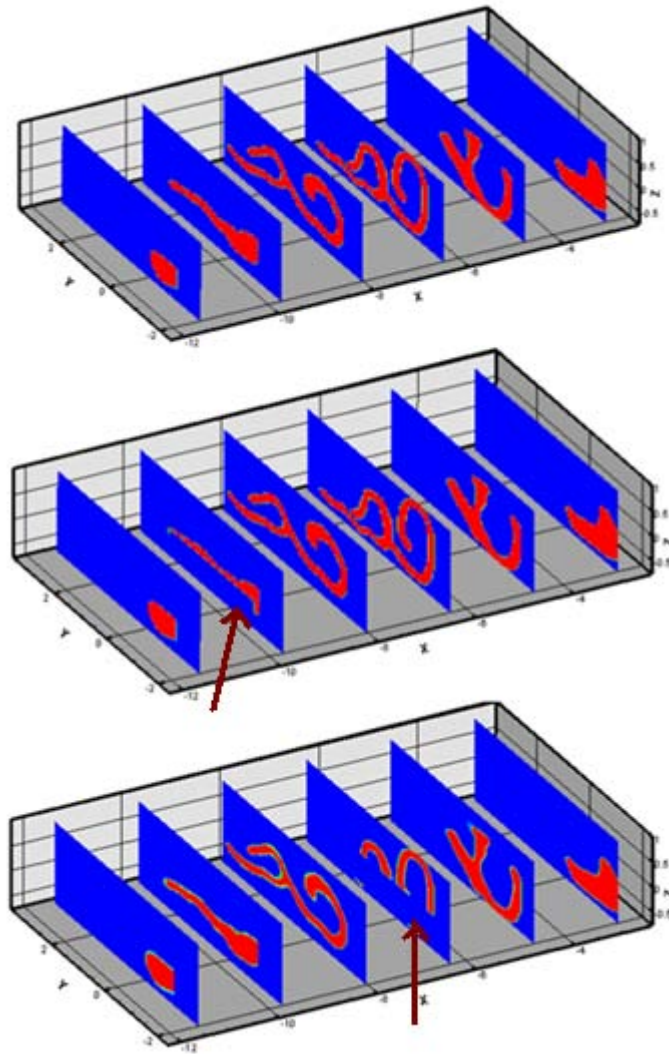
Figure 56: Normal nasal cavity (Top), cavity with anterior deviated septum (Middle: blocking the anterior region marked by the red arrow) and the cavity with deviated septum blocking the posterior part (Bottom: Marked by the red arrow). For locations of nostril and nasopharynx refer to Figure 5.

6.1.1 Internal Respiratory Flow Field

The inspiratory velocity contours for an influx rate of 200 *ml/s* are plotted in Figure 57. Each contour reveals a unique flow field, although there are similarities. An increase in velocity magnitude is observed for both obstructed cavities at the location

of the blockage due to narrowing of the nasal airways. This increase is more visible in Figure 58.

Contours also reveal a reduction in flow by almost half, through the olfactory region in both blocked cavities compared to the normal nasal cavity. This reduction which is slightly higher in the cavity with the anterior blockage suggests that a normal nasal cavity is designed to supply more air to the olfactory region where the presence of septal deviation may impair this mechanism. The influence of variation in anatomical structure of the cavity's anterior region on the olfactory function has been reported previously by Zhao et al. [59].

The highest and the lowest velocities are found within the cavity with the anterior blockage, at the anterior region and the nasopharynx respectively. This suggests that the narrowing of the anterior region posses a high resistance on the airflow which causes the flow losses high amount of energy before reaching the other sections.
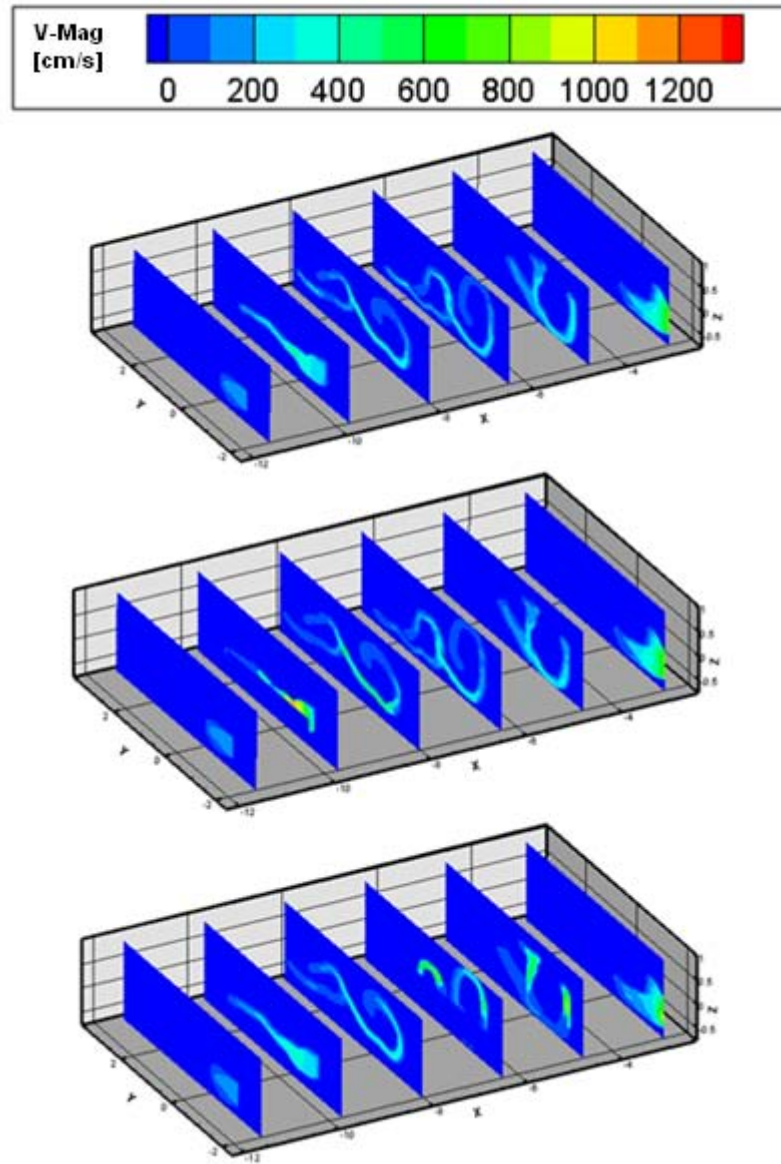
Figure 57: Inspiratory velocity magnitude contours at flow rate of 200 *ml/s* for the normal nasal cavity (Top), nasal cavity with deviated septum blocking the anterior region (Middle) and the cavity with deviated septum blocking the posterior region (Bottom). An increase in velocity magnitude is observed at the location of blockage.
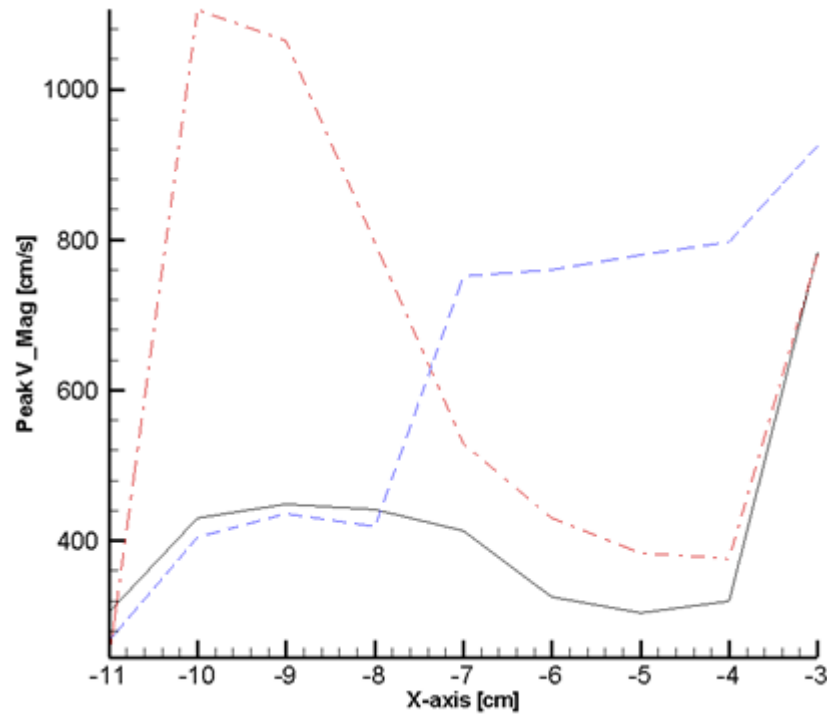
Figure 58: Peak velocity magnitude along the X-axis for the normal nasal cavity (black), nasal cavity with deviated septum blocking the anterior region (Red: dashed-doted) and blocking the posterior region (blue: dashed). Highest velocities are observed for the cavity with the anterior blockage.

The flow fields shown in Figure 59, for the expiratory rate of -200 *ml/s* also exhibit distinctive characteristics. Similar to the inspiratory phase there is an increase in velocity magnitude where blockages narrow the nasal airways.

In both respiratory phases, at the location of blockage, the peak velocity magnitudes are much larger (by three time and almost double for the anterior blockage and the posterior blockage respectively) than the peak velocities in the normal nasal cavity.

These results show considerable variation in the respiratory nasal airflow due to the septal deviation. This is however different to the experimental results by Proetz et al. [53] and Chung et al. [34] who reported no changes in the nasal airflow field for a

cavity with a deviated septum. This can be explained due to different cavity models used in those experiments. Proetz et al. [53] investigated the nasal airflow dynamics using a cadaver model which could have significantly reduced the accuracy of the data as its small size may have interfered with flow measurements. Chung et al. [34] constructed an experimental model from the CT scan of a patient suffering from a deviated septum. Despite the septal deviation in this model, similar airways width were found to that of normal nasal cavity as a result of compensatory hypertrophy of turbinates and the development adaptation of another nasal structure [99] which at this study was believed to be responsible for nearly equal airflow patterns.
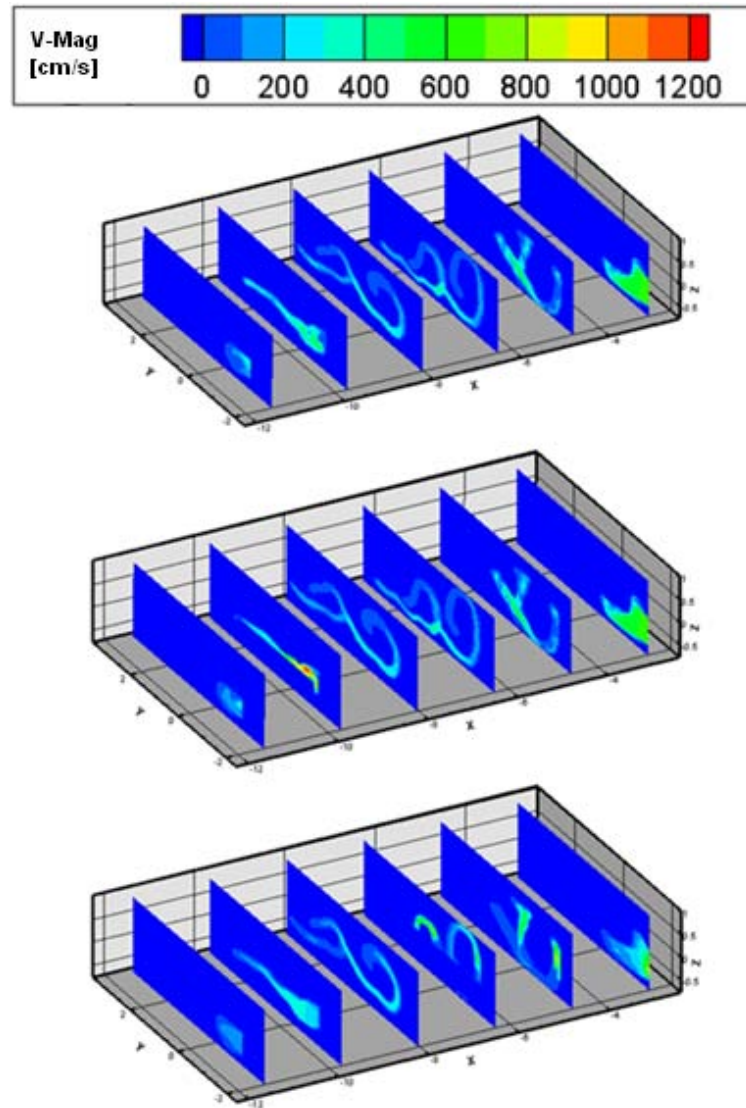
Figure 59: Expiratory velocity Magnitudes for Normal nasal cavity (Top) and cavity with deviated septum blocking the anterior section (middle) and the posterior section (bottom) at flow rate of -200 *ml/s*.
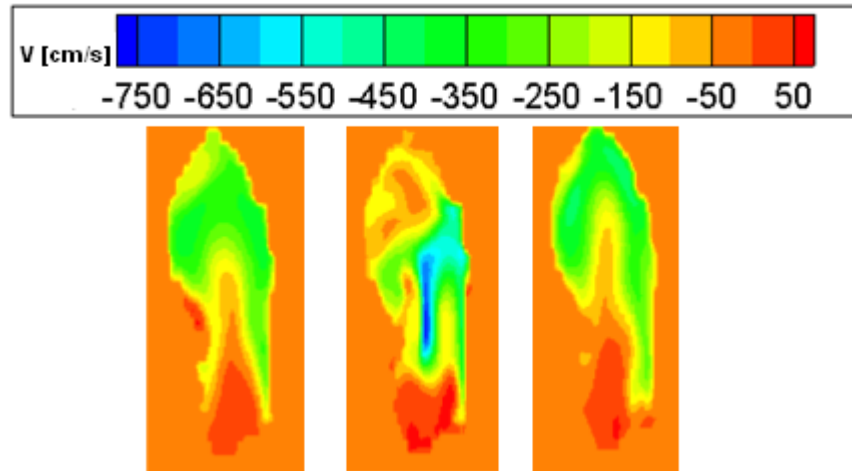
Figure 60: Normal velocity magnitude contours at the nostril for the normal nasal cavity (Left), and cavities with deviated septum blocking the anterior region (Middle) and the posterior region (Right) at the expiratory flow rate of -200 *ml/s*. The contours reveal a significant change in velocity profile after adding the anterior blockage and a slight change after adding the posterior blockage.

Figure 60 shows the normal velocity magnitudes at the nostril cross sectional area, for the normal nasal cavity and the obstructed cavities. The flow fields are the most distinctive for the normal nasal cavity and the cavity with the anterior blockage. The addition of the anterior blockage displaces the position of peak velocity magnitude from near the tip of the nostril to the centre along a straight line. Posterior blockage also changes the flow field slightly, creating a peak velocity region bigger than in the normal nasal cavity.

6.1.2 Transnasal Pressure & Turbulent Kinetic Energy

Table 6 reveals an increase in both the transnasal pressure and nasal resistance for the inspiratory rate of 200 *ml/s*, after adding nasal the blockage due to the narrowing of the nasal airways. The cavity with the anterior blockage shows a higher increase

than the nasal cavity with the posterior blockage. This is expected since the anterior region contributes the most to the nasal resistance and therefore its condition has the most influence on the nasal cavity [68]. Similar results have been reported in a computational study carries by Zambetti et al. [100].

Table 6: Turbulent kinetic energy, transnasal Pressure and nasal resistance values of normal and cavities with deviated septum blocking the anterior and posterior regions of the main nasal airway, for the inspiratory flow rate of 200 *ml/s*.

Cavity at 200 *ml/s*	$\Delta k \dfrac{cm^2}{s^2}$	$Pd[Pa]$	$NR[\dfrac{Pa.s}{ml}]$
Normal	1.9%	54.36	0.27
Anterior deviated septum	8%	123.732	0.6
Posterior deviated septum	-0.1%	102.043	0.5

Studying the variation in turbulent kinetic energy for the cavity with anterior blockage shows a significant increase in Δk, of four times the value measured for the normal nasal cavity. This increase in turbulent kinetic energy compared to the normal nasal cavity is due to an increased velocity magnitude in the nasal valve region which coincides with the location of the anterior vortex in the normal nasal airflow. Higher velocities in this region create more flow fluctuation and hence increase the level turbulence. This influence of velocity magnitude at the anterior region on the turbulent kinetic energy was previously reported as reducing the inflow flux was accompanied by a reduction in Δk. No further increase in k from the inlet

value is observed for the cavity with the posterior blockage. This is expected since the velocities in the anterior region are smaller compared to the normal nasal cavity.

Comparison between the velocity's streamlines for the normal cavity and cavity with anterior blockage (Figure 61) shows more irregular flow behaviour for the blocked nose due to an increase in velocity magnitude. Measuring the turbulent intensities however show smaller values for the blocked cavity than the normal nasal cavity due to an increased velocity magnitude in the nasal valve region. This reduction in turbulent intensity in the anterior region as a result of septal deviation has also been reported in a computational study carried out by chen et al. [101]. The peak turbulent intensity of 5% is found close to the floor of the cavity, just posterior to the main nasal airway. This irregularity of the flow pattern combined with the reduced turbulent energy can enhance the sensation of discomfort in breathing and reduce the conditioning efficiency. Similar results were also reported in other experimental and computational studies [98, 102, 103].
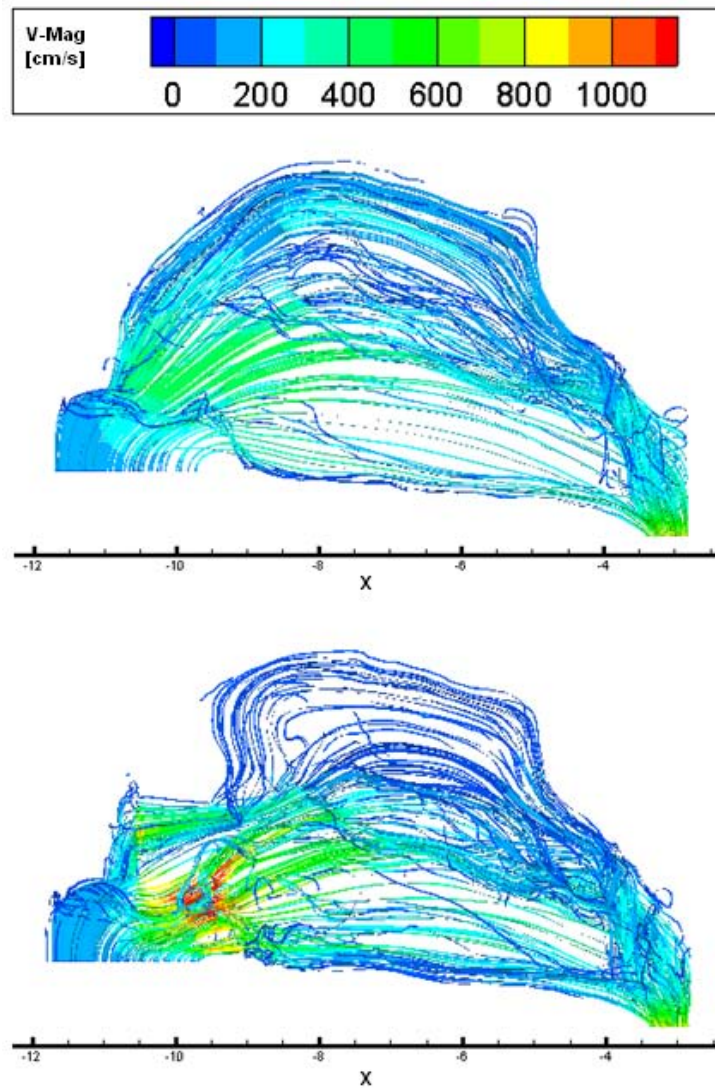
Figure 61: Velocity streamlines for the normal nasal cavity (Top) and the cavity with deviated septum blocking the anterior region (Bottom) at the influx rate of 200 *ml/s*, showing stronger vortices and increased irregularity of the flow field due to the anterior blockage.

6.1.3 External Expiratory Flow
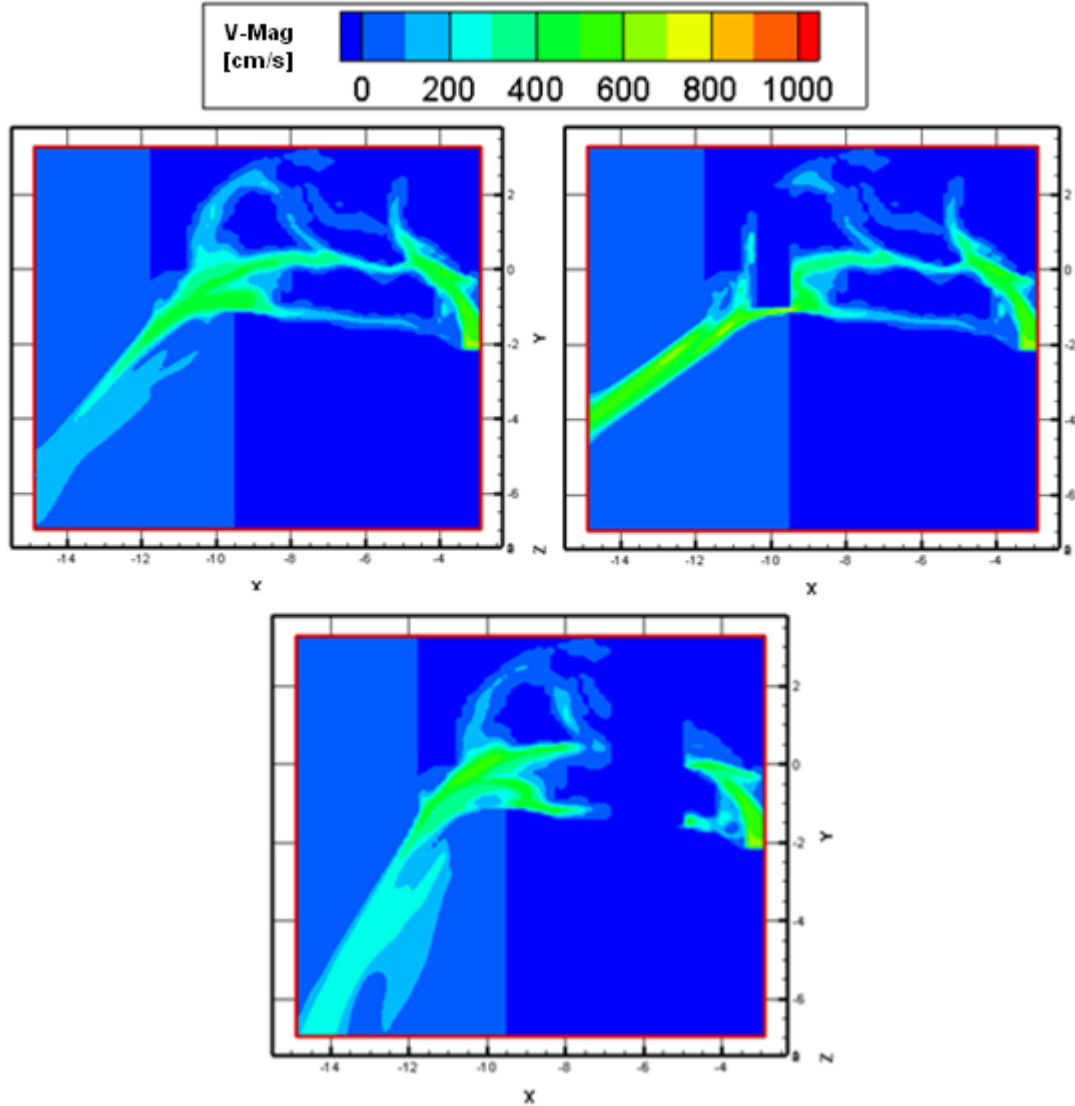
Figure 62: Velocity magnitude contour of external and internal nasal airflow fields at the expiratory flow rate of -200 *ml/s*. Normal nasal cavity (Left), cavity with anterior blockage (Right) and posterior blockage (bottom). The external flow angle and the external flow thickness is varied after adding the blockage to the nasal cavity.

The contours of velocity magnitude including both internal and external nasal airflow fields are shown in Figure 62. Comparison between the cavity with the

anterior blockage and the normal nasal cavity shows an increase in both velocity magnitude and the external flow angle (the angle between the external flow stream and vertical line representing the face) as the flow leaves the cavity from the nostril. This is a similar case as one narrows a flexible water hose near its exit causing the water to flow faster (continuity conservation) and with a higher angle (although one has to acknowledge that in water flow gravity plays a higher role).

The addition of the posterior blockage also changes the external flow field by increasing the thickness of the main flow stream leaving the nostril. Again here the analogy to the water hose holds. Narrowing its width far from the exit will accelerates the water inside but it will have time to recover inside the hose. Nevertheless depending on the location of the narrowing the water will come out with a higher velocity but in a less organised velocity profile causing the thickening of the water stream outside. For the normal cavity and the cavity with a posterior blockage the difference between the external flow fields increases as the distance to the nostril increases pointing to an accumulated influence of the difference in the velocity profile at the nostril.

6.2 Enlarged Inferior Turbinates and Nasal Airflow Dynamics & Physiology

Nasal obstruction due to inferior turbinate hypertrophy is a common complaint encountered in the practice of Rhinology [104]. The turbinates may enlarge due to a deviated septum, allergies, non allergic rhinitis or sinus infections. The most common symptoms include facial pain and nasal drainage problems [105-107].

To simulate this condition, the lower turbinate is extended at the anterior region of the main nasal airway to partially block the lower meatus and the airway. Another case is also considered where the enlarged inferior turbinate is at the posterior section of the main nasal airway blocking the entire lower airway and the meatus. The locations of blocked airways are shown in Figure 63.
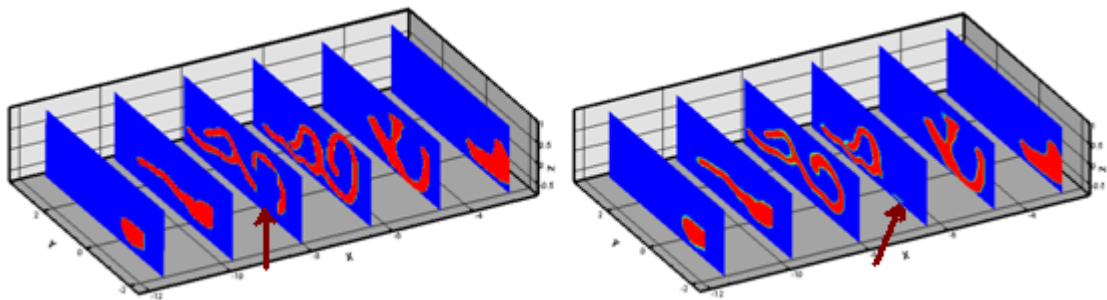
Figure 63: The nasal cavity with enlarged inferior turbinate, partially blocking the lower airway and the meatus in the anterior region of the main nasal airway (Left: Marked by the red arrow) and blocking the entire lower airway and the meatus in the posterior region of the main nasal airway (Right: Marked by the red arrow). For locations of nostril and nasopharynx refer to Figure 5.

6.2.1 Respiratory Flow Field of the Cavity with Enlarged Inferior Turbinate

Comparison between the flow fields using the cavity with and without blockages in inspiration (Figure 64) reveals a shift in flow's preferred path from the lower to the upper half with highest velocities occurring at the location of blockage. In this case however there is no flow reduction in the olfactory region, perhaps due to the increased flow flux in the upper half. This suggests that a cavity with an enlarged inferior turbinate is less likely to affect the sense of smell although due to the reduction in the cross sectional area of the nasal airway, one might suffer from dryness as the efficiency of the nasal conditioning decreases.
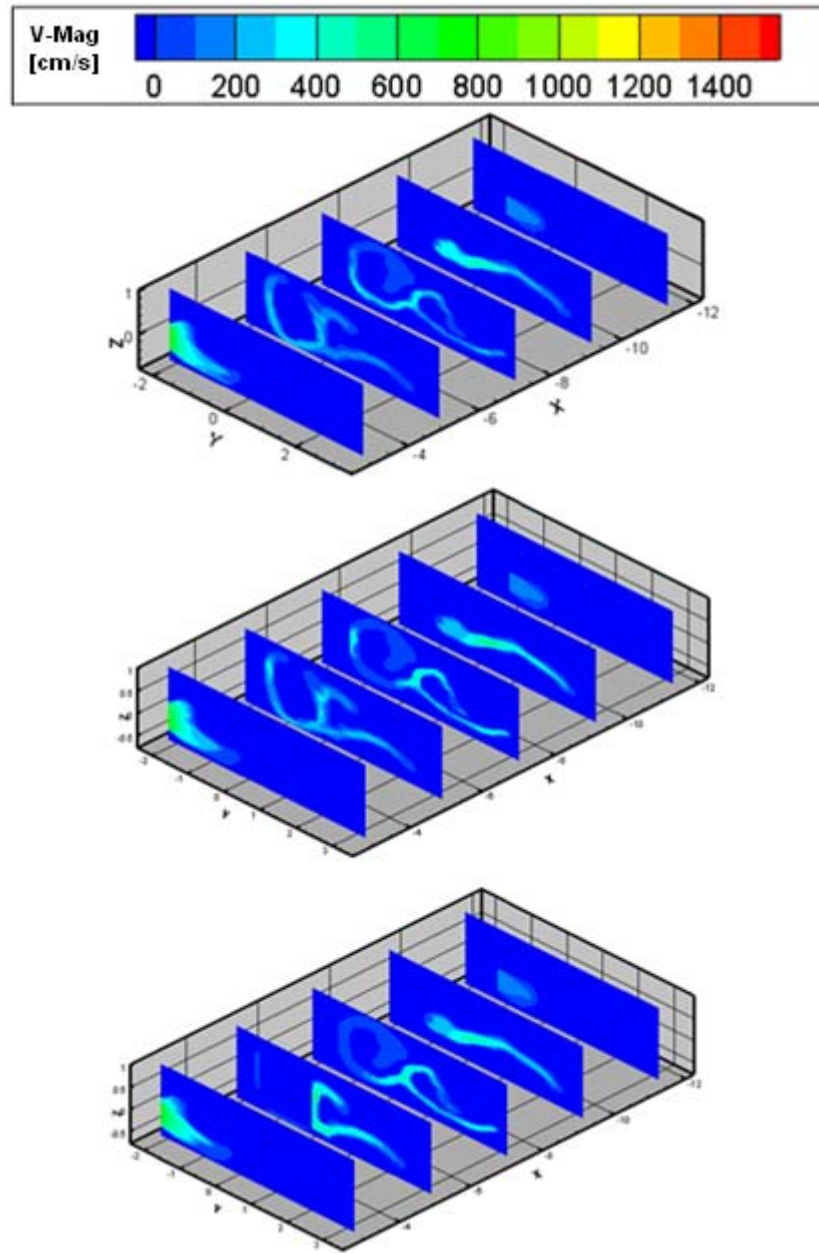
Figure 64: Velocity Magnitudes for the nasal cavity free from obstruction (Top), cavity with an enlarged turbinate partially blocking the lower airway and lower meatus in the anterior region (Middle) and the cavity with an enlarged inferior turbinate in the posterior region of the main nasal airway, blocking the entire lower airway and meatus (Bottom) at inspiratory flow rate of 200 *ml/s*. A change in the main flow path is observed from the lower half of the cavity to the upper half after addition of blockages.

The shift in flow path from the lower half to the upper half is also observed in expiration as shown in Figure 65. This displacement is much stronger for the cavity with the entire lower airway and meatus blocked creating a uniform flow field in the anterior region.

Comparison between the respiratory flows for the cavity partially blocked reveals more variation in the inspiratory airflow pattern than in the expiratory phase. This suggests the higher susceptibility of the inspired air to geometric changes, than when the air is exhaled confirming the computational results by Horschler at al. [63].

The highest velocities in both respiratory phases occur in the cavity with the anterior blockage, despite having a larger cross sectional area for the airflow compared with the cavity with the posterior blockage. This is related to the location of the blockage. In the anterior region for a normal nasal cavity the flow velocity increases due to the sudden reduction in the cross sectional area, as the flow enters the nasal valve region. A further narrowing close to this region has more influence on flow velocity compared to a reduction in the cross sectional area of the posterior region of the main airway where the flow velocities are smaller.
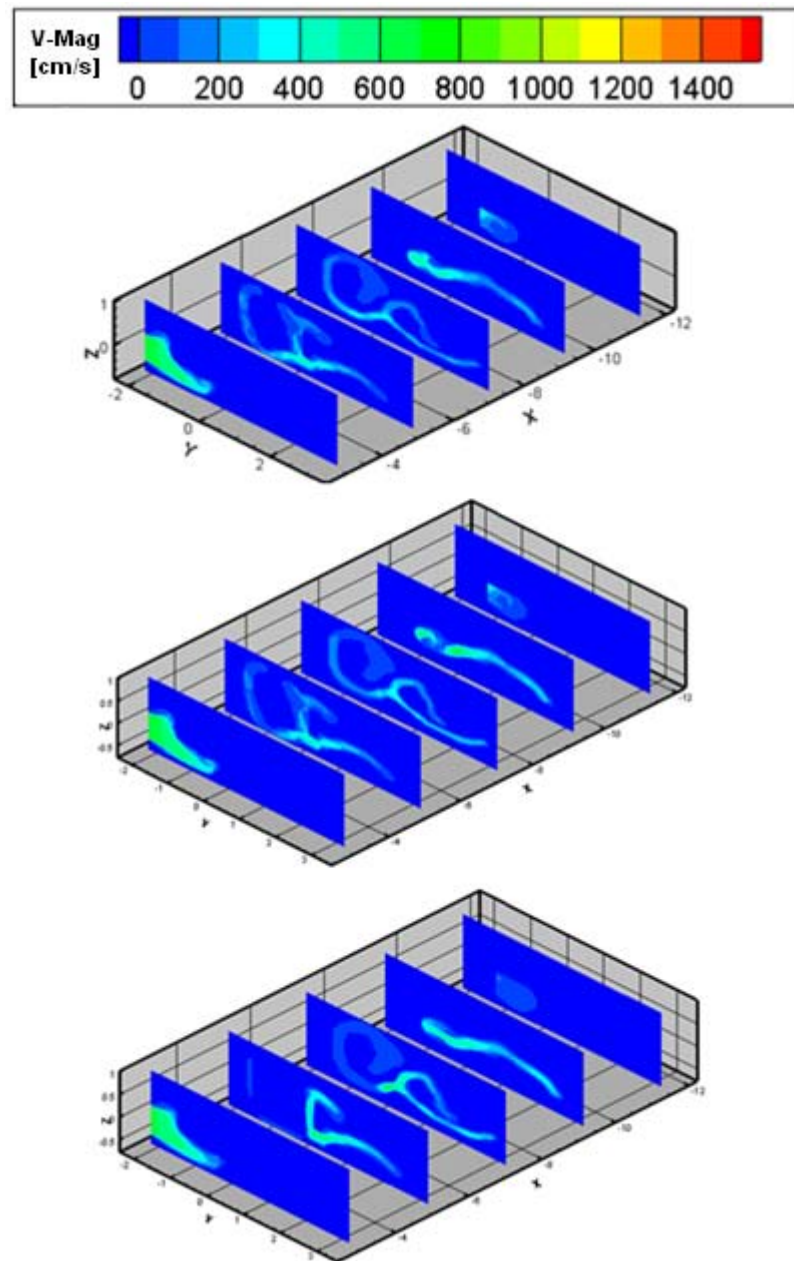
Figure 65 Velocity magnitude contours for the normal cavity (top) and the cavity with inferior turbinate hypertrophy in the main airway partially blocking the lower airway and meatus in the anterior region (Middle), and fully blocking the lower airway and meatus in the posterior region (Bottom) at the expiratory rate of -200 *ml/s*. Adding the blockages are followed by an increase in flow in the upper half of the nasal cavity.
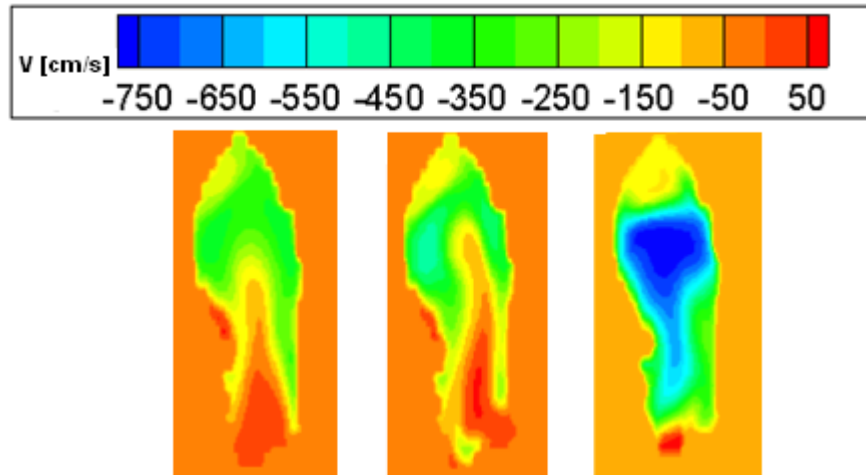
Figure 66: Normal velocity magnitudes at the nostril for the normal cavity (Left) and the cavity with the lower airway and meatus partially blocked in the anterior region of the main airway (Middle) and the lower airway and meatus fully blocked in the posterior region of the main airway (Right) at expiratory flow rate of -200 *ml/s*. Each blockage creates a different velocity profile from the velocity profile of the healthy nasal cavity.

The expiratory normal velocity magnitude contours at the nostril are shown in Figure 66. Velocity fields vary the most between the normal nasal cavity and the cavity with the posterior blockage. In this case the extension of the inferior turbinate changes the location of the peak velocity magnitude from close to the tip, to the central region, forming a T shape profile.

The influence of geometrical variation in the inferior turbinate on the nasal airflow field has also been reported in the experimental investigation of the nasal airflow by Chung et al. [34] and a numerical study carried out by Lindemann at al. [108] where a resection of this region was shown to significantly disturbed the airflow pattern by creating a massive vortices in the nasal cavity.

6.2.2 Transnasal Pressure & Turbulent Kinetic Energy for the Cavity with Enlarged Inferior Turbinate

The values of turbulent kinetic energy, transnasal pressure and the nasal resistance for the normal nasal cavity and cavities with anterior and posterior blockages due to the enlarged inferior turbinate are presented in Table 7 and Table 8 for inspiratory flow rates of 200 *ml/s* and 300 *ml/s* respectively.

Table 7: Turbulent kinetic energy, transnasal pressure and nasal resistance in inspiration for the normal nasal cavity and cavity with enlarged lower turbinate in the anterior and the posterior region of the main nasal airway at the inspiratory rate of 200 *ml/s*.

Cavity at 200 *ml/s*	$\Delta k \frac{cm^2}{s^2}$	$Pd[Pa]$	$NR[\frac{Pa.s}{ml}]$
Free from obstruction	+1.9%	54.36	0.27
Partially blocked lower airway & meatus at the anterior region	+1.7%	68.63	0.34
Entirely blocked lower airway & meatus at the posterior region	-0.5%	83.00	0.41

An increase in both transnasal pressure and the nasal resistance is observed as the inferior turbinate is extended to block the nasal cavity in both anterior and posterior regions. The values of transnasal pressure and the nasal resistance correspond to the degree of blockage since the peak values belong to the cavity where the entire lower

airway and meatus are blocked. Furthermore investigating the turbulent kinetic energy only reveals an increase in k from the inlet value for the cavity with the anterior blockage. This increase of 1.7% is smaller than the increase of 1.9% for the normal nasal cavity, as a result of flow reduction in the lower half. Despite the smaller Δk value, the turbulent intensities are quite similar to intensities in the normal nasal cavity due to reduction in mean flow velocities at the lower region. Higher nasal resistance with no changes in turbulence intensities, suggest that an enlarged lower turbinate in the anterior region may only be followed by a sensation of discomfort in breathing.

Table 8: Turbulent kinetic energy in inspiration for the normal nasal cavity and cavity with enlarged lower turbinate in the anterior and the posterior region of the main nasal airway at the inspiratory rate of 300 ml/s.

Cavity at 300 ml/s	$\Delta k[\frac{cm^2}{s^2}]$	$Pd[Pa]$	$NR[\frac{Pa.s}{ml}]$
Free from obstruction	+8.7%	119.85	0.39
Partially blocked lower airway & meatus at the anterior region	+8.1%	151.72	0.5
Entirely blocked lower airway & meatus at the posterior region	+1.9%	182.03	0.6

Similar behaviour is also observed at the higher flow rate of 300 ml/s. In this case however there is also a 1.9% increase in Δk for the cavity with the entire lower

173

airway and meatus blocked. This increase in Δk which is much smaller than the other two cavities (8.7% for the normal and 8.1 % for partially blocked cavities) is caused as the velocity magnitude in the nasal valve region increases as a result of increase influx rate.

Table 9: Values of turbulent kinetic energy, transnasal pressure and the nasal resistance for normal nasal cavity and cavities with an enlarged lower turbinate for the expiratory flow rate of -200 *ml/s*.

Cavity at -200 *ml/s*	$\Delta k \frac{cm^2}{s^2}$	$Pd[Pa]$	$NR[\frac{Pa.s}{ml}]$
Normal nasal cavity	-0.2%	18.001	0.09
Partially blocking the lower airway & meatus at the anterior region	-0.2%	30.94	0.15
Entirely blocking the lower airway & meatus at the posterior region	-6.5%	43.69	0.21

For the expiratory flow rate of -200 *ml/s* (Table 9), an increase in both transnasal pressure and the nasal resistance is observed for the blocked cavities confirming the dependency of these values on the degree of nasal blockage. The turbulent kinetic energy stays the same as in the normal nasal cavity (reduces from the inlet value) after adding the anterior blockage, since there is no significant changes in the nasal airflow field. Adding the posterior blockage is followed by a larger reduction in turbulent kinetic energy from the inlet value, since it reduces the airflow velocities in

the nasopharynx. Increasing the expiratory flow rate (Table 10) results into an increase in the turbulent kinetic energy from its initial value for the partially blocked cavity, and no further increase for the cavity with the posterior blockage.

Table 10: Values of turbulent kinetic energy, transnasal pressure and the nasal resistance for normal nasal cavity and the cavity with enlarged lower turbinate at the expiratory flow rate of -300 *ml/s*.

Cavity at -300 *ml/s*	$\Delta k \frac{cm^2}{s^2}$	$Pd[Pa]$	$NR[\frac{Pa.s}{ml}]$
Normal nasal cavity	+3.9%	38.69	0.12
Partially blocking the lower airway & meatus at the anterior region	+3.9%	68.37	0.22
Entirely blocking the lower airway & meatus at the posterior region	-2.7%	94.92	0.31

Similar results confirming these variations in the respiratory flow fields due to inferior turbinate hypertrophy have been reported in other computational studies [103, 109, 110].

6.2.3 External Expiratory Flow of the Cavity with Enlarged Lower Turbinate

The external nasal airflow is investigated only for the cavity with the anterior blockage since its expiratory flow field shown at the nostril cross sectional area

175

(Figure 66) was quite similar to that of the normal nasal cavity. For the nasal cavity with posterior blockage, the expiratory flow field at the nostril was quite different to the normal nasal cavity suggesting a different external flow pattern.
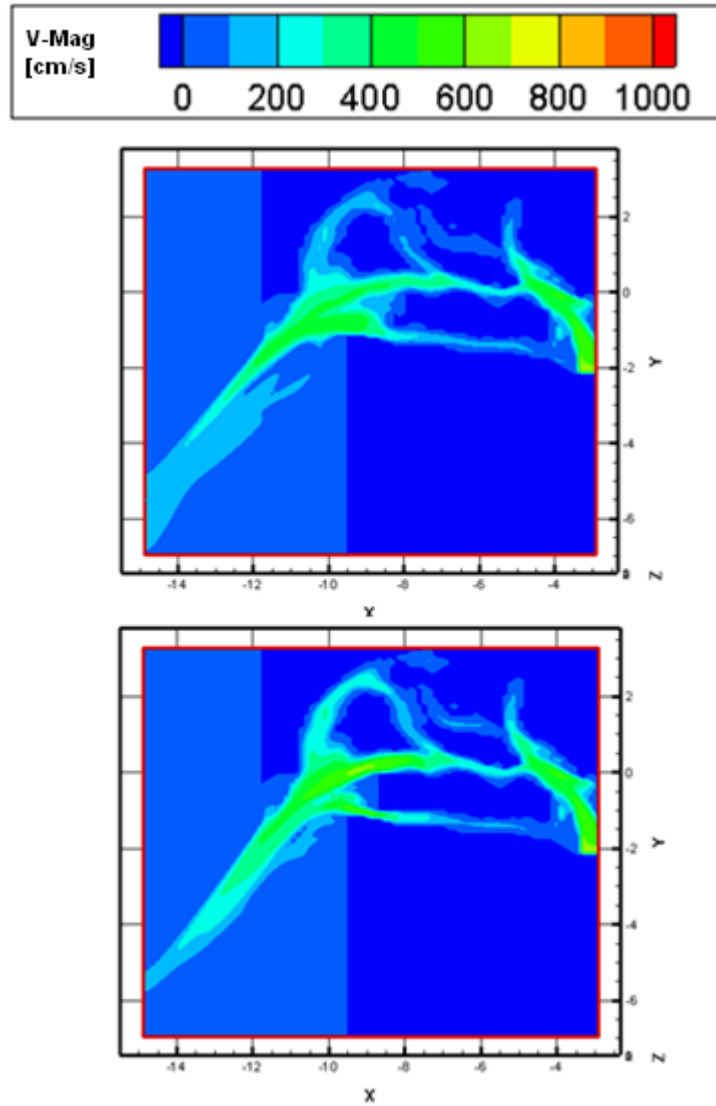
Figure 67: Expiratory nasal airflow fields (including both internal and external flows) for the normal nasal cavity (Top) and the cavity with enlarged inferior turbinate partially blocking the lower airway and meatus at the anterior region of the main nasal airway for expiratory flow rate of -200 *ml/s*. Higher velocity magnitudes are thicker external flow stream is observed for the blocked cavity.

Comparing the external flow fields in the sagittal cross sectional area (Figure 67) reveals a slightly thicker flow stream for the blocked cavity. The external flow angles are quite similar although the velocity magnitude is slightly higher at the exit for the blockage cavity. The difference between the two flow fields increases as the distance to the nostril increases.

The contours of velocity magnitude are also plotted at different coronal planes on the X-axis external to the nostril, shown in Figure 68. Comparison reveals two different coronal velocity profiles. For the normal nasal cavity highest velocities form a horse shoe shape profile which converges slightly as the flow progresses. For the blocked cavity the highest velocities are along a single line where its thickness decreases with flow progression.
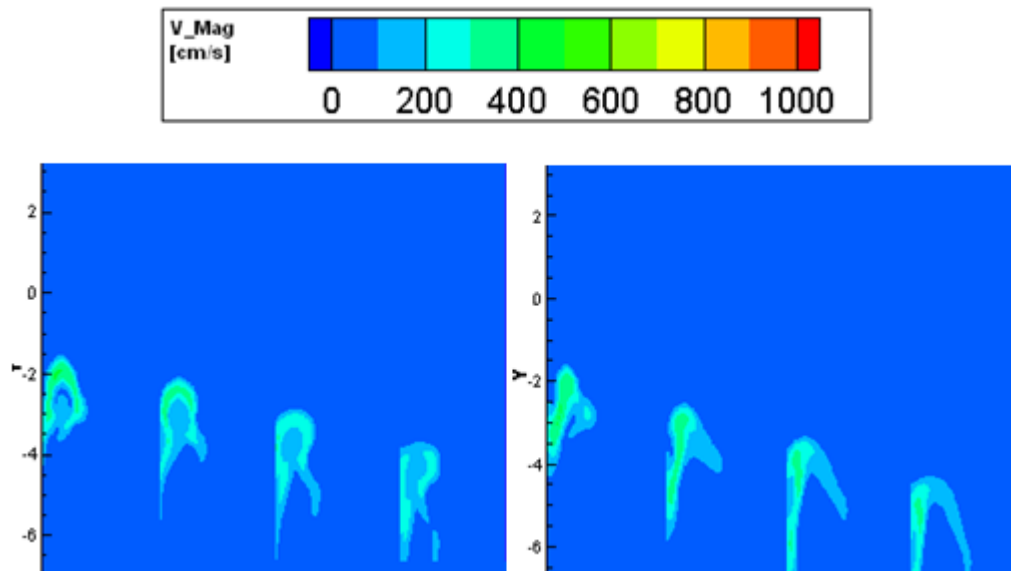
Figure 68: Velocity magnitude contours (on coronal planes) of the external nasal flow at the expiratory rate of -200 *ml/s* for normal nasal cavity (Right) and a cavity with enlarged lower turbinate blocking the anterior region (Left) on different location on the x-axis (-12, -12.66,-13.33 and -14) respectively from right to left. The coronal velocity profiles vary for the normal and the blocked cavity.

6.3 Enlarged Middle Turbinate

The middle turbinate which lies superior and posterior to the inferior turbinate is substantially smaller and thus is considered to be of less clinical significance. Similar conditions which cause lower turbinate hypertrophy may also result in an abnormal growth of the middle turbinate [111]. The middle turbinate may also enlarge due to an air pocket that can grow into the turbinate. In this section the middle turbinate is extended so that the middle meatus at the posterior part is partially blocked as shown in Figure 69.
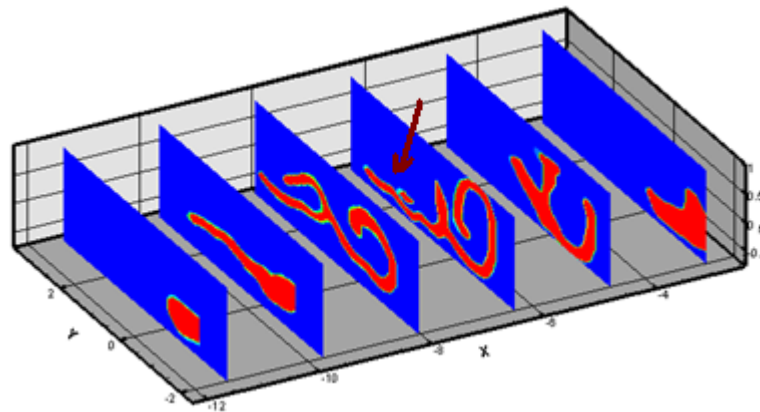
Figure 69: A cavity with enlarged middle turbinate, blocking parts of the middle meatus at the posterior region of the turbinated. The location of the blockage is marked by the red arrow. For locations of nostril and nasopharynx refer to Figure 5.

6.3.1 Respiratory Flow Field

Investigating the velocity contours in Figure 70 and Figure 71 shows similar flow patterns at both respiratory phases for the normal nasal cavity and the cavity with

blockage. Despite the similarities in the two flow fields, a small reduction in flow velocities can be observed through the upper airway, after addition the blockage, confirming the experimental results by Kim et al. [112]. The normal expiratory velocity contours at the nostril (Figure 72) also reveal similar flow fields, with the peak velocity region slightly more extended for the blocked nose compared to the normal nasal cavity at the tip of the nostril.
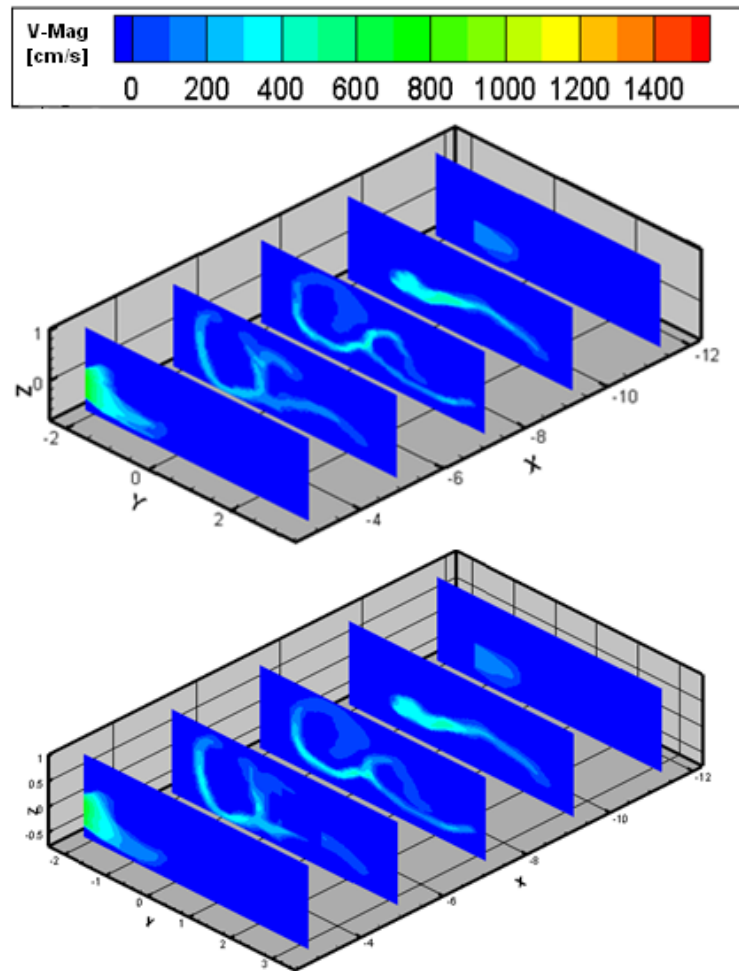
Figure 70: Velocity magnitude contours for the normal nasal cavity (Top) and the blocked cavity with enlarged middle turbinate (Bottom) at the inspiratory flow rate of 200 *ml/s*, showing a small reduction in flow in through the upper airway after adding the blockage.
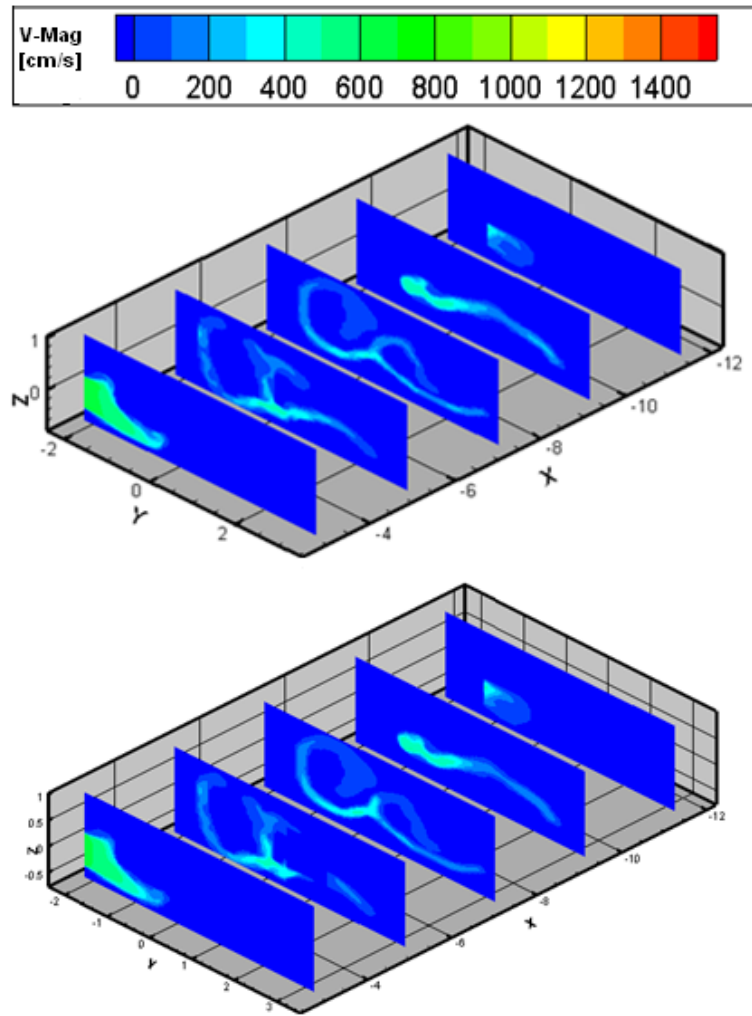
Figure 71: Velocity magnitude contours for the normal nasal cavity (Top) and the blocked cavity (Bottom) with enlarged middle turbinates at the expiratory flow rate of -200 *ml/s*, showing a small reduction in flow in through the upper airway after adding the blockage.
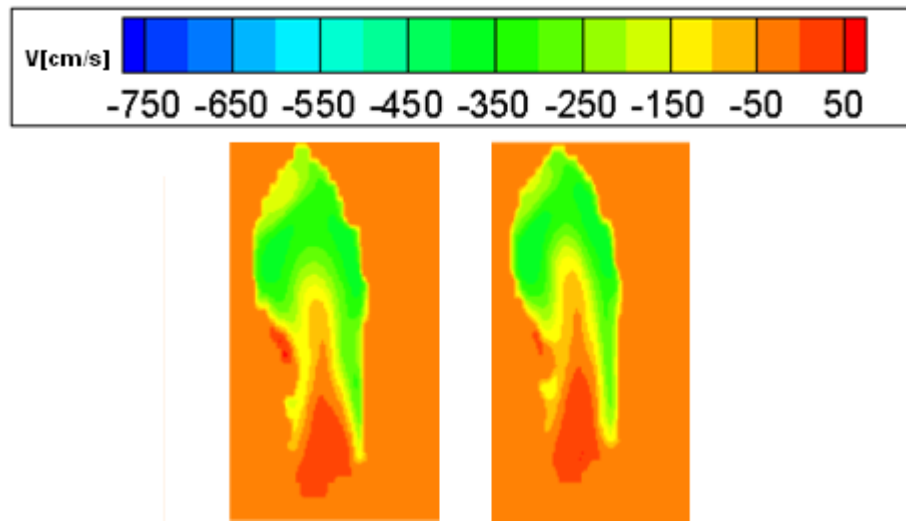
Figure 72: Normal velocity contours at the nostril, for the normal nasal cavity (Left) and the blocked cavity (Right) at the expiratory flow rate of -200 *ml/s*, showing a slightly more extended region of peak velocity for the blocked cavity.

The inspiratory and expiratory peak velocity magnitudes, along the X-axis are plotted and compared for both normal and blocked cavities in Figure 73 and Figure 74 respectively. The inspiratory airflow enters the blocked cavity at a lower speed than the air flow entering the normal nasal cavity. An increase in peak velocity magnitude is observed close to the location of blockage and it is maintained throughout the most turbinated region. At the posterior section the peak velocities become quite similar for both cavities. In the expiratory phase, the airflow enters the blocked nose via the nasopharynx at a lower velocity than for the normal nasal cavity and continues in the same manner until close to the location of blockage. The peak velocities are then hold higher values throughout the entire main nasal airway. Close to the nasal vestibule the peak velocities, once more reduce to lower values than those observed for the normal nasal cavity.
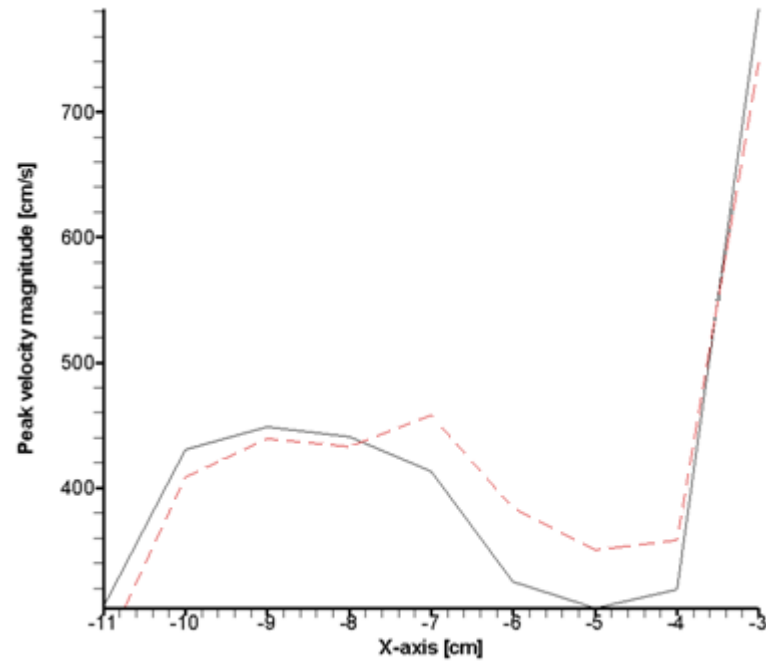
Figure 73: Peak velocity magnitude at different slides on the X-axis for the normal nasal cavity (Black) and the blocked cavity (Red: dashed) at the influx rate of 200 *ml/s*.
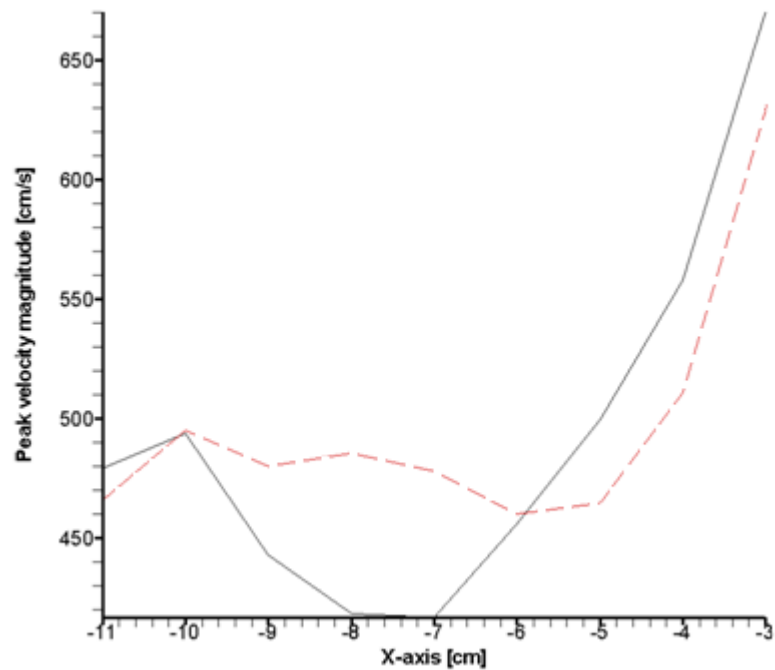
Figure 74: Peak velocity magnitude at different slides on the X-axis for the normal nasal cavity (Black) and the blocked cavity (Red: dashed) at expiratory flow rate of -200 *ml/s*.

6.3.2 Transnasal Pressure Difference and the Nasal Resistance for the Cavity with an Enlarged Middle Turbinate

Studying Table 11 reveals that the hypertrophy of the middle turbinate, creating a blockage in the posterior region is followed by a reduction in transnasal pressure, nasal resistance and the turbulent kinetic energy when compared to the normal nasal cavity in the inspiratory phase. These reductions occur due to reduction in the velocity magnitudes in the anterior region (Figure 73) of the nasal cavity after adding the blockage. Lower flow velocities at the nasal valve region, cause the airflow to experience less nasal resistance and reduces the promotion of turbulence supporting the previous results for other blockages. Furthermore blockage of the middle meatus which in a normal nasal cavity offers a narrow passageway and allows only for a small portion of inspiratory air (Figure 70) can reduce the transnasal pressure. This is expected since the middle meatus primary function is to provide drainage for the sinus secretion.

Increasing the inspiratory volume flow rate (Table 12), is followed by an increase in turbulent kinetic energy k from the inflow value for the blocked cavity as a result of increased velocities at the nasal valve region. This increase however is much smaller than the increase in the turbulent energy for the normal nasal cavity.

Table 11: Turbulent kinetic energy, transnasal pressure and the nasal resistance values for the normal cavity and the cavity with enlarged middle turbinate at the inspiratory rate of 200 *ml/s*.

Cavity at 200 *ml/s*	$\Delta k \dfrac{cm^2}{s^2}$	$Pd[Pa]$	$NR[\dfrac{Pa.s}{ml}]$
Normal	+1.9%	54.36	0.27
Blocked	-0.2%	53.46	0.26

Table 12: Turbulent kinetic energy, transnasal pressure and the nasal resistance values for the normal nasal cavity and the cavity with enlarged middle turbinate at the inspiratory rate of 300 *ml/s*.

Cavity at 300 *ml/s*	$\Delta k \dfrac{cm^2}{s^2}$	$Pd[Pa]$	$NR[\dfrac{Pa.s}{ml}]$
Normal	+8.7%	119.85	0.39
Blocked	+2.4%	117.71	0.39

For the expiratory flow rate of -200 *ml/s* (Table 13), introducing the blockage is accompanied by a small increase in both the transnasal pressure and the nasal resistance. The turbulent kinetic energy however decreases by 7% from the initial value due to the reduction in flow velocities at the posterior region after adding the blockage (Figure 74). As the expiratory flow rate increases, a further increase in the transnasal pressure, nasal resistance and Δk is observed for both cavities as expected.

Table 13: Turbulent kinetic energy, transnasal pressure and nasal resistance values in expiration for normal nasal cavity and cavity with enlarged middle turbinate for flow rate of -200 *ml/s*.

Cavity at -200 *ml/s*	$\dfrac{cm^2}{s^2}\Delta k$	$Pd[\,Pa\,]$	$NR[\dfrac{Pa.s}{ml}]$
Normal	-0.2%	18.001	0.090
Blocked	-7.0%	19.67	0.098

Table 14: Turbulent kinetic energy, transnasal pressure and nasal resistance values in expiration for normal nasal cavity and cavity with enlarged middle turbinate for flow rate of -300 *ml/s*.

Cavity at -300 *ml/s*	$\dfrac{cm^2}{s^2}\Delta k$	$Pd[\,Pa\,]$	$NR[\dfrac{Pa.s}{ml}]$
Normal	+3.9%	38.69	0.12
Blocked	-2.8%	42.12	0.14

6.3.3 External Flow Field

Figure 75 reveals different external flow fields, despite the similarities observed for the internal nasal airflow fields between the normal and the obstructed cavity. At the exit to the nostril, the region of high velocity magnitudes is larger for the blocked cavity, forming a thicker flow stream which is also more extended. The coronal velocity contours shown in Figure 76 also confirms the unique characteristic of each flow fields. For the blocked nose the flow is more deflected towards one side forming a different profile, to the horse shoe shape profile of the normal nasal cavity.
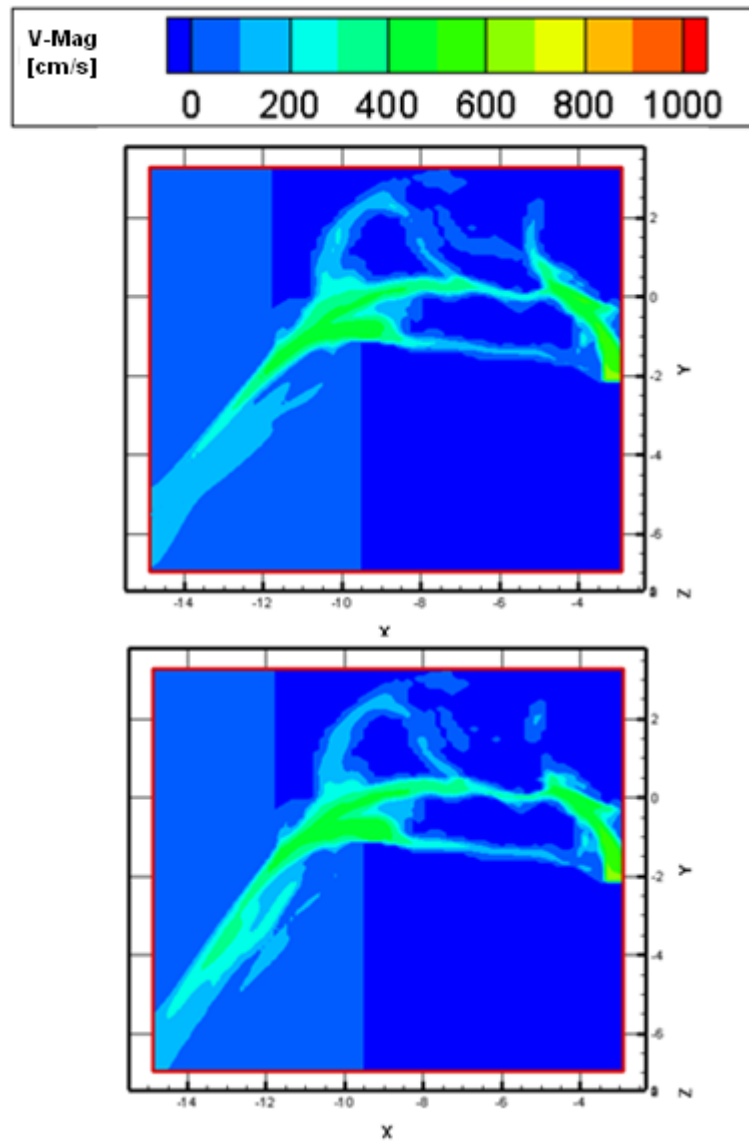
Figure 75: The expiratory internal and external nasal airflows for the normal nasal cavity (Top) and the blocked cavity as a result of enlarged middle turbinated (Bottom) at flow rate of -200 *ml/s*. Addition of blockage is followed by an increase in the external airflow thickness.
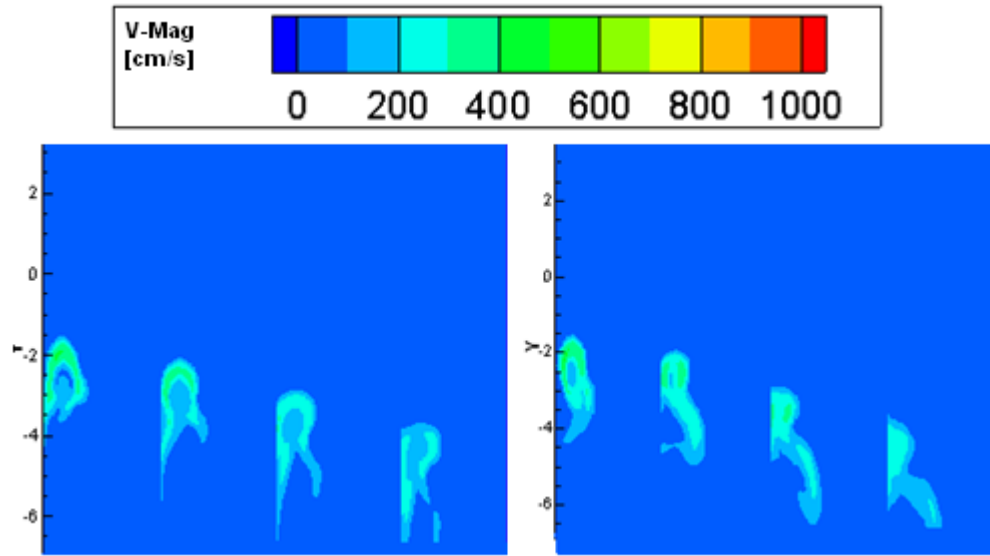
Figure 76: Velocity magnitude contours of the external nasal flow (in coronal planes on the X-axis: -12, -12.66,-13.33 and -14 respectively) for the normal nasal cavity (Right) and a cavity with enlarged middle turbinate (Left) at the expiratory rate of -200 *ml/s*.

6.4   Nasal Polyps

Nasal polyps are formed as the epithelial burst, followed by protrusion of the lamina propria forming bags of pale oedematous tissue that over time become fleshy and reddened [113] . They are most likely to appear from the anterior ethmoid sinuses through the middle meatus into the nasal cavity [114]. A nasal cavity with a nasal polyp is simulated by blocking the superior region of the main nasal airway shown in Figure 77.
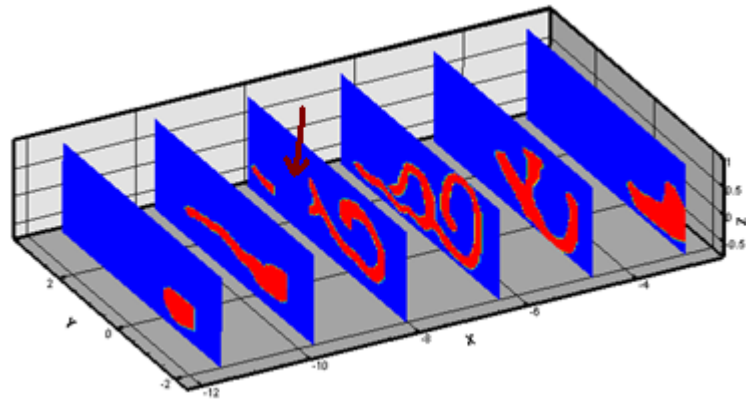
Figure 77: The location of blockage shown by the red arrow, due to a nasal polyp at the superior region of the turbinated area. For locations of nostril and nasopharynx refer to Figure 5.

6.4.1 Influence of the Nasal Polyps on the Respiratory Flow Field

The inspiratory velocity contours (Figure 78) for both normal and the blocked cavities are quite similar. Despite the location of the blockage which is at the superior region, there is no flow reduction in the olfaction. This suggests that the normal velocity component has a significant role in directing the flow from other airways to the olfactory region.
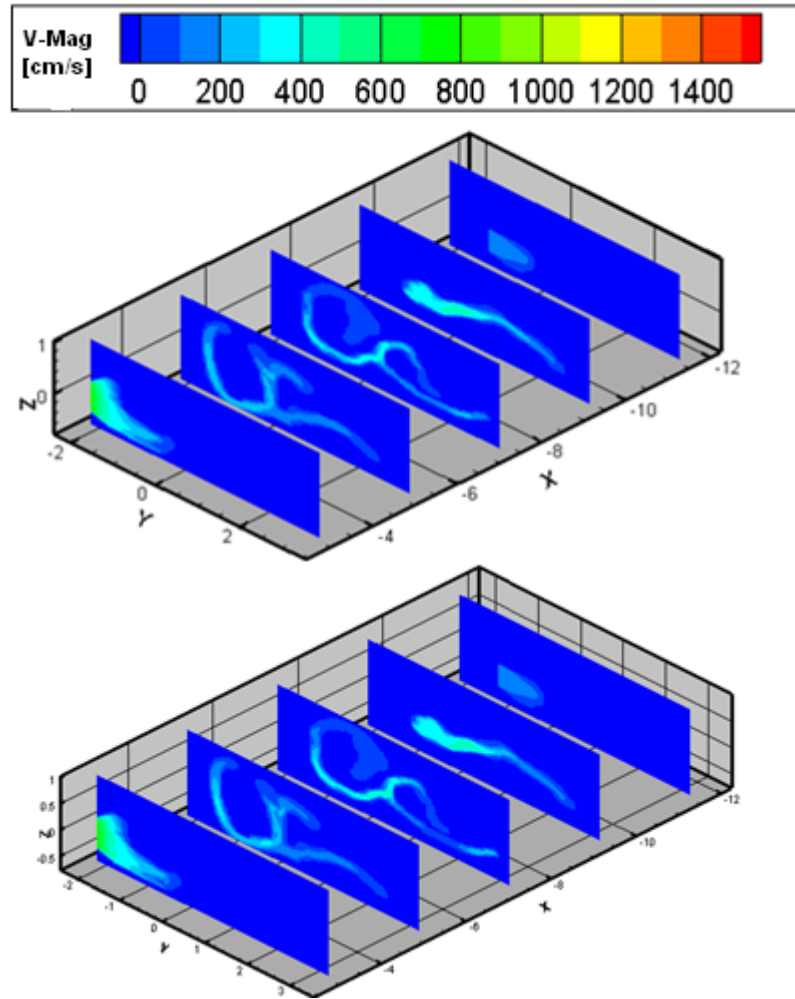
Figure 78: Velocity magnitude contours for the normal (Top) and blocked cavity due to the nasal polyps (Bottom) at the inspiration flow rate of 200 *ml/s*.

Comparing the peak velocity magnitudes for both cavities in Figure 79, shows similar profiles. For the blocked cavity, slightly higher velocities are observed around the location of blockage and throughout the main turbinated region. Velocity magnitudes are quite similar at the anterior and posterior regions.
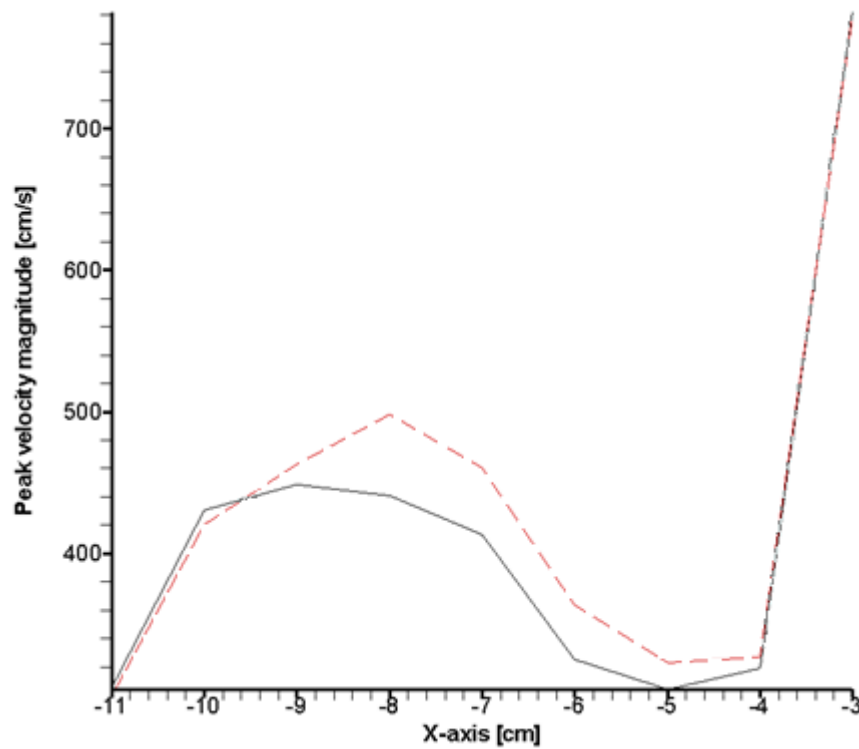
Figure 79: Peak velocity magnitudes at the inspiratory flow rate of 200 *ml/s* for the normal nasal cavity (Black) and the blocked cavity due to nasal polyp (Red: dashed). The peak velocities are higher for the blocked cavity at the location of blockage and throughout the main nasal airway.

Similar to the inspiratory phase there is no significant difference between the airflow fields of the cavities in expiration (Figure 80). The peak velocity magnitudes, (Figure 81) show similar velocities from the nasopharynx up to the location of the blockage where an increase in the peak velocity is observed for the blocked nose which continues up to the nostril. This higher velocity magnitude at the nostril can also be seen from the normal velocity contour shown in Figure 82, specifically at the tip of the nostril although the flow fields are quite similar.
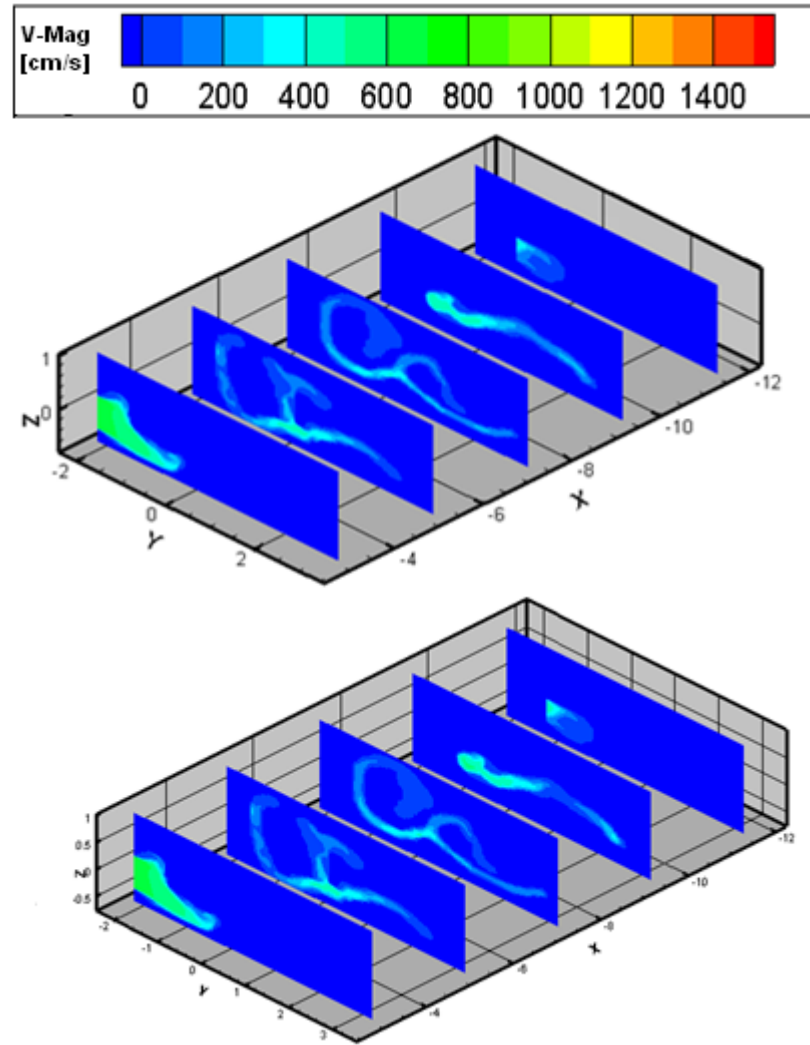
Figure 80: Velocity magnitude contours for the normal cavity (Top) and the blocked cavity due to the nasal polyps (Bottom) at the expiratory flow rate of -200 *ml/s*.
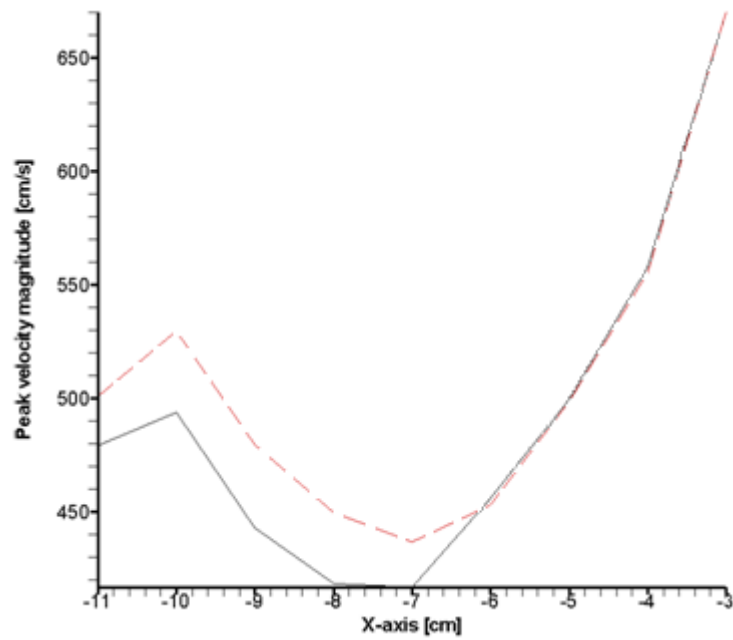
Figure 81: Peak velocity magnitudes along the axial length of the normal nasal cavity (Black) and the blocked cavity (Red: dashed) at the expiratory rate of -200 *ml/s*, showing higher peak velocities at the anterior region for the blocked cavity.
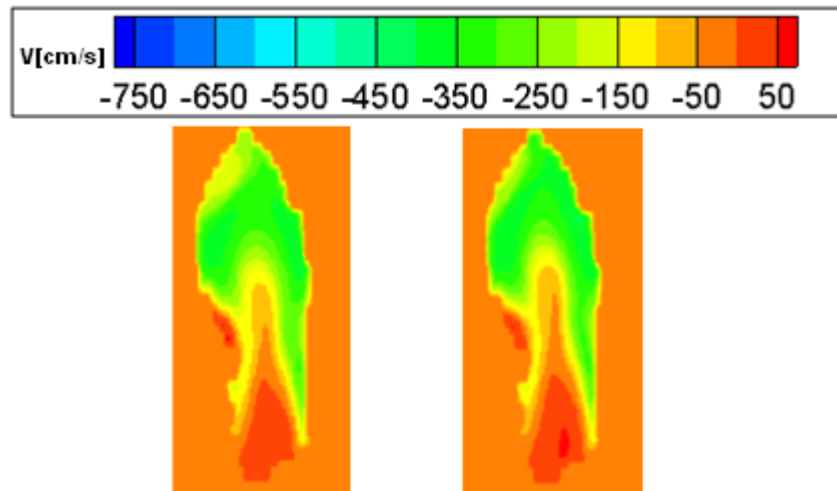
Figure 82: Normal velocity contour at the expiratory rate of -200 *ml/s* for normal nasal cavity (Left) and the blocked cavity due to the nasal polyp (Right). The region of peak velocity magnitude is more extended at the tip of the nostril for the blocked cavity.

6.4.2 Transnasal Pressure, Nasal Resistance & Turbulent Kinetic Energy for the Cavity with Nasal Polyps

Looking at Table 15, a small increase in the transnasal pressure can be observed as a result of blockage for the inspiratory rate of 200 *ml/s*. However since the nasal polyp only blocks a small region of the cavity within the main nasal airway there is no further increase in the nasal resistance. Both the turbulent kinetic energy Δk and the turbulent intensity I values stay the same as expected since the velocity magnitudes at the anterior region were quite similar for both cavities (Figure 79). This suggests that the blockage of the superior region has negligible influence on turbulence production. Similar trend is also observed for a higher inspiratory flow rate of 300 *ml/s* as shown in Table 16.

Table 15: Turbulent kinetic energy, transnasal pressure and the nasal resistance values for the normal and the blocked cavities, at the inspiratory flux of 200 *ml/s*.

Cavity at 200 *ml/s*	$\Delta k \frac{cm^2}{s^2}$	$Pd[Pa]$	$NR[\frac{Pa.s}{ml}]$
Normal	+1.9%	54.36	0.27
Blocked	+1.9%	55.70	0.27

Table 16: Turbulent kinetic energy, transnasal pressure and the nasal resistance values for the normal and the blocked cavities for the inspiratory flow rate of 300 *ml/s*.

Cavity at 300 *ml/s*	$\Delta k \frac{cm^2}{s}$	$Pd[Pa]$	$NR[\frac{Pa.s}{ml}]$
Normal	+8.7%	119.85	0.39
Blocked	+8.9%	122.80	0.4

For the expiratory flow rate of -200 *ml/s* the addition of nasal polyp causes an increase in both transnasal pressure and the nasal resistance (Table 17). This increase is expected as a result of the increase in the velocity magnitude in the anterior region which is a critical section for contributing to the nasal resistance value. The addition of blockage however shows no influence on the turbulent kinetic energy. This is also expected since the velocity profiles are quite similar at the posterior region close to the nasopharynx. For the higher expiratory flow rate of -300 *ml/s* (Table 18) and hence higher velocities within the normal cavity, an increase in the transnasal pressure, nasal resistance and *k* can be observed.

Table 17: Values of turbulent kinetic energy, transnasal pressure and the nasal resistance for the normal nasal cavity and the cavity with nasal polyp at the expiratory flow rate of -200 *ml/s*.

Cavity at -200 *ml/s*	$\Delta k \frac{cm^2}{s^2}$	$Pd[Pa]$	$NR[\frac{Pa.s}{ml}]$
Normal	-0.2%	18.001	0.09
Blocked	-0.2%	20.25	0.10

Table 18: Turbulent kinetic energy, transnasal pressure and the nasal resistance for the
normal cavity and the blocked cavity, at the expiratory rate of -300 *ml/s*.

Cavity at -300 *ml/s*	$\Delta k \frac{cm^2}{s^2}$	$Pd[Pa]$	$NR[\frac{Pa.s}{ml}]$
Normal	+3.9%	38.69	0.12
Blocked	+3.9%	43.86	0.14

6.4.3 External Nasal Airflow for the Cavity with Nasal Polyp

The flow fields from the normal nasal cavity and the cavity with the nasal polyps including both internal and external flows are shown in Figure 83. Higher velocities are observed for the blocked cavity, resulting into a thicker airflow stream which extends further than the airflow from normal nasal cavity.

Figure 84 shows the external velocity magnitude contours on coronal slides along the X-axis. Higher velocity magnitudes for the blocked nose result into a fuller profile as compared to the normal nasal cavity. The two velocity profiles for both cavities become more distinctive as the distance increases from the nostril.
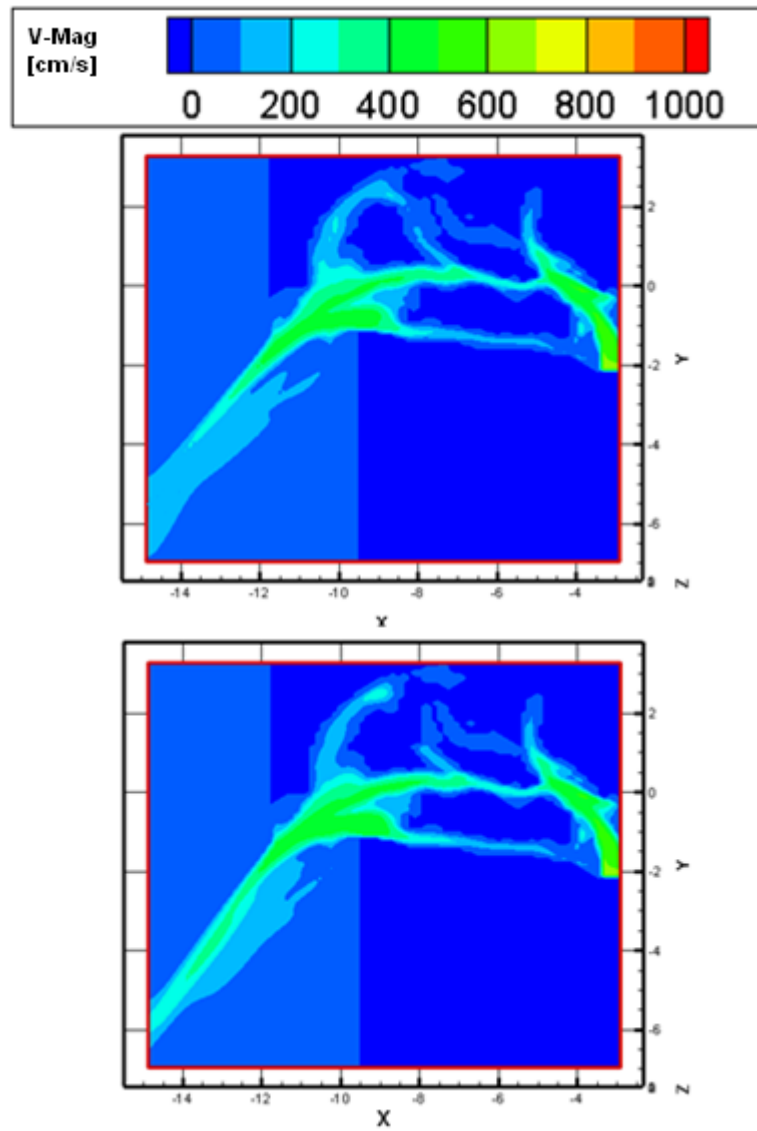
Figure 83: Internal and external nasal airflow fields for the normal nasal cavity (top) and the cavity with nasal polyp (Bottom) at expiratory flow rate of -200 *ml/s* showing a thicker external flow stream for the blocked cavity.
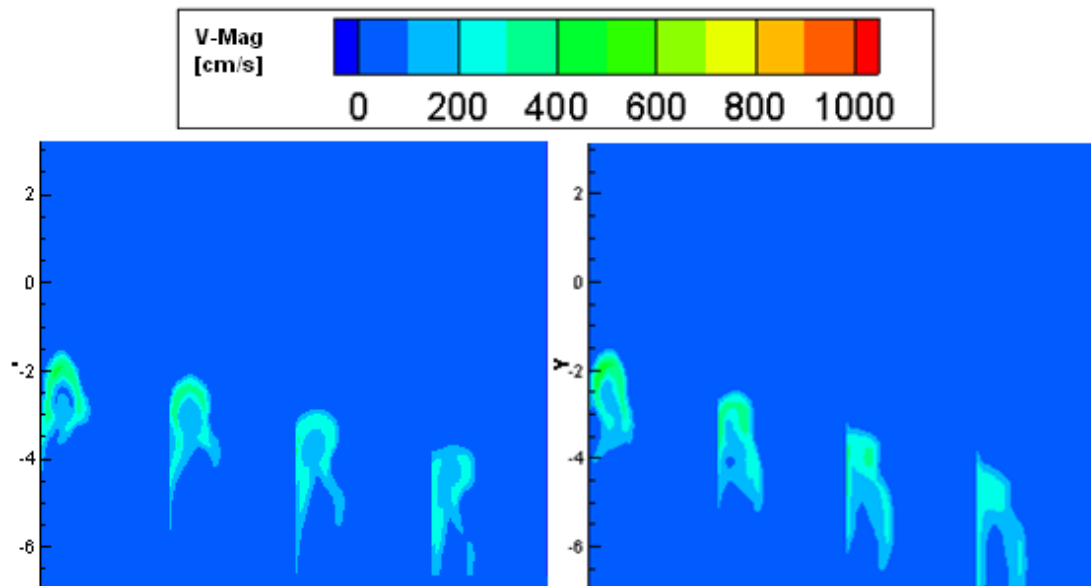
Figure 84: Coronal velocity magnitude at different slides on the X-axis from left to right at (-12, -12.66,-13.33 and -14) external to the nasal cavity at the expiratory rate of -200 *ml/s*. the contours show the influence of the blockage on the external nasal airflow as the velocity profile differ at the identical cross coronal sections.

6.5 Summary

This chapter investigated the influence of the nasal blockages on both the internal and the external nasal airflows. Initially the nasal septum was extended to block the anterior and the posterior regions of the nasal cavity separately. Both blockages showed significant influence on the nasal airflow field by increasing the velocity magnitude where the obstructions narrowed the nasal airways as well as reducing the flow through the olfactory region and hence the possibility of losing the sense of smell. Both the anterior and posterior septal deviations caused an increase in the nasal resistance and the turbulent kinetic energy. However these increases were much higher for the cavity with the anterior blockage suggesting that the anterior

197

region of the nasal cavity is a critical area for the flow field which exhibit a significant influence on turbulence promotion.

The inferior turbinate was enlarged at two separate occasions. First the blockage was arranged to obstruct parts of the lower airway and meatus in the anterior region. In the second case the hypertrophy blocked the entire lower airway and meatus at the posterior section. Both blocked cavities were shown to influence the flow field by shifting the preferred path of the flow from the lower half to the upper half of the nasal cavity. There was no change in the olfactory flow flux as a result of blockage. The highest velocity magnitude was observed for the cavity with the anterior blockage despite having a lower degree of blockage. This confirmed the significant of the anterior region. The values of transnasal pressure and the nasal resistance were increased after introducing the blockages. Higher increases were observed for the cavity with the posterior blockage where the degree of blockage was higher too. The turbulent kinetic energies were found to be lower than in the normal nasal cavity, due to flow velocity reduction in the anterior region.

Two other blockages were considered by enlarging the middle turbinate and introducing a nasal polyps to partially block the middle meatus and the superior airway respectively. These two blockages showed smaller influences on the internal nasal airflows. This suggests the anterior region and the lower half of the nasal cavity are the most influential region within the nasal cavity. This is expected since in a normal nasal cavity the majority of the flow was shown to pass through the lower half. Despite the small influence of some of the blockage within the cavity, for all cases studies in this chapter the resultant internal nasal airflows were shown to be

different from the normal nasal cavity and different with respect to each other, confirming the results from the experimental study by Grutzenmac et al. [115].

Investigating the external nasal airflow revealed promising results. It was shown that in addition to the external velocity profile which was unique for each nasal cavity considered after varying the internal geometry, the external flow angle and it thickness were also varied with respect to the degree and the location of the blockage. These changes in the external nasal airflow field, even for cavities with similar expiratory flow patterns at the nostril cross section, (cavity with enlarged middle turbinate and cavity with the nasal polyps) were significant enough to be recognised. This is quite promising since the major obstacle in using the airflow dynamics for diagnosis of the nasal blockage is, the measurements of the internal nasal airflow field due to the small size of the cavity. The uniqueness of the external airflow field for all the nasal cavities studying in this chapter suggests that the measurements of the external nasal airflow can be just as utile as of the internal flow field and much easier to be measured.

7. Chapter 7

Experimental Results & Comparison with Computational Data

Experimental studies were carried out using the Schlieren optical technique on a human subject and a PIV system (Particle Image Velocimetry) using a 2.54:1 scaled silicon model of the nasal cavity. These data were then compared to the computational results for validation when applicable and for further analysis.

For the Schlieren set up a single extended light source was used since it was shown in chapter 3 to give the sharpest image. The air was also replaced with helium gas for increasing the visibility of Schlieren images, since the flow fields using helium gas and the air were shown to be quite similar. The external airflow field of a steady exhale was then captured by asking the human subject to blow the air out for few seconds at a steady normal breathing rate which is identical to the computational flow condition.

Using the 2-D PIV technique, the external flow field outside the nostril was measured for the scaled model of the nasal cavity. The air entered the cavity via nasopharynx to simulate expiration. Fine particles of olive oil were introduced into the airflow for the transparency within the laser sheet. The flow rate was adjusted so that the flow field can be captured at different influx rates to allow comparison to the computational data.

7.1 Schlieren External Flow Images & Comparison with the Computational External Flow field

The nasal airflow flow pattern of human subjects was captured while exhaling helium gas at a steady breathing rate for a few seconds. Initially the flow field was captured as the flow was exhaled from both nostrils using 8 subjects at a normal breathing rate. These images were then compared to the subjective score of their nasal patency. Using one subject only the external nasal airflow field was also captured for several times from one and both cavities.

The quality of the recorded images from the first set of experiment, were found quite poor. This was due to the un-precise arrangement of parts while setting up the Schlieren system, since it was the first attempt as well as the dislocation of the folding mirror as result of constant vibration in the laboratory environment which decreased the sensitivity of the system. Also due to a connection problem between the camera and the computer, resulting images were in black and white. Despite the poor quality of these images, some results were drawn by comparing the external flow pattern of each subject to their subjective patency scores. Out of the eight images taken of the external flow field, only five were visible. These five images belonged to the subjects with the patency scores of 1 to 3 indicating clear nasal airways. Other three images that show no clear external flow patterns had the patency scores of 4 to 5 which describes a congested nasal airway. This suggests that the amount of airflow through the nose of subjects with high patency scores may have been reduced to the nasal blockage.

For the second sets of experiment, the Schlieren system was improved and the arrangement of the mirror were continuously checked and corrected. The images taken from flow patterns were similar in each test. The images of the external airflow from one and both nostrils are shown in Figure 85. Comparison reveals fairly similar patterns as both flows travel for a short distance before they disappear on the Schlieren image, as their velocity decreases and their temperature reaches the surrounding environmental temperature. A small difference between the two external flow angles can be observed. The measured flow angles are 60 and 55 degrees from both nostril and one nostril respectively. This is expected due to having higher velocities at the exit from both nostrils, and confirms the computational results in the previous chapter, where higher velocities at the anterior region due to blockages were accompanied by an increase airflow angle. The thickness of the external nasal airflow from one nasal cavity is also greater that the flow leaving both nostrils. This also confirms the results in previous chapter. Finally the flow pattern is more visible when both nostrils are used, suggesting the influence of the neighboring air flows on each other and increased mixing.
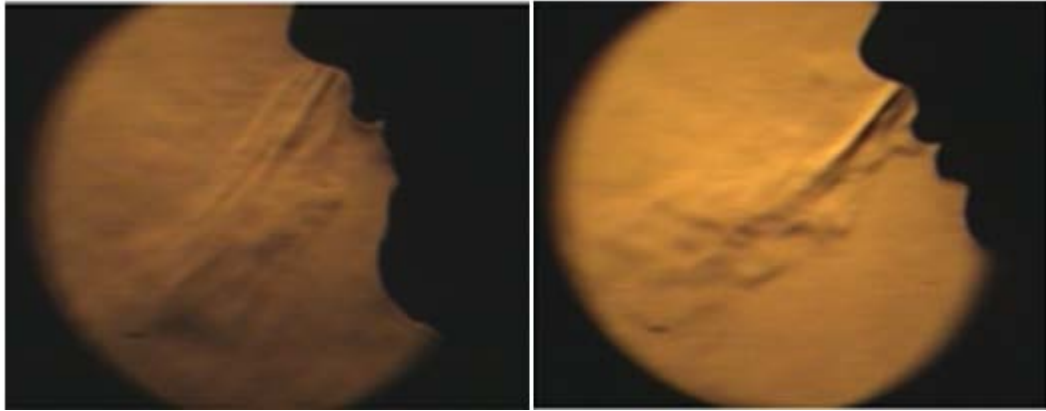
Figure 85: Captured external airflow pattern of one nostril (Left) and both nostrils (Right) at a steady expiration. The external nasal airflow from one cavity is thicker with a lower external flow angle.

Comparison between the Schlieren images and the computational data for the expiratory flow rate of -200 *ml/s* (Figure 86) shows similar flow characteristic. Similar to the Schlieren flow pattern, the computational nasal air flow leaves the cavity with its highest velocity located towards the tip of the nostril and there is a reduction in flow velocity as the flow progresses. The computational flow angle measured is also close to 60 degrees which is similar to the Schlieren external flow angle. The small difference between the external flow angles is the result of having different volume flow rates. More detailed and quantitative comparison is not valid for these data since the nasal cavities considered for Schlieren images and the computational calculations are not the same. Furthermore the Schlieren system is also only a qualitative technique.
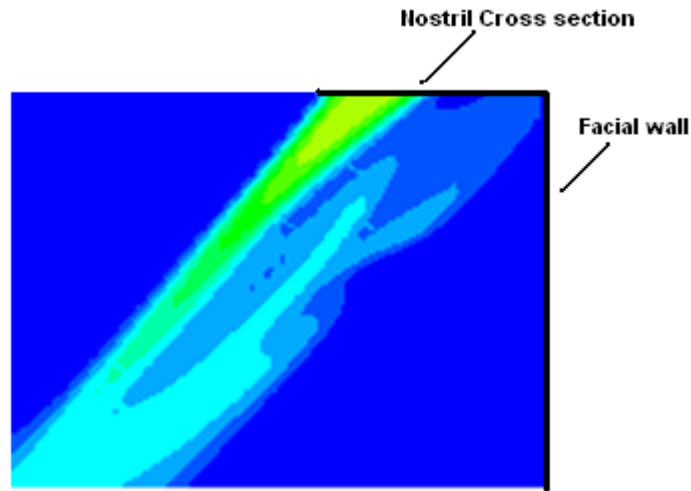
Figure 86: External computational airflow pattern for the expiratory flow rate of -200 *ml/s* in the sagittal plane, showing similar external flow angle and flow pattern to the Schlieren images.

The similarities between the experimental and the computational flow fields suggest that an optical technique such as Schlieren, may be a useful tool for clinical observation in assessment of the nasal blockage since in the previous chapter it was shown that the external nasal flow can be used for diagnosis purposes.

7.2 PIV Experiments & Comparison with the Computational Data

The PIV measurements are carried out using a 2.54:1 silicon model of the nasal cavity (Figure 15). The air from an air cylinder is adjusted to a suitable flow rate via a flow meter attached to the set up. The olive oil particles are then introduced to the air before it reaches the nasopharynx using a T junction. The airflow through the nasal cavity is designed to be kinematically similar to the computational data by

matching the numerical values of the relevant dimensionless numbers that characterized the flow. Since the experiments are carried out for the airflow at a steady exhale, only the Reynolds number ($Re = \dfrac{\bar{u}d}{\nu}$) needs to be considered, where $\bar{u}$ is the mean local velocity, d is the local diameter and ν is the kinematic viscosity of air. Since the volume flow rate, $\dot{q}$ through the nose is proportional to $\bar{u}d^{2}$, it follows that $\dot{q}_{model} = 2.54\,\dot{q}_{computational}$ when Re is matched in both systems [46].

An aluminium sheet is cut and added to the experimental model, to represent the face (Figure 49) in the computational data. Since the CFD code measures the flow field through one nasal cavity only, another wall is added at the septum side acting as a wall of symmetry. The entire model is then painted in matt black to avoid laser reflection during the experiments.

The PIV images are captured at three different planes of coronal, sagittal and parallel to the nostril plane. For the coronal plane, the nostril is divided into five equal sections for four planes and the sagittal plane cuts through the nostril medially. Three flow rates of 130, 380 and 635 *ml/s* which correspond to 50, 150 and 250 *ml/s* in the computational studies are considered. The experimental results are compared to the computational flow fields calculated on the identical plane and for the same influx flow rate.

7.2.1 Nasal Flow Field in Coronal Plane

The external experimental flow fields taken at various coronal planes are compared to the computational flow fields at the identical planes for the same influx flow rate. Using the expiratory flow rate of -250 *ml/s* the flow fields are compared at the coronal planes shown in Figure 87.
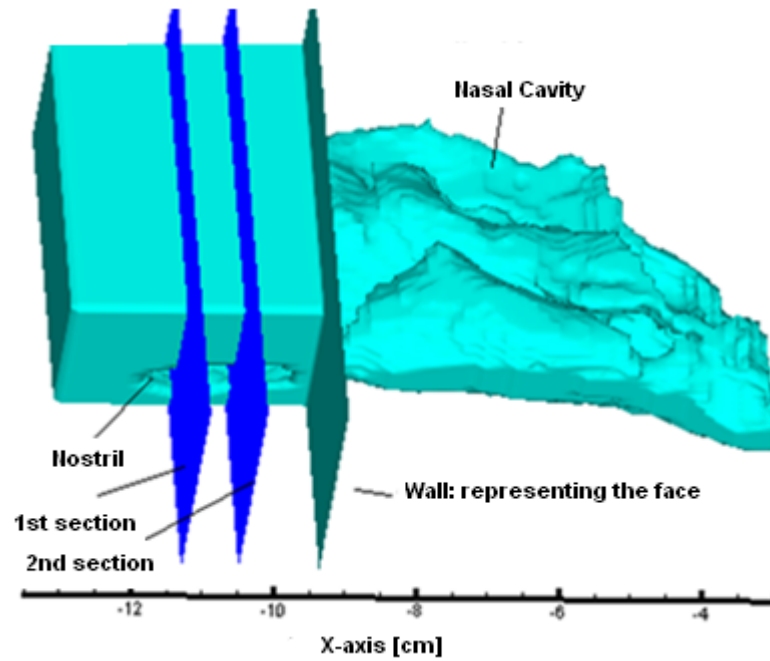
Figure 87: Coronal slices external to the nasal cavity located at the -11.2 and -10.4 on the x-axis, identical to the first and the second slides in the PIV experiments.

Figure 88 shows the flow fields at the first cross sectional area, starting at the exit of the nostril. Both images show the same area. According to the contours, the computational velocities are higher than the experimental velocities as expected since based on the kinematical similarity, the velocities should follow the

$$U_{exp} = \frac{U_{comp}}{2.54}$$ relation. Comparing the peak computational and the experimental

velocities of 553 *cm/s* and 272 *cm/s* respectively, however shows that the experimental values is higher by about 20%. This can be explained as a result of having slightly different flow rates and geometries in the experimental and the computational experiments.

A small flow angle is observed in both flow fields shifting the nasal airflow towards the septum side (or the added experimental symmetry wall). This angle can be easily detected from the experimental data and it is more visible in the computational flow field at far field. This shift in flow pattern was previously observed and reported as a result of flow deflection from the middle airway towards the lower part of the nostril Figure 54. This small velocity component towards the septum is responsible for mixing of the airflows from each nasal cavity reported in section 7.1 for the Figure 85. Two regions of high velocity concentration are observed close to the nostril cross sectional area for the computational flow field marked by the red and black arrows. These two regions create a horse shoe shape by splitting the airflow stream into two branches. Similar regions can also be observed in the experimental data which are marked by arrows. However for the experimental flow field these high velocity concentrations are not high enough to split the airflow stream.
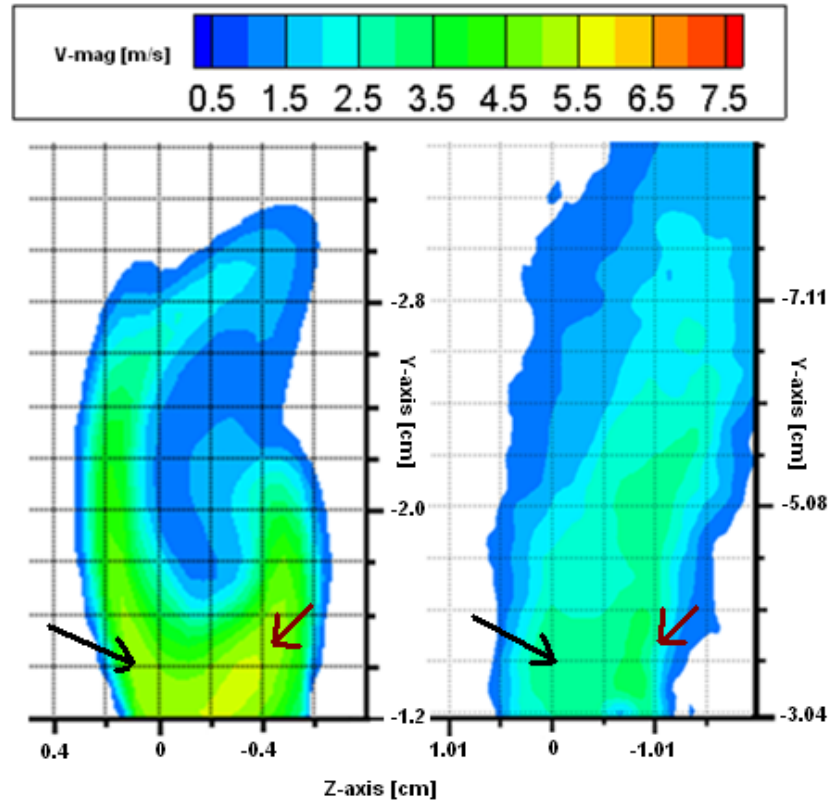
Figure 88: External flow field showing the velocity contours at the expiratory rate of -250 *ml/s* using computational data at a coronal slide on x=-11.2 (Right) and the PIV results on the 1st coronal cross section (Left) which is taken from the enlarged (2.54:1) nasal cavity model. Y-axis is located at the wall of symmetry (the wall separating the two nostrils). Both computational and the experimental fields show two regions of high velocity concentrations and a cross flow component towards the septum.

Figure 89 shows the non dimensional velocity profile along a plane parallel to the nostril cross sectional area in Figure 88 and separated by 0.05 cm towards the external field. Both graphs indicate two peak velocities. Although the peak computational velocities occur closer to the septum as compared to the experimental data but they are fairly close. The reduction in velocity magnitude between the two peak points is sharper in the experimental data and it is much more subtle in the computational field. The experimental velocity profile shows more gradual reduction from the highest velocities to the lowest whereas in the computational profile this

slope is greater. The areas between the two peak points underneath the graphs are quite similar in size suggesting that the regions of high velocities are distributed fairly equally.
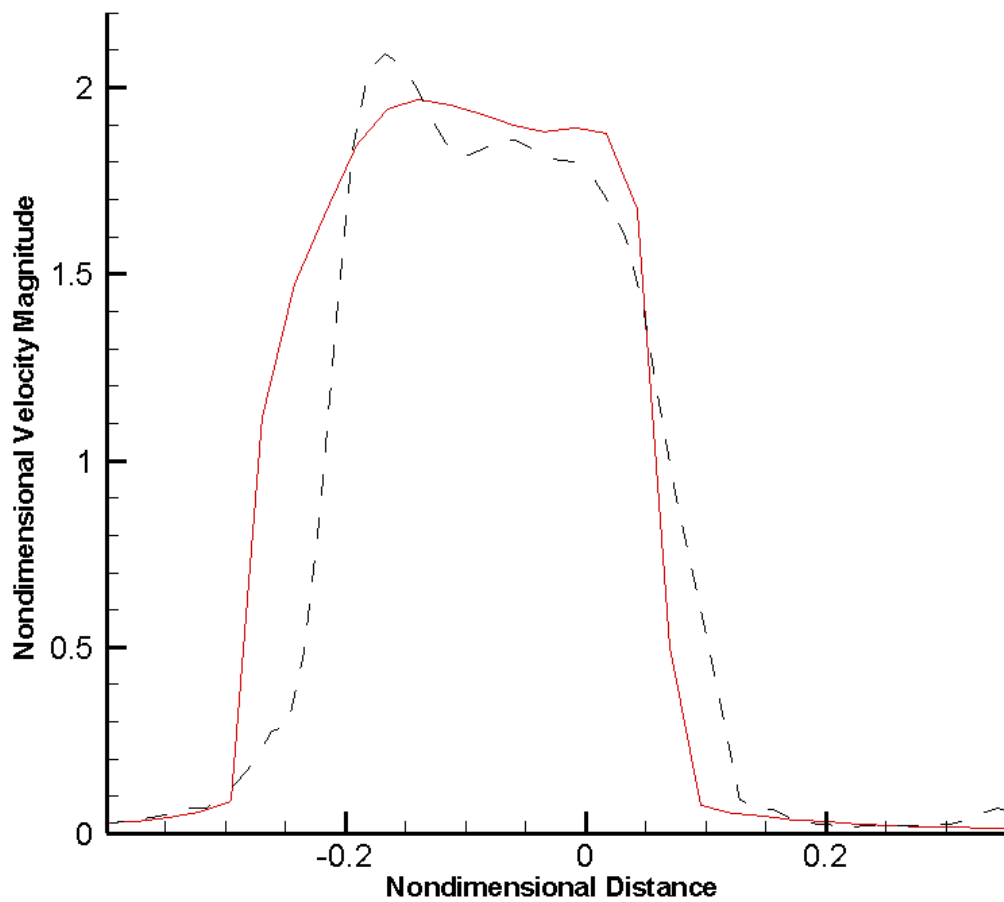
Figure 89: Non-dimensional external Velocity Magnitude versus non-dimensional distance for the experimental (back dotted line) and the computational (red solid line) data respectively (0.2, closest to the septum) taken at the expiratory rate of 250 *ml/s* parallel to the nostril cross sectional area and separated by 0.05 cm in Figure 88.
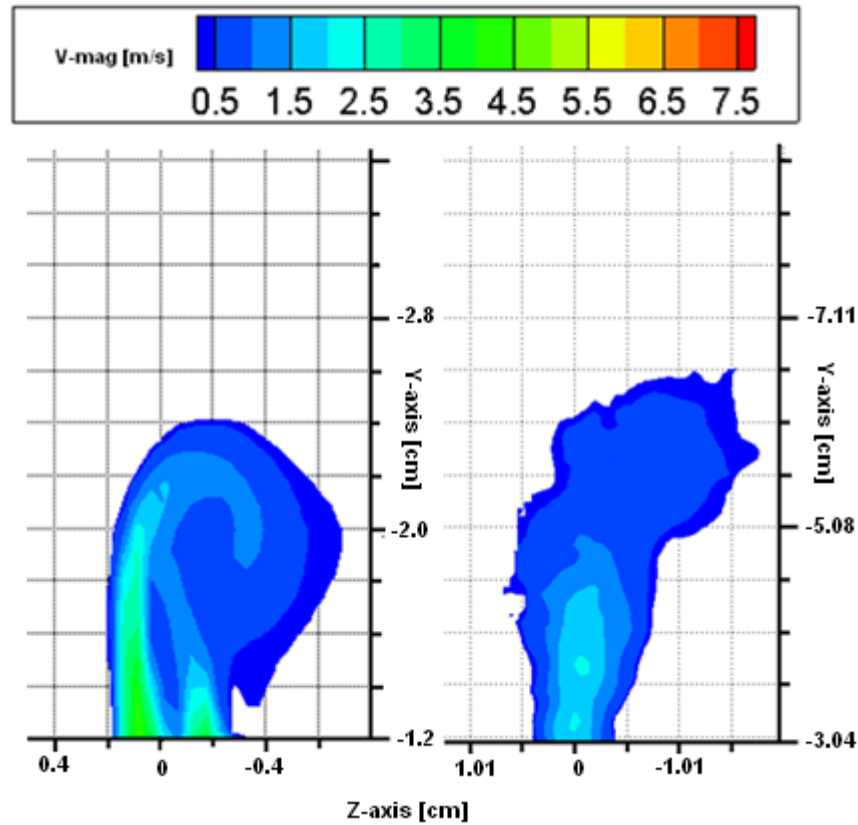
Figure 90: External velocity flow field at the expiratory rate of -250 *ml/s* using computational data at a coronal slide on x=-10.4 (Right) and the PIV data taken from the enlarged model (2.54:1) from the 3rd coronal section (Left). Y-axis is located at the wall of symmetry.

Similar results are also found for the expiratory external computational and the experimental flow fields at the second coronal plane. With the progression of flow, both fields are shifted towards the septum. Higher velocity magnitudes are observed in the computational data, with the peak computational and the experimental velocity magnitudes of 547.41 cm/s and 249 cm/s respectively close to the nostril. The experimental peak velocity magnitude still holds a higher value than the expected value by about 15%. This reduction (from 20% to 15%) from the first plane can be related to the geometrical variation between the two models. The computational flow

field is still divided into two streams close to the nostril, as a result of having two regions of high velocity concentrations, however this splitting is much less as compared to the first plane as the velocity is smaller. For the experimental data the highest velocities are along a single line. Looking at both images (Figure 88 & Figure 90) it can be observed that changes in the computational flow field in the axial direction occur much faster than in the experimental data, allowing the experimental flow field to extend longer than the CFD flow field. The abrupt changes in the computational data can be due to the artificially viscosity introduced in the CFD codes. The influence of the artificial viscosity will be studied in more details later in this chapter. The external computational and the experimental flow fields at the expiratory rate of 150 *ml/s* at a coronal plane located on X=-10 cm are compared in Figure 91. The peak computational and the experimental velocity magnitudes are 334 *cm/s* and 152 *cm/s* respectively located at the nostril.

Comparison between all data presented in this section, reveals as the flow moves further away from the tip of the nostril (First slice) towards the bottom of the nostril (Second slice), the flow velocities as well as the flow angle towards the septum decreases. This agrees with the Schlieren images (Figure 85) and the external computation flow patterns (Figure 50), as the highest velocities were also found close to the tip of the nostril.
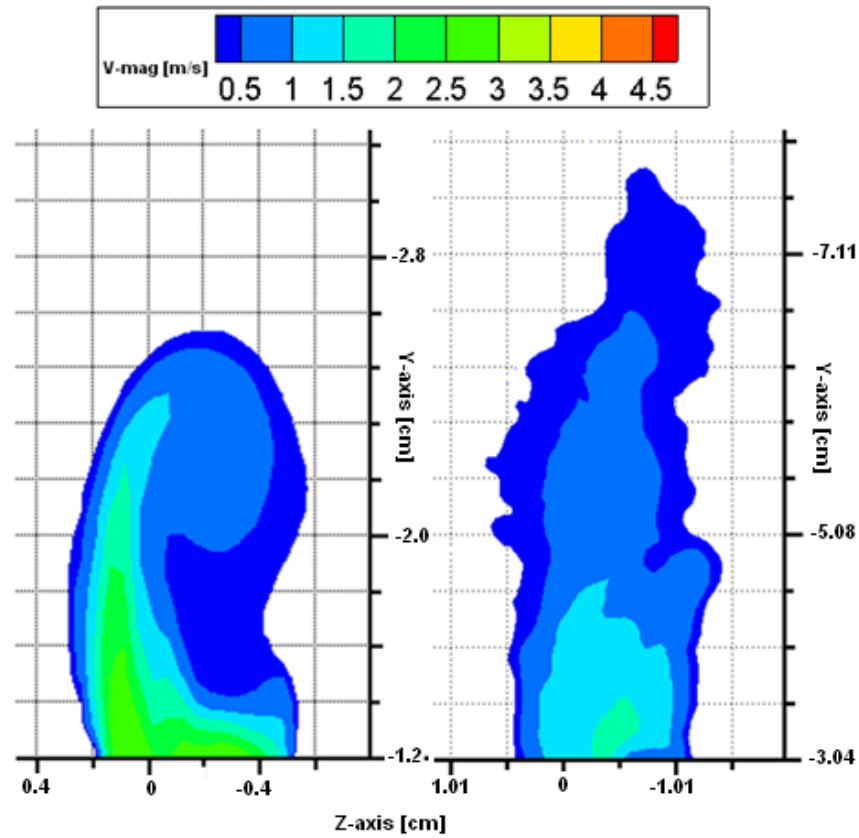
Figure 91: External velocity flow field at the expiratory rate of -150 *ml/s* using computational data at a slide on x=-10.0 (Right) and the PIV results from the 4th section (Left). Y-axis is located at the wall of symmetry.

7.2.2 Nasal Flow Field in Sagittal Plane

The experimental flow field in the sagittal plane is investigated by arranging the laser sheet arm in a position to cut through the mid section of the nostril. The identical computational slide is shown in Figure 92.

212

Sagittal slice: cutting through the mid section of the nostril
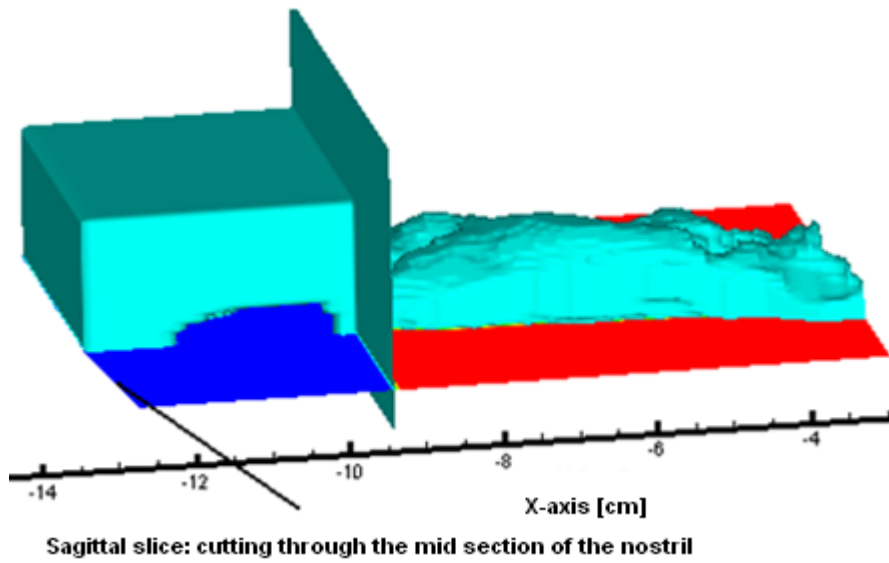
Figure 92: The sagittal slide cutting the nostril medially identical to the sagittal experimental slice.

Figure 93 shows the computational and the experimental external flow fields in the sagittal plane for the expiratory flow rate of -250 *ml/s*. The flow fields are similar with the highest velocities located close to the tip of the nostril for both images. The velocities are higher in CFD data with the computational and the experimental peak velocity magnitudes of 780 *cm/s* and 357*cm/s* respectively. There is an increase of 15% in the measured experimental peak velocity magnitude from the expected value.
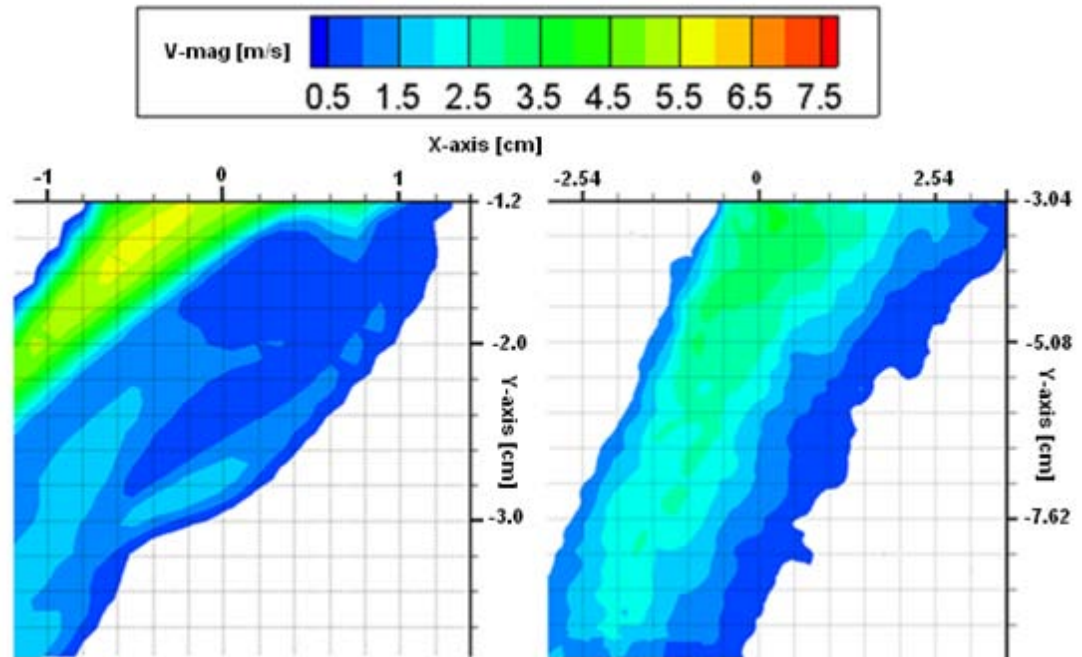
Figure 93: External flow field of the velocity contours levels in the sagittal plane at the expiratory flow rate of -250 *ml/s*, computational data (Right) and experimental flow field (Left). The tip of the nostril is located close to the X=-1, the bottom of the nostril is located close to the X=1. The highest velocities are located towards the tip of the nostril in both computational and the experimental flow fields.

The Non dimensional velocity profile is plotted in Figure 94, at the plane taken close to the nostril cross sectional area (at Y=-1.2). Despite the difference between the two graphs, there are several common features. Starting from the septum, the velocities gradually increase until they reach their highest values towards the tip of the nostril followed by a sharp reduction. The locations of peak velocities are quite close, with the CFD data slightly closer to the septum similar to the coronal profile. More oscillation is observed in the experimental data.
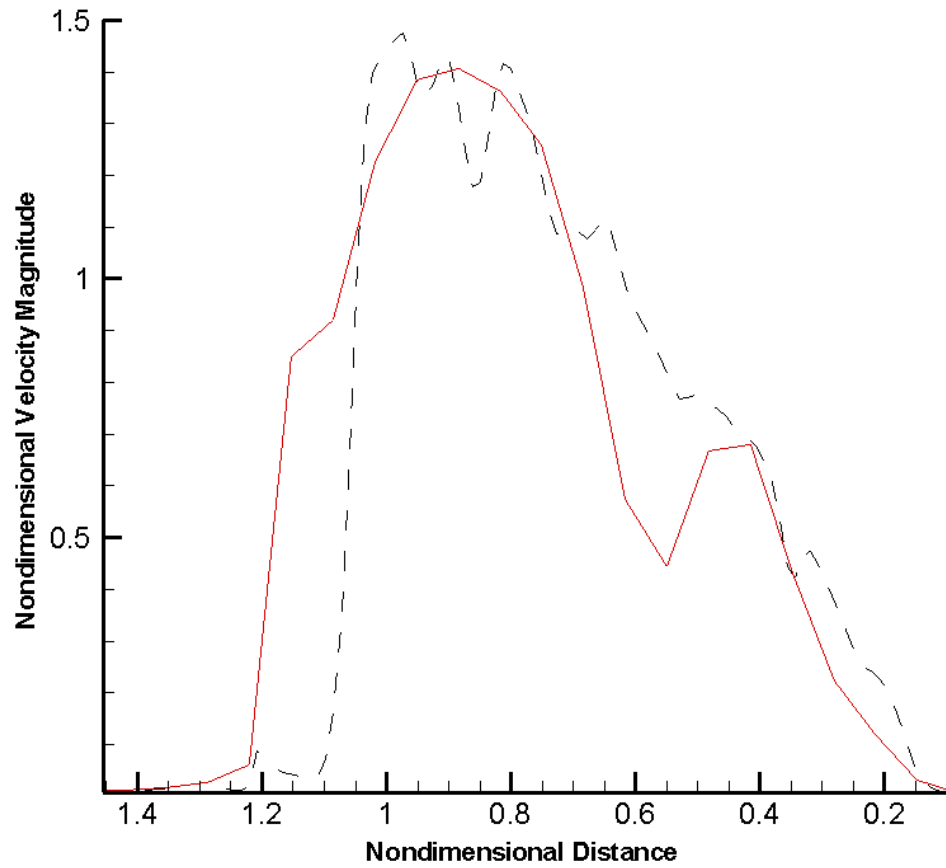
Figure 94: Non dimensional velocity magnitude versus non dimensional distance across an axial line at the nostril cross section (Y=-1.2) in Figure 93 taken from the sagittal plane, for the computational (red, Solid) and the experimental (black dotted line) expiratory flow rate of 250 *ml/s*, (0.2 is the closest to the septum). Both profile show a gradual increase in non-dimensional velocities form the septum side and same region of peak non-dimensional velocities.

7.2.3 Airflow Field at the Nostril

The experimental model is tilted so that the laser sheet is in the parallel and close to the nostril cross sectional area as shown in Figure 95.
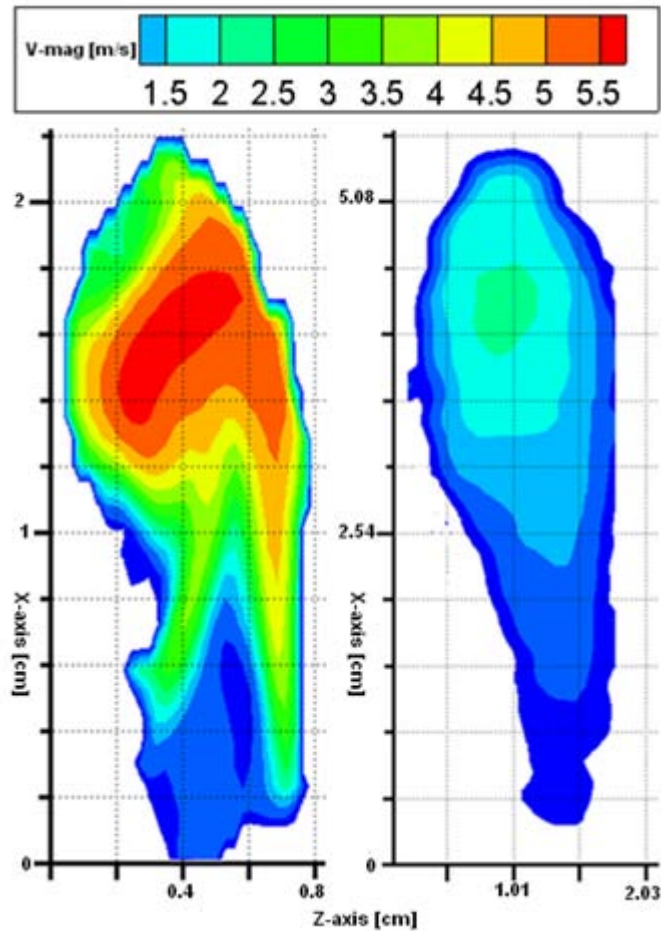
Figure 95: The computational velocity magnitude field (Left) and the experimental (Right) velocity magnitude flow field taken from the enlarged (2.54:1) nasal cavity model, at a plane located on the nostril cross section for the expiratory rate of -250 *ml/s*. Highest velocities are located towards the tip of the nostril in both data fields.

Comparing the two flow fields shows lower velocities in the experimental data. The computational and the experimental peak velocity magnitudes of 571 *cm/s* and 217 cm/s are located between the center and the tip of the nostril. Unlike the previous cases where the peak experimental velocity was found to be higher, in this case is smaller than the computational velocity by small amount. This is caused due to the difference between the slice locations in the computational and the experimental data. For the computational contours the data are taken exactly at the nostril cross

216

section, whereas for the experimental data, the laser sheet could not be arranged exactly on the nostril. The experimental data are therefore taken from a close parallel cross section to the nostril. This reduction in the experimental velocity is therefore caused as the flow slows down further away from the nostril. The region of high velocity magnitude is much larger in the computational data, creating a V shape like profile towards the lower part. A gradual decrease in velocity magnitude can be observed in both flow fields from the tip towards the lower section of the nostril.
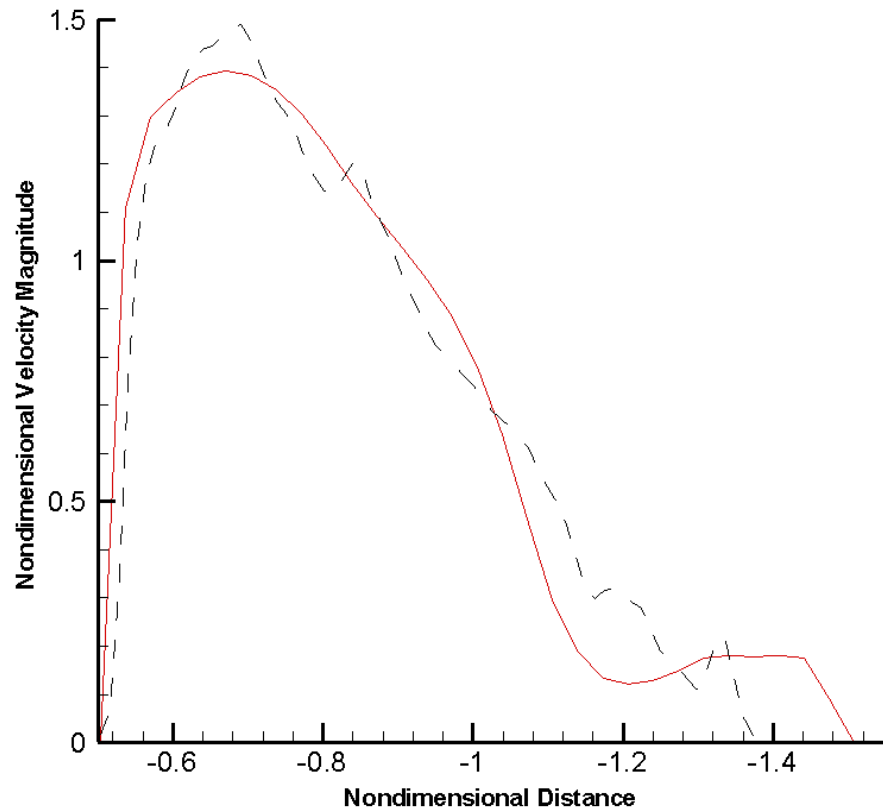
Figure 96: Non dimensional velocity magnitude profile across the nostril (at Z=0.6 and Z=1.524 for the computational and the experimental flow fields respectively) for the expiratory flow rate of 250 *ml/s*, showing the same region for the peak non-dimensional velocities.

The non dimensional velocity profiles across the nostril are plotted in Figure 96. Here the computational velocities across the nostril are taken from a plane parallel and slightly further way from the actual nostril to allow a fair comparison to the experimental data. The peak velocities occur at about 0.3 from the tip of the nostril for both flow fields followed by a decrease as the distance increases from the tip. This reduction in the computational data is much more uniform as compared to the experimental profile where some Sharpe changes can be observed. Calculating the velocities from the same cross sectional planes reveals higher experimental data similar to previous sections.

Both Figure 95 and Figure 96 show smaller experimental field. This is believed to be the result of variations in the experimental and the computational models. After manufacturing, the experimental model was embedded within a solid box with a very low transparency. The box was cut at the anterior and posterior regions to reach the level where the nostril and the nasopharynx were estimated to be. Furthermore the nostril and the nasopharynx opening were manually cut using an image of the computational data to form the same geometry for both opening. This resulted into a smaller opening for the nostril than in the actual computational model.

7.3   Effect of artificial viscosity on the flow field

Figure 97 shows the inspiratory internal flow fields at a plane located towards the posterior section of the nasal cavity. This is taken at the inspiratory flow rate of 200 *ml/s* and a Reynolds number of 10 times greater than the value used in the CFD

218

calculations. The calculated flow fields are based on two different schemes of first order upwind (Left) and a TVD scheme with a Superbee flux limiter (right), in order to study the effect of artificial viscosity. Applying the first order upwind scheme results into a stable solution due to the high value of artificial viscosity. On the other hand discretization based on a TVD scheme using a Superbee flux limiter is the least dissipative scheme.
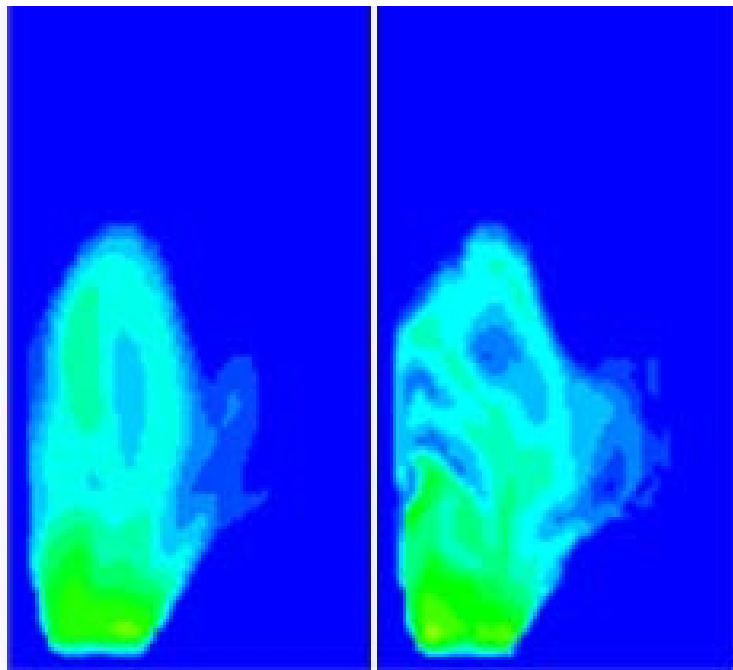
Figure 97: The internal nasal airflow field at a slide located at -3.5 on the X-axis (towards the nasopharynx) using a first order upwind scheme: (Left) and Superbee flux limiter (Right) at the inspiratory flow rate of 200 *ml/s* at a Reynolds number 10 times greater than in the normal nasal airflow. The influence of the numerical dissipation on solution can be observed as for the least dissipative solution the flow field is more developed.

Looking at the two images, it is clear that the flow field is dependent on the amount of artificial viscosity introduced into the solution. As expected changes in the least dissipative flow field are more gradual resulting into a flow field which is slightly

more developed. This difference between the two flow fields confirm the explanation given previously in this chapter for the differences between the PIV and the CFD results.

As a result of increasing the Reynolds number, a significant increase in turbulent kinetic energy k is also observed from the inflow value. This increase however is dampened by a large amount as the TVD scheme is replaced by the first order upwind scheme. This suggests that a high value of artificial viscosity can also influence the other important flow properties besides k. In this section since the Reynolds number was increased by ten times, it is expected to have similar flow fields as for the normal nasal cavity at the inspiratory rate of 20 *ml/s*. Although the flow patterns are quite similar to those obtained from the normal nasal cavity at a low inspiratory phase, but the large increase in k suggests that the flow field has no physical meaning as it was shown previously that there is only an increase in k from the inflow value for the inspiratory flow rate of 200 *ml/s* and higher. This non physical translation of the nasal airflow field as a result of increasing the Reynolds number supports the kinematic similarity used between the experimental and the computational data.

7.4 Summary

The Schlieren images of the external flow field showed that the nasal airflow leaves the cavity at an angle of about 60 degrees to the face. It then travels for a short distance until its velocity and temperature reaches to that of the surrounding air. The flow fields shown for one and two cavities also suggested that the airflows from

neighbouring cavities had an influence on each other due to the mixing. Same flow patterns were observed for repeated experiments using one subject, suggesting the consistency in an individual flow pattern over time. A reasonable qualitative agreement was obtained between the Schlieren images and the external computational flow field.

There was also a fair agreement between the computational and the PIV results as the flow fields were found to have similar characteristics. The non dimensional velocity profiles showed similar location for the peak velocities and the same trend. The computational fields were less developed due to the artificial viscosity introduced in the CFD data. This suggests the requirement for less artificial viscosity for the computational code.

Despite the similarities between the two flow profiles, the experimental velocities were shown to be higher than the computational data by 15%-20%. This can be explained due to the followings;

1. For the experimental model, the nostril and the nasopharynx openings had to be cut manually. This resulted into a smaller cross sectional area for the experimental nostril than in the computational model.

2. For the experiment model, at the nasopharynx, only a small circular hole was cut to allow inserting the air pipe to avoid air leaks. This nasopharynx opening was also smaller than the actual nasopharynx opening in the computational model. This also contributed to increased velocities observed in the experimental data.

3. For the scaling factor used in this study, the representative experimental flow rates for the computational inflow fluxes of 250, 150 50 *ml/s*, are 635, 381 and 127 *ml/s*

respectively. In order to achieve these flows in the experimental set up, the flow meter was adjusted to the higher end of the nearest value marked on the flow meter.

4. Finally some differences may have arisen due to a typical geometrical variation occurring during the production process [116] as well as the errors associated with both CFD and the PIV calculations.

In overall the fair to good agreement observed between the Schlieren and PIV images to the external computational data suggests the realistic prediction of the computational data. This includes both external and the internal CFD flow calculations for the normal nasal cavity and obstructed cavities. Furthermore it can be suggested that a simple optical technique such as Schlieren can be safely used in clinics for external nasal airflow visualisation to assess nasal obstructive disorders.

8.   Chapter 8

Discussion

This chapter covers a summary of work followed by a discussion of the results from chapters 5, 6 and 7.

8.1   Summary of Work

The nasal cavity is a communicating chamber between the environmental air and the respiratory system [117]. It acts as an efficient air conditioning device [66] which adjusts the temperature and humidity of the environmental air to nearly alveolar conditions in order to protect the sensitive lining of the lungs. The nasal cavity also contains the olfactory epithelium for the sense of smell and removes impurities with its ciliated mucosa. The significance of these physiological functions are proven since a healthy human would breathe through the nose by nature, even though its complex geometry imposes a much higher resistance in comparison to mouth breathing.

Nasal blockage is a common disease among many individuals. Usually the permanent type of nasal obstructive disorder occurs due to deformity in the structural body of the nasal cavity. The nasal blockage spoils the nasal functioning either by encouraging mouth breathing or by reducing the efficiency of transport process that control the humidity and temperature of the air [117]. It is therefore vital to understand and treat the nasal blockage. Unfortunately investigation and diagnosis of nasal blockage is quite challenging due to the small size and complex shape of the

nasal cavity. Current clinical tools for objective and structural assessment of the nasal obstruction, only provide a limited specific information and their contribution to the management of nasal airflow disorders has been disappointing [40]. In the last century investigation on nasal airflow dynamics has significantly enhanced our understanding of the nasal cavity functioning. It is also believed that such information may also be used in assessment of the nasal obstruction and its diagnosis. In addition to studying the nasal airflow behavior for the normal nasal cavity, there also have been many studies which have investigated the influence of the airways anatomical features on local airflow pattern and the physiological function [19, 54, 59, 102, 115, 118-120]. However all these studies are limited to the internal nasal cavity airflow dynamics which is quite difficult to be visualized if the nasal flow pattern is going to be used for diagnostic purposes. In this study the flow field inside and outside the nasal cavity was investigated for both normal nasal geometry and cavities with structural abnormalities. This is the first attempt where the external nasal flow field is investigated for both normal and abnormal nasal cavities.

The nasal airflow was investigated by means of experimental and computational tools using similar nasal geometries constructed from the CT scan of a healthy human nasal cavity. Each method had different strengths and weaknesses that lead to them being strongly complementary [116]. For the experimental investigation of the airflow pattern the two dimensional PIV technique was used since it provided quantitative results which can be used to complement the computational predictions [34]. In addition to the PIV, the Schlieren optical technique was also used for the

nasal airflow visualization of a human subject outside the nostrils. Although this technique is not quantitative, it is still a powerful, rapid and flexible tool for nasal flow field investigation and is suitable for clinical assessments since it can be used on human subjects.

For the computational calculations, a steady mean flow assumption was used to simulate the entire respiration. This assumption is not suitable for modeling the accumulative process such as heat and odorant transfer [116] which are not considered in this study, nevertheless it has been shown in other references that flow patterns are similar for the flow rates at quiet breathing to those calculated from the unsteady assumption [61, 62, 69, 108, 121]. For prediction of the possibility of turbulence flow, the low Reynolds number $k - \omega$ model was applied. This model was shown to be one of the most accurate compared to other turbulence models, due to the better treatment of adverse pressure gradient and viscous near wall region [30, 122, 123]. The computational nasal cavity was extended to cover an area outside the nostril, in order to allow calculations for the flow field outside the nostril as well as inside. The geometry of the nasal cavity was also varied to enable investigation of the nasal airflow through cavities with some of the most common conditions of nasal blockage.

8.2 Discussion of Results

Computations of the internal nasal airflow dynamics for the normal nasal cavity at different volume flow rates, suggested that the flow velocities are generally higher at both ends of the nasal cavity due to the reduction in the cross sectional area with the

main flow features being independent of the inflow rate. In the inspiratory phase the flow was found to be higher towards the septum and in the lower half of the nasal cavity. A small amount of air was observed through the upper airway and despite the small amount an increase in the flow was observed in the olfactory region which is believed to aid with the olfaction. This increase in flow proportion in the olfactory region has also been reported in the experimental study of the internal nasal airflow by Hornung et al. [33]. The lowest velocity magnitudes were observed at the turbinated area as compared to the other regions with a further reduction in the flow towards the meatuses. These observations confirm some of the previous numerical and experimental studies [7, 46, 54-56, 62] and are in contradiction with the results by Brucker et al. [47] where the main flow was found to pass through the middle and the upper airways. This contradiction is believed to be the result of low resolution of the nasal cavity anatomic data used for model generation of the nasal fossa in which studied by Brucker's study. The velocity profile within the nasal cavity suggests that, it is mainly the turbinated region that is responsible for the air flow conditioning as the flow spends longer in this region. In the expiratory phase the flow velocities were higher in the main nasal airway, and more uniformly distributed as a result of increasing cross flow component which allowed for more air through the meatuses. This is expected since the air conditioning is only significant in the inspiratory phase.

Two vortices were observed at the nasal valve and the nasopharynx regions due to the expansion in the cross sectional areas and the steep directional change in the flow direction supporting results from previous experimental and computational works [45, 55, 59, 61]. However the vortices reported by Schreck et al. [45] were observed

226

at different locations from those found in this study. This difference may be due to the geometrical variation between the two nasal cavity models as well as using an invasive flow measurement technique which would have interfered with the flow field itself. The anterior vortex disappeared as the inflow flux was reduced since the nasal airflow had more time to handle the adverse pressure gradient better. Studying the velocity fields including both vortices and only the posterior vortex suggested that, both anterior and to a lesser extend the posterior vortex give a spiraling motion to the flow streamlines in the turbinated area especially in the lower half. Having the spiraling velocity component ensures that the flow stays longer in this region which enhances the conditioning. The upper half unlike the lower region is only exposed to low velocity airflow with weak spiraling motion so that the sensitive olfactory epithelium is protected. This suggests that the conditioning mainly takes place in the lower half of the main turbinated region. It can also be concluded that the meatuses do not play an important role in the airflow conditioning due to their small surface area as well as allowing only a small amount of flow through them in the inspiratory phase. This is expected since the primarily function of the meatuses is to provide drainage for the secretion from the sinuses. The maintenance of the posterior vortex after a reduction in airflow velocity in the entire nasal cavity suggests that the posterior vortex may have an additional function. This additional role can be described as a directional functioning since the posterior vortex extracts the energy from the flow in the main nasal airway and directs it towards the pharynx where the lining is much more sensitive.

Similar to inspiration, two vortices were also observed in the expiratory mode, this time in the nasal vestibule region close to the nostril, and at the nasopharynx much closer to the floor of the nasal cavity. The location of both vortices suggested that the expiratory vortices are generated due the high directional change in flow direction as well as the nozzle effect for the anterior vortex. The phase of respiration as well as the less reduction in the size of the expiratory vortices compared to the inspiratory ones, at lower volume flow rates suggests that the expiratory vortices have a different function than maintaining the airflow for a longer period in the turbinated region. Since an increase in the flow through the meatuses was observed in the expiratory phase, it is believed that the posterior vortex is responsible in directing the flow to achieve a more uniform flow field where the flow is less opposed by the nasal resistance. This can be accepted since the inspiration is found to be harder than the expiration. The anterior vortex however, extracts energy from the airflow and directs it to leave the nostril.

Measurements of the flow field showed an increase in turbulent kinetic energy k from the inflow value for the flow rate of 200 *ml/s* and higher in the inspiratory phase. The highest turbulent kinetic energy was found at the nasal valve region close to the floor of the nasal cavity. The turbulent intensity I was also found to have its peak value at this region. This is caused as the flow experiences adverse pressure gradient due to the high directional change. There was also an increase in turbulent kinetic energy and turbulent intensity in the expiratory phase at the nasopharynx, starting at a higher flow rate of 250 *ml/s*. These increases also occur as the flow

undergoes a steep directional change. However these increases were much smaller as compared to those obtained from the inspiratory phase.

The values of nasal resistance (NR), for both steady laminar and steady RANS flow conditions, showed higher NR in inspiration. The nasal resistance was also higher for the RANS model, specifically for flow rates of 200 *ml/s* and higher although this difference was quite small. Higher nasal resistance in the inspiratory phase as well as the increases observed in both values of k and I suggests that the airflow undergoing the directional change, experiences adverse pressure gradient at the nasal valve region which may onset transition to the turbulent flow at inspiratory flow rate of 200 *ml/s* and higher [124]. With an increase in flow rate, an increase in turbulence and energy loss is also observed. This turbulent flow continues up to main nasal airway and then becomes laminar towards the posterior end, as the turbulent kinetic energy was only extended up to this region. Having a turbulent flow in the inspiratory phase, enhances the conditioning by increasing the heat and moisture exchange between the air and the nasal mucosa [125]. Although turbulent flow at higher volume flow rates have been reported in other works [33, 44, 46, 48, 49], but there are many other studies which have found the nasal airflow to be of a laminar nature [46, 51, 54, 55, 60]. Since both groups of these studies have been validated by other references, then it can be concluded that this uncertainty in the nature of the nasal airflow, perhaps arises due to having different types of airflow depending on the architecture of the nasal cavities. This is supported by two studies of Wolpoff [126] and Churchill et al. [49] who suggested that people exposed to cold and dry environments exhibit leptorrhine nasal features which induce turbulent flow

while people in hot and humid environments exhibit platyrrhine features that encourage laminar flow.

The anterior vortex was shown to influence the external nasal airflow for expiration by inducing across flow component towards the septum side and causing a reverse flow as the flow leaves the nostrils. The highest velocity magnitudes were found near the tip of the nostril. The external computational flow field was similar to the images taken from the flow field by the Schlieren system. This confirms the feasibility of an optical system such as Schlieren which allows producing quick data about the nasal airflow without the difficulties involved with internal flow measurements.

The influence of the anatomical variation on the nasal airflow dynamics was investigated by blocking the airflow at various locations within the nasal cavity. The results revealed a high level of dependency of the nasal airflow field on the internal geometry's structure since the smallest variation was shown to have a significant effect on both the internal and the external nasal airflow dynamics. In general the addition of blockage was accompanied by an increase in the local velocity magnitude and the overall nasal resistance. The amount of increase in the nasal resistance was found to be related degree of blockage. Variation in turbulent kinetic energy and intensity however were found to be related on the behavior of the velocity field in the anterior region (the nasal valve). Although the number of cases studied in this work was limited, but following general conclusions can be drawn. The anterior blockages are mainly followed by an increase in breathing effort as well as disturbing the olfaction whereas the posterior blockages within the lower half of the nasal cavity are more likely to reduce the efficiency of the nasal air conditioning. The nasal airflow

was shown to travel mainly through the lower half of nasal cavity in the turbinated region. This preferred path was shifted to the upper region after blocking the lower airway. This suggests that the nasal air conditioning mainly occurs in the lower region with a small contribution of the upper half which only becomes significant when blockage occurs in the lower region. This also confirms the need for a turbulent flow in the extreme environments to enhance the conditioning by both increasing the rate of heat and moist transfer as well as guiding more flows through the upper regions.

For all the nasal geometries considered in this study, a unique external nasal airflow was observed in the expiratory phase. For all anterior blockages, an increase in velocity magnitude and the flow angle (the angle between the airflow leaving the nostril and the face) was observed. The posterior blockages all resulted into thickening the flow stream leaving the nostril as well as increasing the velocity magnitude by a smaller amount as compared to the anterior blockages. This suggests that as the blockage moves further towards the nasopharynx, a reduction in flow angle and the velocity magnitude at the exit can be observed followed by an increase in its thickness. The relationship between the flow angle, velocity magnitude and its thickness to the position and perhaps the degree of nasal blockage can be a promising method to assess the nasal obstructive disorders, since it only requires an observation and measurements of the external flow field. For this more studies needs to be carried out in order to find a correlation between these flow properties using statistical analysis.

231

The CFD calculations for the internal flow field have been validated since the results agreed to those by other experimental and computational (using different codes) studies already pointed out through this study. However since no literature was found on the influence of the nasal cavity's geometry on the external nasal airflow field, some experiments were carried out using the PIV technique to measure the flow field outside the nostril for computational validation. Due to the modeling limitation, the cost and the time, only an enlarged non transparent silicon model of the computational nasal cavity free of any obstruction was made. A fair quantitative agreement was found between the computational and the experimental results. The main flow characteristics, such as the location of peak velocities, flow angle and the external flow thickness were found to be quite close. Despite these similarities, the experimental velocities were higher by 15%-20% than the computation data, for all the experiments carried out in this study. This was explained to be mainly the result of geometrical variations between the two models. Overall the experimental results confirmed the behavior found in the computational calculations for the external airflow of the normal nasal cavity, and hence increased the confidence in other CFD calculations which were carried out after addition of blockage.

In addition to the PIV measurements, some images from the external nasal airflow were taken using the Schlieren optical technique. These images showed similar flow angle and flow-stream's thickness to those by the CFD data despite being taken from a different nasal cavity. This may suggest that for a normal nasal cavity (free of any obstruction) the flow angle and the thickness of the main flow stream leaving the nostril can be expected to be similar among healthy adults. This similarity plus a

correlation between the flow angle and the thickness to the position and the degree of nasal blockage, supports the assessment of the nasal blockage based on the external airflow observation using techniques such as Schlieren where the images can be processed in a short time, as well as being of low cost, non invasive and reproducible. Other external techniques which have been used for analysis of nasal breathing such as thermal imaging [127] can also be used for assessment of blockage if a correlation between the nasal blockage and what they measure is found.

Although some validation of the results from this study were confirmed by other studies and the experimental data, other conflicting results can be just as valid due to variation in the anatomical geometry of each human nasal cavity which is used as the computational or the experimental model. The author believes that the nature of the internal nasal airflow strongly depends on the nasal cavity's geometry and depending on the nature of the nasal airflow unique flow characteristics can be exhibited. It is also believed that the external nasal airflow is less influenced by the internal structure of the nasal cavity and hence more similarity between the flow characteristics can be found (such as the flow angle and the thickness) as long as there is no obstruction. However this needs further investigation as only two different nasal cavities were investigated in this work.

9. Chapter 9

Conclusion & Future Work

Following the previous chapter which discussed the result of the study the conclusion and the recommended future work are written as follows in a concise manner for easy reading.

9.1 Conclusion

- The lower region of the nasal airway is the most significant region for airflow conditioning. The upper region is also responsible for conditioning to a lesser extends but it is mainly responsible for the olfaction. The anterior and posterior regions distribute and direct the nasal airflow and it is the shape of the anterior region which mainly influences the nature of the flow field.

- The nasal airflow can be either laminar or turbulent depending on the shape of the nasal cavity's geometry and the shape of the external nose. The nasal cavity has evolved into different shapes genetically, influenced by the environment, to condition the nasal airflow probably in the most efficient way possible. For this particular nasal cavity model used in this study, the inspiratory flow is found to have turbulent characteristics only in the anterior region, for flow rates of 200 *ml/s* and

higher. This turbulent flow enhances the airflow conditioning as it promote spiraling flow component and reduces the mean flow velocity in the main nasal airway.

- Variations in the nasal cavity's geometry have a significant influence on the internal nasal airflow and to a lesser extent on the external nasal airflow. The results from this study suggest that there may be a correlation between the external flow angle and its thickness with the location of the nasal blockage. Information about the degree of nasal blockage can also be achieved by velocity measurements of the external nasal airflow. Therefore the nasal blockage can be assessed using the external flow field only which avoids the current challenges involved with the clinical tools.

- Anterior blockages are mainly followed by an increase in breathing effort and a loss in the sense of smell. Posterior blockages in the lower half reduce the efficiency of the airflow conditioning.

- The influence of the internal blockages on the external flow field supports the assessment of nasal obstruction by flow visualization methods used for the external flow field which can be easily achieved using an optical technique such as Schlieren.

9.2   Future Work

The following recommendations are based on this study and the available literature:

- In order to develop methods for assessment of nasal obstruction based on airflow dynamics more studies need to be carried out. These studies should solely focus on the influence of the obstructive cavities on the nasal airflow field both internally and externally so that a correlation between the external nasal airflow field and the blockage can be established. Parallel to this, more studies need to be carried out on possible techniques for external flow measurements with the possibility of clinical usage.

- Nasal airflow was computed under the steady state assumption, since several studies have suggested that the airflow field is similar regardless of the steady and unsteady nature of the airflow. However the unsteady RANS or Large Eddy Simulation (LES) should be of interest since it can simulate the realistic cycle of breathing and account for the phase change period. In this project some computations were carried out using the unsteady assumption. However due to time limits and difficulties in data acquisition, only preliminary results were accumulated. The author recommends pursuing this line of investigation as more computational power become available.

- More investigation on different shapes of the nasal cavities and the airflow field is recommended. This will further establish the influence of the nasal geometry on the nature of the airflow.

- Further experimental investigation is also recommended in order to study the influence of the nasal blockages on both the internal and the external airflow fields. This will strengthened the possibly of using an optical measurement system to assess internal nasal blockage.

References

1. Eccles, R., *Nasal airflow in health and desease.* Acta Otolaryngol 2000. **120**(5): p. 580-595.

2. Rappai, M., et al., *The nose and sleep disorded breathing: What we know and what we do not know.* Chest, 2003. **124**(6): p. 2309-2323.

3. Nigro, C.E., et al., *Nasal Valve: anatomy and physiology* Braz J Otorhinolaryngol 2009. **75**(2): p. 305_310.

4. Tortora, G.J. and S.R. Grabowski, *Principles of anatomy and physiology.* 10 ed. 2003: John Wiley and Sons. Inc.

5. Lang, J., *Clinical anatomy of the nose, nasal cavity, and paranasal sinuses.* 1 ed. 1989: Newyork thieme medical published Inc.

6. Heetderks, D.R., *Observations on the reaction of normal nasal mucous membrane* Am.J.med.Sci, 1927. **174**(2): p. 231-243.

7. kelly, J.T., A.K. Prasad, and A.S. Wexler, *Detailed flow patterns in the nasal cavity.* J Appl Physiol, 2000. **89**(1): p. 323-337.

8. Naftali, S., et al., *Transport phenomena in the human nasal caivity: A comoutational model.* ANnal of biomedical engineering 1998. **26**(5): p. 831_839.

9. Burrow, A., R. Eccles, and A.S. Jones, *The effects of camphor, eucalyptus and mrthol vapour on nasal resistance to airflow and nasal sensation.* Acta Otolaryngol, 1983. **96**(1-2): p. 157-161.

10.	Jones, A.S., D.J. Willatt, and L.M. Durham, *Nasal airflow: resistance and sensation* Journal of Laryngology and Otology 1989. **103**(10): p. 909-911.

11.	Eccles, R. and A.S. Jones, *The effect of menthol on nasal resistance to airflow* Journal of Laryngology and Otology, 1983. **97**(8): p. 705-709.

12.	Jones, A.S., et al., *The effect of local anaesthesia of the nasal vestibule on nasal sensation of airflow and nasal resistance* Clinical Otolaryngology, 1987. **12**(6): p. 461-464.

13.	Jones, A.S., et al., *The effect of lignocaine on nasal resistance and nasal sensation of airflow.* Acta Otolaryngol, 1986. **101**(3-4): p. 328-330.

14.	Jones, A.S., et al., *Nasal sensation of airflow following blocakge of the nasal trigminal afferents.* Clinical Otolaryngology 1989. **14**(4): p. 285-289.

15.	Ramos, J.G., *The integration of respiratory movement. III The fifth nerve afferents.* Acta physiol. Lat. Am, 1960. **10**: p. 104-113.

16.	Corey, J.P., *Acoustic rhinometry: should we be using it?* . Curr Opin Otolaryngol Head Neck Surg 2006. **14**(1): p. 29-34.

17.	Corey, J.P., et al., *Evaluation of the nasal cavity by acoustic rhinometry in normal and allergic subjects.* Otolaryngology- head and neck surgery 1997. **117**(1): p. 22-28.

18.	Nummien, J., et al., *Reliability of acoustic rhinometry.* Respiratory Medicine, 2003. **97**(4): p. 421-427.

19.	Chandra, R.K., M.O. Patadia, and J. Raviv, *Diagnosis of nasal airway obstruction.* Otolaryngol Clin of North America 2009. **42**(2): p. 207-225.

20.   Clarke, R.W., A.S. Jones, and H. Richardson, *Peak nasal inspiratory flow-the plateau effect* the Jounral of Laryngology and Otology 1995. **109**(5): p. 399-402.

21.   Nathan, R.A., et al., *Objective monitoring of nasal patency and nasal physiology in rhinitis* J Allergy Clin Immunol 2005. **115**(3): p. 442-459.

22.   Julia, J.C., M. Enriqueta burches, and A. Martorell, *Active anterior rhinomamnometry in paediatrics. Normality criteria.* Allergol Immunopathol (madr), 2011. **39**(6): p. 342-346.

23.   Yaniv, E., et al., *Objective and subjective nasal airflow.* American journal of otolaryngology, 1997. **18**(1): p. 29-32.

24.   Lund, V.J., H. Holmstrom, and G.K. Scadding, *Functional endoscopic sinus surgery in managment of chronic rhinosinusitis. An objective assessment* J Laryngol Otol 1991. **105**(10): p. 832-835.

25.   Kim, C.S., et al., *Correlation between nasal obstruction symptoms and objective parameters of acoustic rhinometry and rhinomanometry.* Auris Nasus Larynx, 1998. **25**(1): p. 45-48.

26.   Scadding, G.K., Y.C. Darby, and C.E. Austin, *Acoustic rhinometry compared with anterior rhinomanometry in the assessment of the response to the nasal allegen challenges.* Clinical Otolaryngology, 1994. **19**(5): p. 451-454.

27.   Fairley, J.W., L.H. Durham, and S.R. Ell, *Correlation of subjective sensation of nasal patency with nasal inspiratory peak flow rate.* Clinical Otolaryngology, 1993. **18**(1): p. 19-22.

28. Enberge, R.N. and D.R. Ownby, *Peak nasal inspiratory flow and write peak flow: a comparison of their reproducibility.* Ann Allergy, 1991. **67**(3): p. 371-374.

29. Van der Leeden, R., E.J. Avital, and G. Kenyon, *Nasal airflow in a realistic anatomic geometry*, in *Direct and Large Eddy Simulation VI*, M.O. Friedrich R., Geurts BJ, Editor. 2005, Kluwer Academic Publishers. p. 423-430.

30. Wilcox, D.C., *Turbulence Modeling for CFD* 3rd ed. 2006: DCW Industries.

31. Mlynski, G., et al., *A method for studying nasal air flow by means of fluid dynamics experiments* Z. Med. Phys, 2000. **10**: p. 207-214.

32. Mlynski, G., et al., *Correlation of nasal morphology and respiratory function.* Rhinology, 2001. **39**(4): p. 197-201.

33. Hornung, D.E., et al., *Airflow Patterns in a Human Nasal Model.* Arch Otolaryngol Head Nech Surg 1987. **113**(2): p. 169-172.

34. Chung, S.K. and S.K. Kim, *Digital Particle Image velocimetry studies of nasal airflow* respiratory Physiology & Neurobiology, 2008. **163**(1-3): p. 111-120.

35. Hopkins, L.M., et al., *Particel image velocity measurements in complex geometries.* Exp Fluids, 2000 **29**(1): p. 91-95.

36. Saga, T., et al., *A comparative study of the PIV and LDV measurements on a self-induced sloshing flow* Journa of visulisation 2000. **3**(2): p. 145-156.

37. Brucker, C. and K.I. Park, *Experimental study of velocity fields in a model of human nasal cavity by DPIV*, in *Procedings 1st international symposium on*

turbulence and shear phenomena S. Banerjee and K. Eaton, Editors. 1999, Begell house Santa Barbara, California p. 831-836.

38.   Weinhold, I. and G. Mlynski, *Numerical simulation of airflow in the human nose.* Eur Arch Otorhinolaryngol, 2004. **261**(8): p. 452-455.

39.   Horschler, I., M. Meinke, and W. Schroder, *Numerical simulation of the flow field in a model of the nasal cavity.* Computer & fluids 2003. **32**(1): p. 39-45.

40.   Bailie, N., et al., *An overview of numerical modelling of nasal airlfow.* Rhinology, 2006. **44**(1): p. 53-57.

41.   Swift, D.L. and D.F. Proctor, *Access of air to the respiratory tract* In: Respiratory defense mechanisms, ed. J.D.B. L. M. Reid, D. F. Proctor 1977, New York: Dekker. 63-91.

42.   Girardin, M., E. Bilgen, and P. Arbour, *Experimental study of velocity fields in a human nasal fossa by laser anemometry.* Ann Otol RhinolLaryngol 1983. **92**(3 pt 1): p. 231-236.

43.   Stuirver, M., *Biophysics of sense of smell*, in *Groningen* 1958, Rijks University: The Netherland.

44.   Masing, H., *Investigations about the course of flow in the nose model.* Arch Klin Exp Ohr Nas kehkopf, 1967. **189**: p. 371-381.

45.   Schreck, S., et al., *Correlation between flow resistance geometry in a model of the human nose.* J Appl Physiol, 1993. **75**(4): p. 1767-1775.

46.   Hahn, I., P.W. Scherer, and M.M. Mozell, *Velocity profiles measured for airflow through a large-scale model of the human nasal cavity.* J Appl Physiol 1993. **75**(5): p. 2273-2287.

47.   Brucker, C., K.I. Park, and W. Limberg, *Experimental study of velcity fields in a model of human nasal cavity by DPIV* in *LaserAnemometry Advances and applications: Processings of the 7th international conference*, A.L. B. Ruck, D. Dopheide, Editor. 1997: University of Karlsruhe. p. 616-626.

48.   Simmen, D., et al., *A dynamic and direct visualization model for the study of nasal airflow.* Arch Otolaryngol Head Nech Surg, 1999. **125**(9): p. 1015-1021.

49.   Churchill, S.E., et al., *Morphological variation and airflow dynamics in the human nose* American journal of human biology 2004. **16**(6): p. 625-638.

50.   Proctor, D.F., *The upper airway*, in *The nose: Upper airway physiology and the atmospheric enviroment*, D.F. Proctor and I.B. IAnderson, Editors. 1982, Elsevier: New York. p. 23-43.

51.   Kim, J.K., et al., *Particle image velocimetry measurements for the study of nasal airlfow* Acta Oto- Laryngologica, 2006. **126**(3): p. 282-287.

52.   Elad, D., et al., *Analysis in airflow paterrns in human nose.* Medical & biological Engineering & computing 1993. **31**(6): p. 585-592.

53.   Proetz, A.W., *Air currents in the upper respiratory tract and their clinical importance.* Ann Otol Rhinol Laryngol 1951. **60**(2): p. 439-467.

54.   Keyhani, K., P.W. Scherer, and M.M. Mozell, *Numerical simulation of airflow in the human nasal cavity* Journal of Biomechanical engineering, 1995. **117**(4): p. 429-441.

55.   Subramaniam, R.P., et al., *Computational fluid dynamics simulations of inspiratory airflow in the human nose and nasopharynx.* Inhalation Toxicology 1998. **10**(2): p. 473-502.

56.   Sarangapani, R. and A.S. Wexler, *Modelling particle deposition in extrathoracic airway* Aerosol sicence and technology 2000. **32**(1): p. 72-89.

57.   Yu, G., Z. Zhang, and R. Lessmann, *Fluid flow and Particle diffusion in the human Upper Respiratory system.* Aerosol sicence and technology, 1998. **28**(2): p. 146-158.

58.   Croce, C., et al., *In vitro experiments and numerical simulations of airflow in realistic nasal airway geometry.* Annals of Biomedical Engineering 2006. **34**(6): p. 997-1007.

59.   Zhao, K., et al., *Effect of anatomy on human nasal air flow and odorant transport patterns: Implications for olfaction.* Cehm. Senses, 2004. **29**(5): p. 365-379.

60.   Grant, O., et al., *Validation of a numerical method for assessment of human nasal airflow* in *35th AIAA fluid dynamics conference and exhibit* T.C.D. Thornhill, Editor. 2005, American institute of Aeronautics and Astronautics Toronto, Ontario Canada.

61.   Ishikawa, S., et al., *Visualization of flow resistacne in physiological nasal respiration: analysis of velocities using numerical simulation.* Arch Otolaryngol Head Nech Surg, 2006. **132**(11): p. 1203-1209.

62.   Shi, H., C. Kleinstreuer, and Z. Zhang, *Laminar airflow and nanoparticle or vapor deposition in a human nasal caivty model.* Journal of biomechanical Enginerring 2006. **128**(5): p. 697-706.

63.   Horschler, I., et al., *Investigation of the impact of the geometry on the nose flow* European Journal of Mechanics B/Fluids, 2006. **25**(4): p. 471-490.

64.   Finck, M., D. Hanel, and I. Wlokas, *Simulation of nasal flow by lattice Boltzman methods.* Computers in Biology and Medicine 2007. **37**(6): p. 739-749.

65.   Leeden, R.V.D., E. Avital, and G. Kenyon, *A computational simulation of airflow in the human nasal caivty using a dynamic transnasal pressure.* 2007, Elsevier.

66.   Doorly, D., et al., *Experimental investigation of nasal airflow.* Proc Inst Mech Eng H. Journal of engineering in medicine 2007. **222**(4): p. 439-453.

67.   Leung, A.Y.T., et al., *Nasal ariflow simulation in models derived from cone ebam and spiral CT scans by using CFD.* Int. J. of Appl. Math and Mech, 2007. **3**(3): p. 49-61.

68.   Wen, J., et al., *Numerical simulation for detailed airflow dynamics in a human nasal cavity* Respiratory Physiology & Neurobiology, 2008. **161**(2): p. 125-135.

69.   Ishikawa, S., et al., *Flow mechanisms in the human olfactory groove.* Arch Otolaryngol Head Nech Surg, 2009. **135**(2): p. 156-162.

70. Wang, S.M., et al., *Comparison of micron -and nanoparticle deposition patterns in a realistic human nasal cavity* Respiratory Physiology & Neurobiology, 2009. **166**(2): p. 142-151.

71. Tan, J., et al., *Numerical simulation of normal nasal cavity airflow in Chinese adult: a computational flow dynamics model.* European Archives of Oto-Rhino-Laryngology: p. 1-9.

72. Cheng, X.B., et al., *Assessment of nasal bone fracture effect on nasal airflow: a computational fluid dyamics study.* Am J Rhinol Allergy, 2011. **25**(1): p. 39-43.

73. Cheng, X.B., et al., *Aerodynamics effect of inferior turbinate on nasal airflow: a computational fluid dynamics model.* Rhinology, 2010. **48**(4): p. 394-400.

74. Suponitsky, V., E.J. Avital, and M. Gaster, *on three domensionality and active control of incompressible caivty flow.* Physics of fluids, 2005. **17**(10): p. 104103.

75. Wilcox, D.C., *Simulation of transition with a two-equation turbilence model.* AIAA Journal 1994. **32**(2): p. 247-255.

76. Ruiz, P.C., et al., *Computational fluid dynamics simulations of the airflow in the human nasal cavity.* Acta Otorrinlaring Esp, 2005. **56**(9): p. 403-410.

77. Ferziger, J.H. and M. Peric, *Computational method for fluid dynamics.* 3rd ed. 2002: Springer.

78. Bridger, G.P. and D.F. Proctor, *Maximum nasal inspiratory flow and nasal resistance* Ann Otol Rhinol Laryngol 1970. **79**(3): p. 481-488.

79.   Versteeg, H.K. and W. Malalasekera, *An introduction to computational fluid dynamics, the finite volume method*. 2nd ed. 2007: Pearson prentice hall.

80.   Harlow, F.H. and R.F. Welch, *Numerical calculation of Time-Dependant viscouse incompressibel flow of fluid with free surface* The physics of fluid 1965. **8**(12): p. 2182-2189.

81.   Zalesak, S.T., *Fully multidimensional flux corrected transport algorithms for fluids* Journal of computational physics, 1979. **31**(3): p. 335-362.

82.   Boris, J.P. and D.L. Book, *Flux corrected Transport* Journal of computational physics, 1971. **135**: p. 172-186.

83.   Hirsch, C., *Numerical computational of internal and external flows*. Vol. 2: Computational methods for invisid and viscous flows 1988: John wiley & sons.

84.   Hirsch, C., *Numerical computational of internal and external flows*. Vol. 1. 1988: John wiley & sons.

85.   Peyret, R. and T.D. Tayloer, *Computational Methods for Fluid Flow* ed. R. Glowinski, et al. 1983: Springer-Verlag New York Inc.

86.   Kim, J. and P. Moin, *Application of a fractional-Step method to incompressible Navier-Stokes eqautions* Journal of computational physics 1985. **59**(2): p. 308-323.

87.   Pozrikidis, C., *On the relationship between the pressure and the projection function in the numerical computation of viscous incompressible flow* European Journal of Mechanics B/Fluids, 2003. **22**(2): p. 105-121.

88. Tau, E.Y., *A second order projection method for the incompressible Navier-Stokes equations in Arbitrary domains* Journal of computational physics, 1994. **115**(1): p. 147-152.

89. Goda, K., *A multistep Techinique with implicit differecing schemes for calculating two or three dimensional cavity flows* Journal of computational physics, 1979. **30**(1): p. 76-95.

90. Raffel, M., C.E. Willert, and J. Kompenhans, *Particle Image velocimetry: A Practical Guid* 1st ed, ed. R.J. Adrian, et al. 1998: Springer

91. Raffel, M., et al., *Particle Image Velocimetry , a practical guide*. 2nd ed. 2007: Springer

92. Taylor, H.G. and J.M. Waldram, *Improvment in the Schliere method* Journal of scientific instruments 1933. **10**(12): p. 378-389.

93. Settles, G.S., *Schlieren and shadowgraph techniques, visualizing phenomena in transparent media*. Experimental Fluid Mechanics ed. R.J. Adrian, et al. 2001: Springer.

94. Zhao, K., et al., *Numerical modeling of turbulent and laminar airflow and odorant transport during sniffing in the human and rat nose.* Chem Senses, 2006. **31**(2): p. 107-118.

95. Pallanch, J.F., T.V. McCaffrey, and E.B. Kern, *Normal nasal resistance* Archives of Otolaryngology Head & Neck Surgery, 1985. **93**(6): p. 778-785.

96. Kelly, J.T., et al., *Particle deposition in human nasal airway replicas manufactured by different methods. Part I: Inertial regime particles* Aerosol sicence and technology, 2004. **38**(11): p. 1063-1071.

97.   Naftali, S., et al., *The air conditioning capacity of the human nose.* Annals of biomedical engineering 2005. **33**(4).

98.   Garcia, G.J., et al., *Septal deviation and nasal resistance: an investigation using virtual surgery and computational fluid dynamics* Am J Rhinol Allergy 2010. **24**(1): p. 46-53.

99.   Grutzenmacher, S., et al., *First findings concerning airflow in noses with septal deviation and compensatory turbinate hypertrophy- a model study* ORL J otorhinolaryngol relat Spec, 2006. **68**(4): p. 199-205.

100.   Zambetti, G., et al., *Study and application of a mathematical model for the provisional assessment of areas and nasal resistance, obtained using acoustic rhinometry and active anterior rhinomanometry.* Clin Otalaryngol 2001 **26**: p. 286-293.

101.   Chen, X.B., et al., *Assessment of septal deviation effects on nasal airlfow: a computaitonal fluid dynamics model.* Laryngoscope, 2009. **119**(9): p. 1730-1736.

102.   Cole, P., et al., *The obstructive Nasal septum* Arch Otolaryngol Head Nech Surg, 1988. **114**(4): p. 410-412.

103.   Leong, S.C., et al., *A review of implications of computational fluid dynacmis on nasal airflow and physiology* Rhinology, 2010. **48**(2): p. 139-145.

104.   Berger, G., S. Gass, and D. Ophir, *The Histopathology of the Hypertrophic Inferior Turbinate.* Arch Otolaryngol Head Nech Surg, 2006. **132** (6): p. 588-594.

105.   Leong, S.C. and R. Ecceles, *Inferior turbinate surgery and nasal airflow: evidence-based management.* Current Opinion in Otolaryngology & Head & Neck Surgery, 2010. **18**(1): p. 54-59.

106.   Hanif, J., S.S. Jawad, and R. Eccles, *The nasal cycle in health and disease.* Clin Otolaryngol Allied Sci, 2000. **25**(6): p. 461-467.

107.   Farmer, S.E. and R. Eccles, *Chronic inferior turbinate enlargement and the implications for surgical intervention.* Rhinology, 2006. **44**(4): p. 234-238.

108.   Lindemann, J., et al., *Numerical simulation of intranasal airflow and temperature after resection of the turbinates.* Rhinology, 2005b. **43**(1): p. 24-28.

109.   Chen, X.B., et al., *Impact of interior turbinate hypertrophy on the aerodynamics pattern and physiological function of the turbulent flow- a CFD simulation model.* Rhinology, 2010. **48**(2): p. 163-168.

110.   Guo, Y., et al., *A computational fluid dynamics study of inner flow through nasal cavity with unilateral hypertrophic inferior turbinate.* Lin Chung Er Bi Yan Hou Tou Jing Wai Ke Za Zhi, 2009. **23**(17): p. 773-777.

111.   Wolf, J.S. and J.F. Biedlingmaier, *The middle turbinate in endoscopic sinus surgery.* Current Opinion in Otolaryngology & Head and Neck Surgery, 2001. **9**(1): p. 23-26.

112.   Kim, S.K. and S.K. Chung, *An investigation on airflow in disordered nasal cavity and its corrected models by tomographic PIV.* Meas Sci Technol 2004a. **15**(6): p. 1090-1096.

113. Tos, M., *Nasal polyps* Current Opinion in Otolaryngology & Head & Neck Surgery, 1995. **3**(1): p. 31-35.

114. LUdman, H. and P.J. Bradley, *ABC of Ear, Nose and Throat* 5th ed. 2007: Blackwell publishing Ltd.

115. Grutzenmacher, S., et al., *Investigations of the influence of external nose deformities on nassal airflow* ORL 2005. **67**(3): p. 154-159.

116. Doorly, D.J., D.J. Tayler, and R.C. Schroter, *Mechanics of airflow in the human nasala riways* Respiratory Physiology & Neurobiology, 2008. **163**(1-3): p. 100-110.

117. Elad, D., M. Wolf, and T. Keck, *Air conditionin in the human nasal caivty* Respir Physiol Neurobiol, 2008. **163**(1-3): p. 121-127.

118. Leopold, D.A., *The relationship between nasal anatomy and human olfaction* Laryngoscope, 1988. **98**(11): p. 1232-1238.

119. Damm, M., et al., *Intranasal volume and olfactory function.* Chem Senses, 2002. **27**(9): p. 831-839.

120. Landis, B.N., R. Giger, and A. Ricchetti, *Retronasal olfactory function in nasal polyposis* Laryngoscope, 2003. **113**(11): p. 1993-1997.

121. Hörschler, I., W. Schröder, and M. Meinke, *On the assumption of steadiness of nasal cavity flow.* Journal of Biomechanics, 2010. **43**(6): p. 1081-1085.

122. Mylavarapu, G., et al., *Validation of computational fluid dynmamics methodology used for human upper airway flow simulations.* Journal of biomechanics 2009. **42**(10): p. 1553-1559.

123.   Mihaescu, M., et al., *Large eddy simulation and Reynolds_Average Navier_Stokes modeling of flow in a realistic pharyngeal airway model: An investigation of obstructive sleep apnea.* Journal of biomechanics 2008. **41**(10): p. 2279-2288.

124.   Nayebossadri, S., E.J. Avital, and F. Motallebi. *Flow calculation for human nasal airway and blocakge effect on outflow pattern.* in *3rd European Fluid Dynamics Conference.* 2009. Nottingham: University of Nottingham.

125.   Lindemann, J., et al., *Nasal Mucosal temperature during respiration.* Clinical Otolaryngology, 2002. **27**(3): p. 135-139.

126.   Wolpoff, M.H., *Climatic influence on the skeletal nasal aperture* Am J Rhinol Allergy, 1968. **29**(3): p. 405-423.

127.   Fie, J. and I. Pavlidis, *Analysis of Breathing Air Flow Patterns in Thermal Imaging* in *28th Annual International Conference of the IEEE.* 2006, Engineering in Medicine and Biology Society: New York. p. 946-952.